THE UNIVERSITY OF
WARWICK

AUTHOR: **James Robinson** DEGREE: **Ph.D.**

TITLE: **The Geodesic Acoustic Mode in strongly-shaped tight aspect ratio tokamaks**

DATE OF DEPOSIT: .....

I agree that this thesis shall be available in accordance with the regulations governing the University of Warwick theses.

I agree that the summary of this thesis may be submitted for publication.

I **agree** that the thesis may be photocopied (single copies for study purposes only).

Theses with no restriction on photocopying will also be made available to the British Library for microfilming. The British Library may supply copies to individuals or libraries. subject to a statement from them that the copy is supplied for non-publishing purposes. All copies supplied by the British Library will carry the following statement:

> "Attention is drawn to the fact that the copyright of this thesis rests with its author. This copy of the thesis has been supplied on the condition that anyone who consults it is understood to recognise that its copyright rests with its author and that no quotation from the thesis and no information derived from it may be published without the author's written consent."

AUTHOR'S SIGNATURE: .....

USER'S DECLARATION

1. I undertake not to quote or make use of any information from this thesis without making acknowledgement to the author.
2. I further undertake to allow no-one else to use this thesis while it is in my care.

DATE SIGNATURE ADDRESS

.....

.....

.....

.....

.....

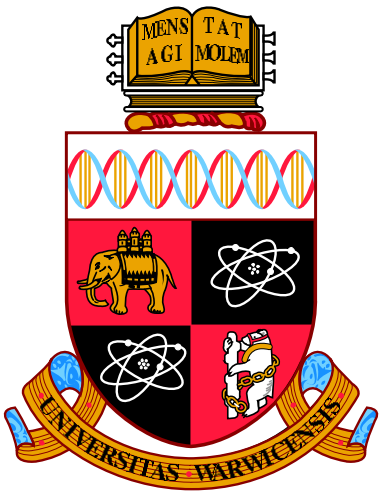

The Geodesic Acoustic Mode in strongly-shaped tight aspect ratio tokamaks

by

James Robinson

Thesis

Submitted to the University of Warwick

for the degree of

Doctor of Philosophy

Department of Physics and Astronomy

January 2013

THE UNIVERSITY OF WARWICK

Contents

List of Tables

List of Figures

Acknowledgments

I would like to thank my supervisor, Bogdan Hnat for all his help and support, together with collaborators from Culham Centre for Fusion Energy in particular Andrew Kirk and Ken McClements for their useful comments. At Warwick, all my fellow PhD students, including Chris Wrench, David Higgins and Stephen Gallagher for useful discussions of ideas and for the help with debugging the code.

Declarations

The content of this thesis is entirely the work of the author, with the following exceptions. The data obtained from the MAST discharges used in chapter 3 was originally gathered in 2009 and published in [Tamain et al., 2010].

The first identification of the geodesic acoustic mode in MAST, including the relationship to RMPs and rotation was published by the author as:
J R Robinson, B Hnat, P Dura, A Kirk, P Tamain, and the MAST Team, *Plasma Phys. and Controlled Fusion* **54** 105007 (2012)[Robinson et al., 2012]

The simulation code `CENTORI` was developed at CCFE as given in [Knight et al., 2012], the documentation of which was used extensively in chapter 4 to detail the system of equations used. The results of the simulations presented in chapters 4 and 5 have been submitted for publication in Physics of Plasmas, following approval by CCFE.

In addition the author collaborated on a paper titled 'Vorticity scaling and intermittency in drift-interchange plasma turbulence' [Dura, Hnat, Robinson, and Dendy, 2012], but this work is not featured here.

The author acknowledges EPSRC support (grant EP/G02748X/1). This work was part-funded by the RCUK Energy Programme under grant EP/I501045 and the European Communities under the contract of Association between EURATOM and CCFE. The views and opinions expressed herein do not necessarily reflect those of the European Commission.

Abstract

This thesis presents comparison between experimental measurements from the spherical tokamak MAST, two-fluid simulation data and theory of the Geodesic Acoustic Mode (GAM) in tight aspect ratio strongly shaped tokamak plasmas. The first identification of a strong $\approx$ 10kHz mode detected in both potential and density fluctuations of the edge plasma in MAST using a reciprocating probe is given. The mode is radially localised, with outer limit $\approx$ 2cm inside the separatrix, and is affected on application of resonant magnetic perturbations (RMP) generated by external coils. A shift in frequency with plasma rotation is found, and a suppression of the mode is observed above a certain threshold. Non-linear coupling to high wave number turbulence is evident, and an increase in power of turbulence fluctuations is seen after suppression. These observations are then interpreted in the context of known low frequency plasma modes present in the toroidal configuration. The supposition that the observed mode is a geodesic acoustic mode is considered and motivated by experimental observations and numerical simulations.

Chapter 1

Introduction

"The greatest shortcoming of the human race is our inability to understand the exponential function"

— Albert Bartlett

"Turbulence is the most important unsolved problem of classical physics."

— Richard Feynman

1.1 Motivation

The motivation for the work described in this thesis can be presented on many levels. First, it is of direct consequence to the development of nuclear fusion as a viable energy source and thus should be considered in the wider context of current transition from fossil fuel energy sources to those that are sustainable in the long term. Secondly, it relates to one of the most challenging topics of modern classical physics, dynamics of non-equilibrium systems. Emergence of large scale structures is a hallmark signature of such systems, and here we examine an acoustic mode which could arise from turbulence fluctuations - a classic example of so called "zonal flow" emergence. In this context, plasma dynamics, is merely an example of much larger class of physical systems, where concepts such as instabilities, bifurcations and turbulence can be considered. And thus, this work has been motivated by both, a practical aspects of controlling turbulence in the tokamak as well as purely scientific curiosity.

The exponential growth in human population since the start of the industrial revolution has primarily been as a result of the increased availability of energy, in the form of fossil fuels, to do work. Either directly via heat and transport, or indirectly

via provision of clean water and fertiliser for agriculture. There are many reasons for wanting to cut the use of fossil fuels, one being the release of CO_2 causing climate change. However, irrespective of the desire or not to reduce consumption, the finite supply of resources will soon dominate. The rise and fall of production of any finite resource was demonstrated by Hubbert [1956] as shown in figure 1.1, which shows world peak oil usage. Similar curves can be plotted for other resources such as coal. While this logistic distribution model is over–simplistic as there will be new discoveries and other factors to enlarge the total area under the curve and introduce a few bumps on the way down, we will need to transition to a range of other sources of energy to maintain the current population.

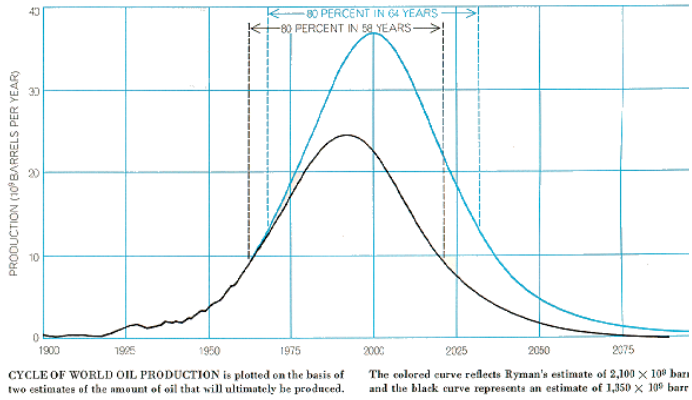

Figure 1.1: Hubbert Curve of 'peak oil', showing exponential growth then fall in production. [Hubbert, 1971, p39]

The cornucopian ideal that the increasing material demands of society will be met by corresponding advances in technology is at the heart of the desire to develop a new plentiful source of energy. So-called renewable energy such as solar and wind, together with nuclear fusion is seen in many eyes as that grail. However it could be that these simply delay the inevitable Malthusian prophecy that exponential population growth will eventually give way through to 'non-linear' mechanisms such as war and disease, as we fight over access to other resources [Malthus, 1798].

In the medium term, as we decline on the right hand side of the Hubbert curve, there will be a desire to restrict the use of hydrocarbons for energy supply so they can be used to manufacture materials (e.g. plastics). The low energy density of renewables and so requirement for large areas of land (or ocean), limit their use to only the most favourable areas, some distance from population centres. While the energy demand can be met in the next 50 years by the use of a new generation of fission reactors, to complement the contribution from renewables, in the longer term a new energy–dense source such as fusion is desired.

The development of magnetically confined fusion (MCF) plasma into a viable source of energy rests on our ability to control the stability of a plasma heated to in excess of 200 million kelvin. Such plasmas are complex systems, with dynamics driven by collective interactions of the individual particles with the fields through a plethora of modes. Even when global-scale instabilities are eliminated, micro-instabilities drive turbulent plasma transport, and this is a key obstacle in achieving self-sustained fusion reaction in a tokamak at the present time. Other factors being tritium production, build-up of impurities, and neutron damage to wall materials.

It would be mistaken, however, to think that such behaviour can be found only in fusion plasmas. In fact, there are many similarities between the study of economics, ecology and fusion research. The growth of instabilities in any bound system can often be modelled as a simple linear phase where the amplitude of the instability rises with a constant percentage in a given time, leading to exponential growth, powered by the availability of free energy in the system. This growth is maintained while the demand of energy is small compared to the supply of energy from the system as a whole. However, just as in the supply of natural resources, or any economic relationship, the growth of an instability in a plasma soon becomes dominated by feedback mechanisms which arise from the non-linear interactions between elements of the system. If the driving is sufficient, complex behaviour can emerge in several ways such as a bifurcation, where the system oscillates between states in a limit cycle, a series of growth followed by sudden avalanche type collapses forming a sawtooth pattern, or chaotic fluctuations such as turbulence. A simple demonstration of this is the logistic function, where P could represent some parameter like population, or wave mode amplitude, over time

$$\frac{dP}{dt} = rP(1-P). \tag{1.1}$$

Figure 1.2 shows the solution to the logistic function and the behaviour of the corresponding discrete mapping, $P(t+1) = rP(t)(1-P(t))$, when iterated forward in time from $P(0) = 0.5$ for different growth rates, r.

The study of non-linearly driven oscillations, and the flow of energy in turbulent plasmas therefore gives not only the hope of better controlling a fusion power plant, but also, at a more generic level, we may learn some lessons of how to better control other complex systems.

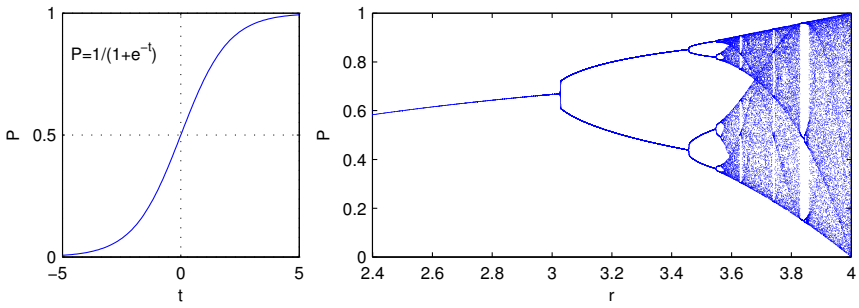

Figure 1.2: (a) Logistic function showing classical S-shaped exponential growth and saturation, (b) envelope of logistic map for varying growth rate r, showing bifurcation and chaotic regimes

1.2 Thesis Outline

This thesis will offer direct comparison between experiment, theory and simulation of a class of large scale oscillations known as the Geodesic Acoustic Mode (GAM), driven by turbulence at the edge of tokamaks, highlighting the key phenomena and characteristics of the mode, their role as a sink of turbulent energy, and so as a key moderator of energy and particle transport out of the plasma. Also discussed will be the role of another instability known as Edge Localised Modes (ELMs). Controlling these potentially damaging disruptions will be essential in ITER [Holtkamp, 2007] and any future fusion power plant. However the method so far used for controlling them by the application of small radial perturbations to the magnetic field, known as Resonant Magnetic Perturbations (RMPs), is shown to interact and suppress the GAM under certain conditions, subsequently increasing the background turbulence level.

The experimental observations were from the Mega Amp Spherical Tokamak (MAST). The simulations performed on the University of Warwick Centre for Scientific Computing's $\approx$ 5800 core high performance cluster '`minerva`'. These were matched to the MAST configuration but then extended up to larger aspect ratio tokamak conditions with various shaping parameters.

Firstly in this introduction we cover some basics of nuclear fusion and plasma physics, highlighting the challenges involved. In Chapter 2 we expand on the two-fluid description of a plasma, and its discretisation into a numerical model suitable for efficient parallel computation, including some basic results from a simple 3D two-fluid code developed in the early stages of this work. In Chapter 3 analysis of data from MAST is presented, including the observation of a 10kHz electrostatic oscillation, and its identification as a Geodesic Acoustic Mode. In Chapter 4 the

experimentally observed mode is compared to a simulation performed using the code `CENTORI` developed at CCFE. Chapter 5 then rounds off the discussion by comparing simulations over a wide parameter range to theoretic descriptions. Concluding in Chapter 6 with a summary of results and discussion of future work proposed to investigate GAMs further.

1.3 Background

Understanding the mechanisms by which turbulence interacts with large scale structures and modes is key to controlling magnetically confined plasmas. Turbulence mediates the flux of energy from small scale instabilities to large scale flows which in turn influence global confinement properties. A generic class of drift instabilities [Hazeltine and Meiss, 1985] provides a driving mechanism for the turbulence at the edge of a confinement device where density and temperature gradients are steep. Upon achieving certain amplitudes, turbulent fluctuations can self-organise into linearly stable zonal flows [Diamond et al., 2005; Hasegawa and Wakatani, 1983; Jakubowski et al., 2002; Lin et al., 1998] which act as a sink of energy for turbulence [Rosenbluth and Hinton, 1998].

In the context of magnetically confined plasma, zonal flows are defined as radially localised, with $a^{-1} < k_r < \rho_i^{-1}$ where ρ_i is the ion Larmor radius a is the tokamak minor radius, axisymmetric and azimuthally symmetric ($m = n = 0$, where m and n are the poloidal and toroidal mode numbers, respectively) electrostatic potential modes, with frequency $\Omega \approx 0$. Zonal flows can couple to other low frequency modes, for example, the Geodesic Acoustic Mode (GAM) [Winsor, 1968] which results from the compressibility of the zonal flows in toroidal geometry, coupling to a compressible (acoustic) mode with $m = \pm 1$, through the geodesic curvature of the confining magnetic field. This mode is distinct from the low frequency Ion Acoustic Modes (IAM), which in strong magnetic field are predominantly field aligned and thus may be strongly Landau damped.

The electromagnetic properties of low frequency oscillations at the edge of the plasma and their interaction with Alfvénic modes are not well understood. Any coupling to magnetic field perturbations opens an additional channel for turbulent energy dissipation and thus could provide an important mechanism for stabilisation of turbulence. A limited number of studies have explored this area suggesting that electromagnetic effects could be important for low frequency oscillations in tokamaks [Leconte and Diamond, 2012; Smolyakov et al., 2008] and stellarators [Fujisawa et al., 2008].

1.4 Nuclear Fusion

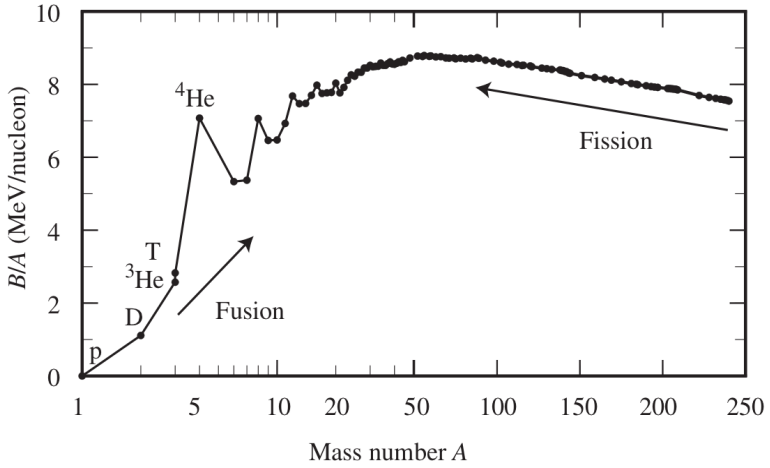

Figure 1.3: Binding energy per nucleon vs mass number, A [Azteni and Meyer-ter-Vehn, 2004]

.

The binding energy per nucleon curve (figure 1.3) shows that just as with fission of heavy nuclei, by fusing light nuclei a vast store of energy could be released. In order for two light nuclei to fuse they need to approach close enough for the nuclear forces to take over from the Coulomb repulsion of the positive protons within it. This means the ions must be travelling fast enough for their kinetic energy to overcome the potential barrier enough that the chance of quantum tunnelling through becomes significant. This equates to a centre–of–mass kinetic energy of at least 50keV.

There are many possible fusion reactions, such as the p+p chain and CNO cycle important in stars or those involving lithium. However here we restrict ourselves to just the major ones of interest for fusion power:

$$\begin{aligned}
\mathrm{D} + \mathrm{D} &\longrightarrow {}^{3}\mathrm{He} + \mathrm{n} + 3.27\mathrm{MeV} \\
\mathrm{D} + \mathrm{D} &\longrightarrow \mathrm{T} + \mathrm{p} + 4.03\mathrm{MeV} \\
\mathrm{D} + \mathrm{T} &\longrightarrow {}^{4}\mathrm{He} + \mathrm{n} + 17.6\mathrm{MeV} \\
\mathrm{T} + \mathrm{T} &\longrightarrow {}^{4}\mathrm{He} + 2\mathrm{n} + 11.3\mathrm{MeV} \\
\mathrm{D} + {}^{3}\mathrm{He} &\longrightarrow {}^{4}\mathrm{He} + \mathrm{p} + 18.3\mathrm{MeV} \\
\mathrm{p} + {}^{11}\mathrm{B} &\longrightarrow 3{}^{4}\mathrm{He} + 8.7\mathrm{MeV}
\end{aligned}$$

As can be seen from figure 1.4 the fusion reaction cross section for all the reactions

drops off rapidly at low energies. The long tail of a Maxwellian velocity distribution means even at relatively low temperatures some fusion will occur, but when averaged over the thermal distribution only the deuterium-tritium reaction gives viable reaction rates below the 20keV or so temperature achievable in a tokamak. Reactions such as $p + {}^{11}B$ are classed as "advanced aneutronic fuels" and have the distinct advantage that much lower neutron fluxes are produced, and hence will involve much lower total radioactive material inventories. However, as shown by [Rider, 1995], no fusion reactions other that D+T, D+D, and $D + {}^{3}He$, can reach ignition in an optically thin plasma, due to the relation between power radiated via bremsstrahlung and atomic number, $P_{\text{brem}} \propto Z^2$. Higher Z ions such as boron radiatively cool faster than fusion reactions can heat them, unless some other mechanism can reduce these losses, such as the quantization of electron Larmor orbits into Landau levels by the extremely high magnetic fields found in plasma focus devices [Lerner et al., 2011]. Furthermore, given the much higher scattering collision rate of ions, compared to the fusion reaction cross-section, essentially all fusion plasmas must be at or near a Maxwellian thermal equilibrium. The temperatures needed for fusion are much

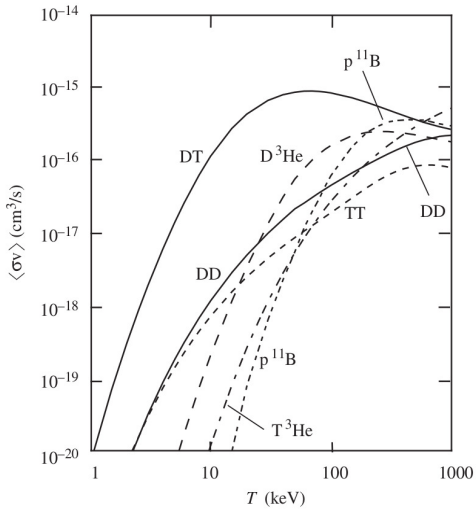

Figure 1.4: Maxwellian averaged reactivity versus temperature for reactions of interest [Azteni and Meyer-ter-Vehn, 2004].

higher than the ionisation energy of hydrogen ($13.6eV$), or indeed any element. As a gas is heated such that a significant fraction of the atoms undergo ionisation, so that by 50eV a hydrogen plasma can be considered as fully ionised. As such, the focus of fusion research is essentially that of plasma physics.

1.4.1 Lawson Criteria

During early development of fusion concepts during the 1950s the principle factors for achieving fusion were studied. A 'figure of merit' criteria was derived by [Lawson, 1957] relating the temperature, density and energy confinement time required to achieve net energy gain was established. Given that the D-T reaction rate, as shown in figure 1.4 in the region from $10 - 20$keV is roughly proportional to T^2 the rate of heating from the fusion alphas balances the losses when

$$n\tau_E T = 2.6 \times 10^{21} \text{keVm}^{-3}\text{s}^{-1} \tag{1.2}$$

The energy confinement time is defined as the total thermal energy of a volume of plasma divided by the rate of loss of power $\tau_E = W/P_{\text{loss}}$. This leads to two scenarios for fusion power generation: the high density short confinement time of inertial fusion, or the low density long confinement of magnetic fusion. While inertial confinement fusion is known to work in the form of the H-bomb, it is not yet practical as an energy source. Magnetic confinement is far closer, in the authors opinion, to a practicable device delivering net power output. However there are significant engineering and materials challenges that face both approaches before a commercially viable design is accomplished.

1.4.2 Tokamak

In the presence of strong, externally applied, magnetic field the motion of ions and electrons is restricted perpendicular to the field but not parallel to it. So, in order to confine a plasma using a magnetic field the field lines must wrap around to form a closed surface. A magnetohydrodynamic (MHD) equilibrium can then be established, balancing the collective forces between the ion and electron motions and the fields when considered on a macroscopic scale. This can be expressed by reducing the full fluid equations (see chapter 2) to the static case where $v = 0$ and $\partial/\partial t = 0$

$$\begin{aligned} \nabla p &= \mathbf{J} \times \mathbf{B} \\ \nabla \times \mathbf{B} &= \mu_0 \mathbf{J} \\ \nabla \cdot \mathbf{B} &= 0 \end{aligned} \tag{1.3}$$

The simplest shape to satisfy this condition is a torus. A sphere (or any topological equivalent) cannot, due to a special case of the Poincaré-Hopf theorem [Brouwer, 1912], whereby one can imagine trying to comb a vector field on the surface of a

ball such that the vector is tangent to the surface everywhere. This is not possible and leaves at least one pole with the vector pointing normal to the surface.

It was quickly realised that the toroidal curvature leads to a net drift on the ions upwards and the electrons down. The resulting imbalance causes a vertical electric field and, via the $\mathbf{E} \times \mathbf{B}$ drift, a loss of confinement. The solution is to add a twist to the magnetic field. This is introduced via running a toroidal current through the plasma to induce a poloidal component to the field, as shown in figure 1.5. The

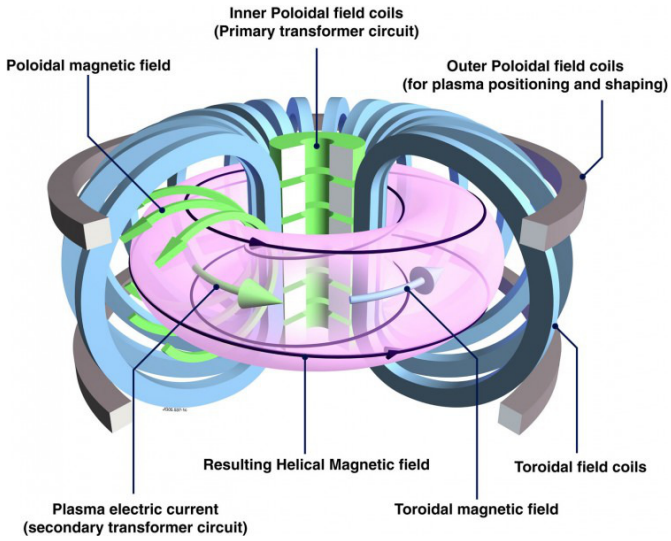

Figure 1.5: Schematic of a tokamak [EDFA-JET]

induced poloidal magnetic field is modified by a further series of outer poloidal coils which control the position and shape of the plasma boundary within the vacuum vessel.

An alternative method of introducing the necessary twist is the stellarator concept [Spitzer Jr., 1958], where a complex set of three dimensional external coils rotate the entire plasma column. This has the advantage of enabling continuous operation, compared to the tokamak which is reliant on the sweep of central solenoid as one side of a transformer circuit, inducing the current in the plasma as its secondary side. However, the complex coil shapes are hard to design and manufacture, and require strong rigid support structures to prevent the coils collapsing onto themselves.

From the equilibrium equations (1.3), substituting Ampère's law into the force balance gives the pressure balance

$$\nabla \left(p + \frac{B^2}{2\mu_0} \right) = \frac{1}{\mu_0} (\mathbf{B} \cdot \nabla) \mathbf{B} \tag{1.4}$$

The ratio of the pressure and magnetic pressure terms on the left hand side yields the plasma beta, $\beta = p/(B^2/2\mu_0)$, a key parameter governing the stability of the equilibrium against the bending and compression of the magnetic field on the right hand side of equation (1.4). The combination of contributions to the magnetic field by the toroidal and poloidal fields forms a series of nested surfaces with constant pressure which can be uniquely labelled by a poloidal flux function ψ, so $p = p(\psi)$. The equilibrium solution for ψ is found via the Grad-Shafranov equation, detailed in section 4.1.1.

1.4.3 Heating gap

The heating of a plasma via Ohmic or Joule heating can never achieve the required $10 - 20$keV temperatures for fusion, as illustrated by figure 1.6. The combination of ohmic and alpha heating falls below the total losses between $1 - 5$keV [Sweetman, 1973]. Early analysis grossly under estimated the ion heat transport, putting it lower than the contribution from bremsstrahlung. In reality the large turbulence driven contribution to ion heat losses make the picture far worse. So auxiliary heating via

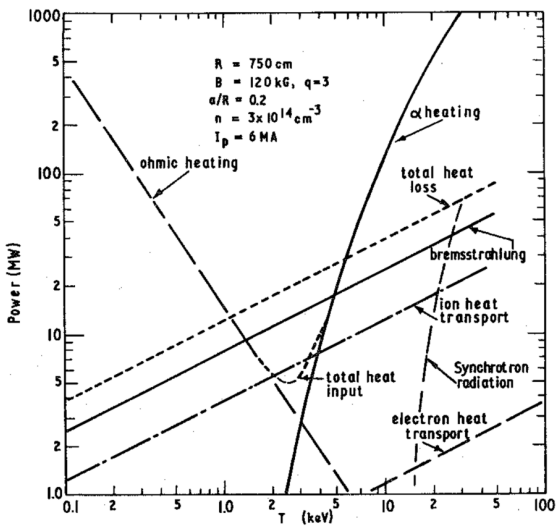

Figure 1.6: Heating gap from Sweetman [1973]

neutral beam or various radio frequency methods is envisaged to be able to bridge the gap. However, it is now appreciated that the brute force approach, of applying more and more heating is only part of the solution, since with increasing auxiliary power P_{aux}, the confinement parameter $n_e\tau_E$ decreases roughly as the inverse square root of P_{aux}/P_{ohm} due to increased level of drift wave turbulence, and so thermal diffusivity [Horton, 2012]. Thus any method for controlling or reducing the turbulent

transport can potentially reduce the level of external heating required. Or put alternatively; enabling steeper a temperature gradient to exist, without adversely affecting transport or introducing large disruptions, could enable break-even with smaller devices.

1.5 Introductory plasma physics

1.5.1 Plasma definition

It is useful to start from the basic definition of a plasma. Once a heated gas is sufficiently ionised the motion of the ions and free electrons form currents which enable long range interactions via the associated electric and magnetic fields. If the ion and electron density is such that the behaviour of the system is characterised by the collective effects of particles with the fields, the state of matter is referred to as a plasma. Specifically in a plasma at temperature T_e the ions and electrons will move to shield out the electric field from any point charge over a distance known as the Debye length, defined as

$$\lambda_D \equiv \left(\frac{\varepsilon_0 T_e}{n_e e^2}\right)^{1/2} \tag{1.5}$$

provided the number of particles within a Debye sphere, $(4/3)\pi\lambda_D^3 \gg 1$, so that the statistical definition of a temperature is valid. As is conventional in plasma physics, the Boltzmann constant k_B is incorporated throughout into the temperature, and is thus expressed in energy unless otherwise stated. The transport in a plasma is governed by the long range collective electric field fluctuations $\mathbf{E}_{\mathbf{k}\omega}$, for wavenumber $\mathbf{k}$, and angular frequency, ω for $k\lambda_D \ll 1$, and binary collisions for $k\lambda_D > 1$ [Horton, 1999]. The rate at which the electrons move to shield out any such charge, in an unmagnetised plasma, is characterised by the frequency at which a perturbation in the electron density will oscillate, known as the electron plasma frequency

$$\omega_{pe} = \left(\frac{n_e e^2}{\varepsilon_0 m_e}\right)^{1/2} \tag{1.6}$$

1.5.2 Motion of a charged particle in an electromagnetic field

A particle with charge q and mass m experiences the Lorentz Force such that the motion of the particle is

$$m\frac{d\mathbf{v}}{dt} = q(\mathbf{E} + \mathbf{v} \times \mathbf{B}) \tag{1.7}$$

In a uniform magnetic field the particle follows a helical path that can be decomposed into the constant parallel velocity and circular motion in the perpendicular plane with frequency $\omega_c = qB/m$, and radius $\rho = v_\perp/\omega_c = mv_\perp/(qB)$. The rapid circular gyration can be considered as a current loop with magnetic moment $\mu = mv_\perp^2/2B$. The motion of the guiding centre is then further decomposed into various drifts.

1.5.3 Particle drifts

If an electric field is present at some angle to the magnetic field, the charged particles are subject to a drift that is independent of the charge, mass and energy of the particle. By moving the frame of reference the electric field can be transformed away such that $\mathbf{E} + \mathbf{v}_f \times \mathbf{B} = 0$. Crossing this with $\mathbf{B}$ gives the drift velocity $\mathbf{v}_E = \mathbf{v}_f$

$$\mathbf{v_E} = \frac{\mathbf{E} \times \mathbf{B}}{B^2} \tag{1.8}$$

Similarly any net force F added to the right hand side of equation (1.7) will result in a perpendicular drift of the guiding centre of

$$\mathbf{v}_F = \frac{1}{q_s}\frac{\mathbf{F} \times \mathbf{B}}{B^2} \tag{1.9}$$

However unlike the $\mathbf{E} \times \mathbf{B}$ drift which is in the same direction for ions and electrons, other drifts depend on the charge and so direction of the gyro-orbit with respect to the B-field. Which can be summarised as follows for each species $s = i, e$

Polarisation drift

If some force $\mathbf{F}$ is imposing perpendicular to a uniform magnetic field the equation of motion becomes

$$m_s\frac{d\mathbf{v}}{dt} = \mathbf{F} + q_s\mathbf{v} \times \mathbf{B} \quad \Rightarrow \quad \mathbf{v}(t) = \mathbf{v}_g(t) + \mathbf{v}_\parallel(t) + \frac{\mathbf{F} \times \mathbf{B}}{q_s B^2} \tag{1.10}$$

where $\mathbf{v}_g(t)$ is the fast gyro–motion. The subsequent charge separation creates an increasing electric field over time $\mathbf{E}_\perp(t) \approx \mathbf{E}_\perp(0) + (\partial\mathbf{E}_\perp(0)/\partial t)t$. This next order correction to the perpendicular motion gives the polarisation drift

$$\mathbf{v}_{ps} = -\frac{m_s}{q_s B^2}\frac{d\mathbf{E}_\perp}{dt} \tag{1.11}$$

which can normally be neglected for electrons due to their low mass, but for ions is the source of electrostatic oscillations between density and potential ϕ, where

$$\mathbf{E} = -\nabla\phi - \frac{\partial \mathbf{A}}{\partial t} \tag{1.12}$$

and the time derivative of the magnetic vector potential $\mathbf{A}$ can be taken to be small.

Magnetic drifts

If the magnetic field is not uniform, the curvature along the field line and perpendicular to it introduce two further drifts

$$\mathbf{v}_R = \frac{\mathbf{v}_\parallel^2}{\omega_{c,s} R} \tag{1.13}$$

where R is the radius of curvature, and the $\nabla\mathbf{B}$ drift

$$\mathbf{v}_{\nabla\mathbf{B}} = \frac{\mathbf{v}_\perp \rho_s}{2} \frac{\mathbf{B} \times \nabla\mathbf{B}}{B^2} = \frac{\mu}{m_s \omega_{c,s}} \mathbf{b} \times \nabla\mathbf{B}. \tag{1.14}$$

where μ is the magnetic moment. The two magnetic drifts can be combined as:

$$\mathbf{v}_B = \frac{\mathbf{v}_\parallel^2 + \frac{1}{2}\mathbf{v}_\perp^2}{\omega_{c,s}} \frac{\mathbf{B} \times \nabla\mathbf{B}}{B^2} \tag{1.15}$$

1.5.4 Diamagnetism and magnetisation drift

The gyro motion of each charged particle is intrinsically diamagnetic. From a collective particle viewpoint the sum of all the magnetic moments $\mu = -(mv_\perp^2/2B)\mathbf{b}$ induces a magnetisation current $\mathbf{J}_\mu = \nabla \times \mathbf{M}$, where $\mathbf{M} = n\langle\mu\rangle = -(p_\perp B)\mathbf{b}$, given that $p_\perp = nT_\perp$. Here the angle brackets denote a weighted average over the velocity distribution. This results in a magnetisation drift of $\mathbf{v}_\mu = \mathbf{J}_\mu/qn$. Combining this with velocity averaged curvature drifts gives the total cross-field guiding centre drift due to particle gyration and non-uniformity of the magnetic field [Garcia, 2003]

$$\langle \mathbf{v}_B + \mathbf{v}_\mu \rangle = \frac{1}{q_s n B} \mathbf{b} \times \nabla p_\perp + \frac{p_\parallel - p_\perp}{q_s n B} \nabla \times \mathbf{b}. \tag{1.16}$$

The second term vanishes for isotropic pressure and uniform fields. This collective particle result is the same as taking the fluid approach where the drift is calculated from the divergence of the gyrotropic form of the pressure tensor $\overleftrightarrow{P} = p_\perp(\overleftrightarrow{I} - \mathbf{bb}) + p_\parallel \mathbf{bb}$. For isotropic pressure the opposing diamagnetic drifts for ions and

electrons are then simply

$$\mathbf{v}_d = -\frac{1}{q_s n}\frac{\nabla p_s \times \mathbf{B}}{B^2}. \tag{1.17}$$

This is often split up into the separate contributions due to density and temperature, or as in some reduced models, using a cold ion approximation, taken as just the component due to the density gradient. The illustration, figure 1.7, of diamagnetic drift, shows even though the individual orbits may be stationary (thus not being advected) there is a net effect on the average velocity within the fluid element. This appears in the full fluid equations as the gyroviscous cancellation (see Section 2.1.3).

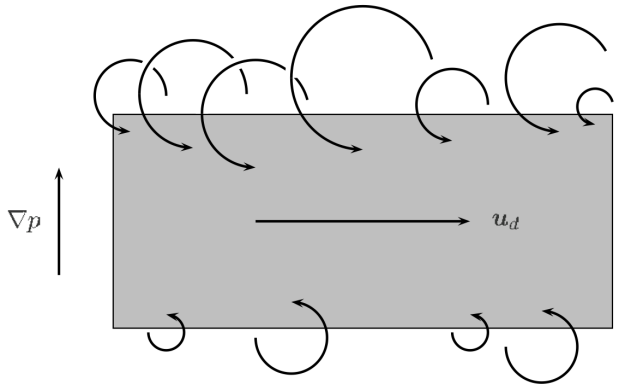

Figure 1.7: Origin of diamagnetic drift in a fluid element due to an imbalance of particle orbit average velocities between the high and low pressure side [Garcia, 2003]

.

1.5.5 Ordering

By comparison of the various characteristic velocities, wave modes, scale lengths and collision times it is possible to order the behaviours such that the complexity of model can be reduced by neglecting smaller terms. This ordering process can also enable new insights as to the possible relationship between interactions.

Restricting ourselves to the case of a strongly magnetised plasma, we can consider the magnitude of electrostatic effects by comparing the $\mathbf{E}\times\mathbf{B}$ drift velocity with the thermal velocity

$$\mathbf{v}_E = \frac{\mathbf{E}\times\mathbf{B}}{B^2} \quad \text{and} \quad \mathbf{v}_{th} = \sqrt{\frac{2k_B T}{m_i}} \tag{1.18}$$

then, if the scales are such that

$$\frac{\mathbf{v}_E}{\mathbf{v}_{th}} \sim 1 \tag{1.19}$$

then this is the regime of Magnetohydrodynamics, or MHD. Whereas, if

$$\frac{\mathbf{v}_E}{\mathbf{v}_{th}} \sim \frac{\rho_i}{L} = \delta < 1 \tag{1.20}$$

where the scaling parameters are ρ_i, the ion Larmor radius, and L is taken as either the scale of the device i.e. minor radius a, or a characteristic scale length such as $L_n = n/|\nabla n|$ then this is known as drift ordering. In the drift limit the equilibrium is such that ion polarisation drift, and heat fluxes must be taken into account. To improve the model further the the next order finite Larmor radius (FLR) effects such as the gyro-viscous and other $O(\delta^2)$ contributions can be included.

At higher frequencies, such that $\omega/\omega_{ci} \sim 1/\delta$, the $\mathbf{J} \times \mathbf{B}$ term dominates over the pressure and the regime is known as Hall-MHD.

	Electron	Ion	MHD	Drift	Transport
Timescale	$\sim ps$	$\sim ns$	$\sim \mu s$	$\sim 10\mu s$	$\sim ms$
Frequency	$\omega_{ce} = eB/m_e$	$\omega_{ci} = eB/m_i$	$\omega_A = kv_A$	$\omega^* = k_y T_e/eBL_n$	
Simulation Methods	Vlasov Particle in Cell	Hybrid-PIC	ideal MHD fluid	resistive MHD	
		$\longleftarrow$	Gyrokinetic	$\longrightarrow$	
		$\longleftarrow$	Two-fluid	$\longrightarrow$	

Table 1.1: Hierarchy of time scales and corresponding physics and numerics, adapted from [Tajima, 2004].

1.6 Kinetic description of a plasma

1.6.1 Fokker-Plank Equation

Starting from the exact Liouville equation describing in full the position and velocity of every ion and electron, some approximation needs to be made to reduce the task to a tractable problem. The first step is to express the 6 dimensional phase space (3 position & 3 velocity components) of all the electrons & ions, as a distribution function f as described by the Fokker-Plank equation.

$$\frac{\partial f}{\partial t} + \mathbf{v} \cdot \nabla f + \frac{e}{m} \left(\mathbf{E} + \mathbf{v} \times \mathbf{B} \right) . \frac{\partial f}{\partial \mathbf{v}} = \left(\frac{\partial f}{\partial t} \right)_c \tag{1.21}$$

Where the collision term on the right hand side is derived from the contribution of many small angle collisions. In some cases, such as the core of a tokamak, this can

be neglected, so the equation reduces to the Vlasov equation.

1.6.2 Gyro-Kinetics

If the plasma is strongly magnetised then term $(\mathbf{v} \times \mathbf{B}).\partial f/\partial \mathbf{v}$ is assumed to be the largest. This governs the gyro-motion of electron and ions around magnetic field lines. Expanding the Fokker-Plank equation with $\omega_c^{-1}\partial/\partial t \ll 1$ and $\rho/L \ll 1$ yields the *drift kinetic equation*

$$\frac{\partial f}{\partial t} + \mathbf{v_g} \cdot \nabla f + \left(e_j \mathbf{E} \cdot \mathbf{v_g} + \mu \frac{\partial B}{\partial t} \right) \frac{\partial f}{\partial K} = \left(\frac{\partial f}{\partial t} \right)_c , \tag{1.22}$$

where f is now a function of position, magnetic moment μ, and kinetic energy $K = \frac{1}{2} m_j v^2$. The guiding centre velocity, $\mathbf{v_g}$, is sum of the rapid parallel motion, $\mathbf{E} \times \mathbf{B}$ and curvature drifts. By averaging over the fast gyro-period the phase space is reduced from 6D down to 5D with 3 position and two velocity related components $(\mathbf{r}, \mu, K)$. Then by careful choice of coordinate system aligned to the background magnetic field the problem can be reduced to a computable scale. The plasma is assumed to be in approximate thermal equilibrium such that the distribution function can be expressed as a Maxwellian distribution, plus a perturbation $f = F_m + \tilde{f}$.

$$F_m(v) = \left(\frac{m}{2\pi k_B T} \right)^{3/2} e^{-mv^2/2k_b T} \tag{1.23}$$

Further simplifications are normally taken by expanding in terms of perturbations in $\mathbf{E}$, $A_\parallel$ and $B_\parallel$.

The drift-kinetic equation and the gyro-kinetic model derived from it rely on certain assumptions which begin to break down in the pedestal and near the edge of a tokamak. To simulate the edge region we need a model that can cope with density and temperature gradient scale lengths much closer to the ion Larmor radius. Also although simplified, gyro-kinetic simulations are still very computationally expensive and cannot easily access low frequency global modes such as the geodesic acoustic mode.

Chapter 2

Fluid Theory and Modelling

"essentially, all models are wrong, but some are useful"

— G. E. P. Box, *1987*

2.1 Velocity Moments

The fluid model is an attempt to reduce the complexity of the system described by the full 6D distribution function. A more useful model can be expressed in terms of the macroscopic properties, such as density, pressure, and bulk fluid velocities. The distribution function $f_s(\mathbf{x}, \mathbf{v}, t)$, is defined with normalisation such that taking the integral $\int f_s(\mathbf{x}, \mathbf{v}, t) d^3\mathbf{x} d^3\mathbf{v}$ is the volume. The moment is then

$$M(\mathbf{x}, t) = \int Q(\mathbf{v}) f_s(\mathbf{x}, \mathbf{v}, t) d^3\mathbf{v} \tag{2.1}$$

such that taking $Q(\mathbf{v}) = 1, m\mathbf{v}, mv^2, mv^2\mathbf{v}$ in turn yields continuity equations for the number density, momentum, energy and heat flux respectively for each volume element. With each equation dependent on the value of the next higher moment. If the particle velocity $\mathbf{v} = V + \delta\mathbf{v}$ where $\delta\mathbf{v}$ is the random thermal velocity, and $\mathbf{V} = \langle\mathbf{v}\rangle$ is the bulk average fluid velocity then stress tensor is defined as

$$\overleftrightarrow{\Pi} \equiv m\langle\delta\mathbf{v}\delta\mathbf{v}\rangle \tag{2.2}$$

In the frame moving with the fluid such that $\mathbf{V} = 0$ this reduces to the pressure tensor. The trace of this tensor is simply the scalar pressure, so for species, $j = i, e$, $p_j = n_j k_B T$, so $\overleftrightarrow{P_j} = p_j \overleftrightarrow{I} + \overleftrightarrow{\pi_j}$, with $\overleftrightarrow{\pi_j}$ just containing the off diagonal components. The series of moment equations is closed at some level by approximating

terms involving the next higher order moment with parameters already defined. The choice of closure is a central problem that needs to be addressed by any theory or model of turbulence, and is motivated by the relative sizes of the various terms, in particular the level of collisionality, and the time scale being investigated. Provided the ion and electron velocity distributions are not too far from Maxwellian, the system can be adequately described by just the first few moments. There exist standard closure schemes appropriate for the MHD limit; [Braginskii, 1957] and drift limit [Mikhailovskii and Tsypin, 1971]. Here we follow Braginskii, omitting for now the off-diagonal components of the stress tensor and heat fluxes. A fuller discussion of the anisotropic terms in these schemes together with various corrections can be found in [Catto and Simakov, 2005, 2004, 2006]. In the cooler edge region of a tokamak the collisionality is sufficiently high that the fluid approach can be justified as collisions will quickly tend to restore any divergence from a Maxwellian velocity distribution. However, despite the smaller Larmor radius, the short scale length of the temperature and density gradients make the parameter $\delta = \rho/L$ sufficiently large that some finite Larmor radius (FLR) effects should be accounted for. In particular rather than the simplification to a single fluid of MHD, the small scale fluctuations due to finite ion inertia, and slow collision rate between ions and electrons, requires keeping track of the ion and electron temperatures separately.

In addition to these coordinate independent requirements the toroidal topology, and magnetic field gradients introduce other anisotropic effects in a tokamak due to 'neoclassical' theory as detailed later in section 2.8.2.

2.1.1 Continuity equation

The conservation of mass is approached from the perspective of the number density of charge carriers for each species, assuming the plasma is fully ionised. From the definition of a plasma, it is taken as being 'quasi-neutral' on a timescale averaged over longer than ω_p^{-1}, and spatial scale longer than λ_D such that net charge density within a macroscopic fluid element, $\rho = e(Zn_e - n_i)$ is zero, thus Gauss' law becomes

$$\nabla \cdot \mathbf{E} = \frac{\rho}{\epsilon_0} \approx 0 \tag{2.3}$$

That is, although there can be electric fields, they only occur as dipole and higher order contributions not isolated build-up of charge at any particular location. Thus, for singly charged ions $n_e = n_i = n$, and we can reduce the system to just one continuity equation

$$\frac{\partial n}{\partial t} + \nabla \cdot (n\mathbf{v_i}) = S^n \tag{2.4}$$

where the particle density is advected at the ion fluid velocity $\mathbf{v_i}$, and S^n includes the contribution from any particle sources or sinks, often taken as zero.

2.1.2 Momentum equations

The change in momentum for each species can be written as the sum of forces on a fluid element

$$nm_i \frac{d\mathbf{v_i}}{dt} = -\nabla \cdot \overleftrightarrow{P_i} + en\left(\mathbf{E} + \mathbf{v}_i \times \mathbf{B}\right) + \mathbf{R_{ei}} + \mathbf{S_i^v} \tag{2.5}$$

$$nm_e \frac{d\mathbf{v_e}}{dt} = -\nabla \cdot \overleftrightarrow{P_e} - en\left(\mathbf{E} + \mathbf{v}_e \times \mathbf{B}\right) + \mathbf{R_{ie}} + \mathbf{S_e^v} \tag{2.6}$$

where $\mathbf{R_{ie}} = -\mathbf{R_{ei}}$ is the rate of momentum transfer from ions to electrons, $\mathbf{S_s^v}$ are any momentum sources (eg. neutral beam injection). The total or advective derivative is defined as

$$\frac{d}{dt} = \left(\frac{\partial}{\partial t} + \mathbf{v_s}.\nabla\right) \tag{2.7}$$

The electron velocity can be defined from the difference from the bulk ion velocity and the plasma current

$$\mathbf{v}_e \equiv \mathbf{v}_i - \frac{\mathbf{J}}{en} \tag{2.8}$$

where the current is found from Ampère's law, but neglecting the displacement current

$$\nabla \times \mathbf{B} = \mu_0 \mathbf{J} + \frac{1}{c^2}\frac{\partial \mathbf{E}}{\partial t} \qquad \Rightarrow \qquad \mathbf{J} = \frac{\nabla \times \mathbf{B}}{\mu_0} \tag{2.9}$$

The collisional momentum transfer term is comprised of a frictional and a thermal component $\mathbf{R_{ie}} = \mathbf{R_u} + \mathbf{R_T}$. In the MHD applicable Chapman-Enskog style closure system of Braginskii these can be expressed as [Braginskii, 1957, 1965]

$$\mathbf{R_u} = \frac{nm_e}{\tau_e}(0.51u_\parallel + u_\perp) = ne(\eta_\parallel J_\parallel + \eta_\perp J_\perp) \tag{2.10}$$

$$\mathbf{R_T} = -0.71n\nabla_\parallel T_e - \frac{3n}{2|\omega_{ce}|\tau_e}\mathbf{b} \times \nabla T_e \tag{2.11}$$

where $\mathbf{u} = \mathbf{v_e} - \mathbf{v_i}$ and $\mathbf{b} = \mathbf{B}/B$. Keeping here, the anisotropic behaviour of the resistive and temperature gradient terms. The electron-ion collision time τ_e is given by

$$\tau_e = \frac{12\pi^{3/2}\epsilon_0^2 m_e^{1/2} T_e^{3/2}}{\sqrt{2} n_i Z e^4 \ln\Lambda} \tag{2.12}$$

where for $T_e > 10\text{eV}$ the Coulomb logarithm [Wesson, 2004]

$$\ln \Lambda \approx 15.2 - 0.5 \ln(n_e/10^{20}) + \ln T_e, \qquad n_e \text{ in m}^{-3}, T_e \text{ in keV} \tag{2.13}$$

On the timescales $\gg \omega_p^{-1}$ the electrons can be taken to react instantaneously to any change, i.e. they have zero interia. As we will see later in section 2.4.2, this has important implications of the types of waves supported. So, setting the left hand side of the electron momentum equation (2.6) to zero, and subsituting in (2.8), and dividing through by en we get

$$0 \approx \frac{m_e}{e}\frac{d}{dt}\left(\mathbf{v}_i - \frac{\mathbf{J}}{en}\right) = -\frac{\nabla \cdot \overleftrightarrow{P_e}}{en} - \left(\mathbf{E} + \left(\mathbf{v}_i - \frac{\mathbf{J}}{en}\right) \times \mathbf{B}\right) + \frac{\mathbf{R}_{ie}}{en} \tag{2.14}$$

rearranging for $\mathbf{E}$, and simplifying the pressure and resistive terms to be isotropic this reduces to a form of Ohm's law

$$\mathbf{E} = -\mathbf{v_i} \times \mathbf{B} + \eta \mathbf{J} + \frac{\mathbf{J} \times \mathbf{B}}{en} - \frac{\nabla p_e}{en} - 0.71 n \nabla_\parallel T_e - \frac{3n}{2|\omega_{ce}|\tau_e} \mathbf{b} \times \nabla T_e \tag{2.15}$$

2.1.3 Diamagnetic gyroviscous cancellation

For the electrons the small Larmor radius makes the off-diagonal pressure tensor components due to the gyro-motion small on the fluid scale. However for the ions, in the drift limit, the temperature and density can change over the width of the ion Larmor radius. The traceless part of the stress tensor in the fluid rest frame (ie. the pressure tensor) can be split into parts dependent on collision frequencies, the remainder is defined as the gyroviscous stress

$$\overleftrightarrow{P} = \pi_{gv} + \pi_{\text{coll}} \tag{2.16}$$

The gyroviscous stress π_{gv} for slow drift dynamics is of order $\delta^2 p$ where $\delta = \rho_i/L$, and can be found from the solution to [Hazeltine and Waelbroeck, 2004]

$$\mathbf{b} \times \pi_{gv} + (\mathbf{b} \times \pi_{gv})^\dagger = \frac{m}{\omega_{ci}} \nabla \cdot \mathbf{M}_3 \tag{2.17}$$

where

$$\mathbf{M}_3 = \int f \mathbf{v}\mathbf{v}\mathbf{v} d^3 v \tag{2.18}$$

is the third order moment of f. This is sufficiently complicated that we want to avoid having to calculate it if possible. Luckily, we do not need π_{gv} directly as it only enters as its divergence. It can be shown that the gyroviscous force due to this

term does not directly contribute to the advection of the ions [Ramos, 2005]. The full expression contains many terms, but to lowest order is given by

$$\nabla \cdot \pi_{gv} \simeq -m_i n \mathbf{v_{i*}} \cdot \nabla \mathbf{v_i} - \nabla \chi \tag{2.19}$$

where the magnetization velocity is

$$\mathbf{v_{i*}} = \frac{1}{en} \nabla \times \left(\frac{p_i \mathbf{B}}{B^2} \right) \tag{2.20}$$

but this is often approximated as the diamagnetic velocity,

$$\mathbf{v_d} = \frac{1}{en} \mathbf{B} \times \nabla \left(\frac{p_i}{B^2} \right) \tag{2.21}$$

However this approximation is only valid if the magnetic field is constant, without significant curvature. χ in the above equation is a term which modifies the perpendicular pressure leaving the parallel pressure unmodified

$$\chi = \frac{m p_\perp}{2eB} b.\mathbf{w} \tag{2.22}$$

where $\mathbf{w} = \nabla \times \mathbf{v_i}$ such that

$$p_\perp \longrightarrow p_\perp - \chi = p_\perp \left(1 - \frac{m}{2eB} b.\mathbf{w} \right) \tag{2.23}$$

Ignoring all the smaller corrections the main result is known as the gyroviscous cancellation, modifying normal advective term $\mathbf{v_i} \cdot \nabla \mathbf{v_i}$ to

$$\mathbf{v_i} \cdot \nabla \mathbf{v_i} \longrightarrow (\mathbf{v_i} - \mathbf{v_{i*}}) \cdot \nabla \mathbf{v_i} \simeq \mathbf{v_E} \cdot \nabla \mathbf{v_i} \tag{2.24}$$

2.1.4 Energy equations

The next velocity moment in mv^2 yields the equations for energy. These can be expressed various ways in terms of the pressure, temperature, or total internal energy including the component due to the magnetic field. Here we use the form for ion and electron temperature from [Wesson, 2004, p92].

$$\frac{3}{2} n \frac{dT_s}{dt} = -p_s \nabla \cdot \mathbf{v_s} - \nabla \cdot \mathbf{q_s} + Q_s + S_s^T \tag{2.25}$$

Where the electron heat flux includes frictional and temperature gradient components $\mathbf{q_e} = \mathbf{q_{ue}} + \mathbf{q_{T_e}}$

$$\mathbf{q_{ue}} = nT_e \left(0.71\mathbf{u}_\parallel + \frac{3/2}{|\omega_{ce}|\tau_e}\mathbf{b} \times \mathbf{u} \right) \tag{2.26}$$

$$\mathbf{q_{T_e}} = \frac{nT_e\tau_e}{m_e} \left(-3.16\nabla_\parallel T_e - \frac{4.66}{\omega_{ce}^2\tau_e^2} - \frac{5/2}{|\omega_{ce}|\tau_e}\mathbf{b} \times \nabla T_e \right) \tag{2.27}$$

the ion heat flux just has the temperature graduent components

$$\mathbf{q_i} = \frac{nT_i\tau_i}{m_i} \left(-3.9\nabla_\parallel T_i - \frac{2}{\omega_{ci}^2\tau_i^2} - \frac{5/2}{|\omega_{ci}|\tau_i}\mathbf{b} \times \nabla T_i \right). \tag{2.28}$$

The ion and electron temperatures equilibrate due to collisions slowly, with a factor of m_e/m_i

$$Q_i = \frac{3m_e}{m_i}\frac{n}{\tau_e}(T_e - T_i) \tag{2.29}$$

the corresponding term for the electrons has the addition of the ohmic heating, ηJ^2

$$Q_e = -\mathbf{R_{ie}} \cdot \mathbf{u} - Q_i = \eta_\parallel J_\parallel^2 + \eta_\perp J_\perp^2 + \frac{1}{en}\mathbf{J} \cdot \mathbf{R_T} + \frac{3m_e}{m_i}\frac{n}{\tau_e}(T_i - T_e) \tag{2.30}$$

2.1.5 Faraday's Law

The system of equations is closed with the last two Maxwell equations not yet introduced: Faraday's law

$$\nabla \times \mathbf{E} = -\frac{\partial \mathbf{B}}{\partial t} \tag{2.31}$$

and the solenoidal condition for the magnetic field (i.e. there are no free magnetic monopoles)

$$\nabla \cdot \mathbf{B} = 0 \tag{2.32}$$

This last requirement is not explicitly set, but given the form of Faraday's law as long as the initial condition for the magnetic field is divergence free, then is held. Care must be taken when defining any numerical scheme to ensure this remains true. One approach is to evolve the magnetic vector potential $\mathbf{A}$ rather than the magnetic field directly, where $\mathbf{B} = \nabla \times \mathbf{A}$

$$\frac{\partial \mathbf{A}}{\partial t} = -\mathbf{E} - \nabla\phi \tag{2.33}$$

2.2 Numerical Modelling

The process of transforming a set of partial differential equations describing a physical model into a numerical algorithm suitable for simulating a given scenario is dependent on a number of factors. Computation is built up from a set of basic integer and floating point operations. These have a fixed level of precision and accuracy, and so can introduce numerical instabilities into a code that if not careful can dominate other factors. Typically scientific modelling is done using the standard IEEE754 double-precision format. In this numbers are stored as a 64bit binary number comprised of 1 sign bit, 11bit exponent and 52bit mantissa, giving a maximum precision of $log_{10}(2^{53}) \approx 16$ decimal digits (for single precision it is only 7 digits). Given that the relative size of terms in the equations can be separated by many orders of magnitude it is important to express calculation of variables in such a way as to maintain the precision as far as possible. For many quantities where we are dealing with small perturbations on a background value it can make sense to store the perturbed value in a separate variable[Higham, 2002].

For modelling a 3D system the number of operations per time-step quickly becomes unmanageable for any reasonable system size on a single workstation, therefore a parallel algorithm is needed to divide the model across many processors. This is achieved by using a technique know as domain decomposition, whereby each processor handles a small local cell of the domain and communicates the changes across its boundaries with neighbouring cells. Thus each processors grid has an extra layer of grid points around the edge which are copied from the neighbouring cell after each time-step. Another guiding principle is to reuse data where possible, in that all calculations requiring a variable (or array element) should be performed in close proximity to ensure the data is still in the local CPU cache, as fetching from main memory is very slow by comparison. To the extent that if the quantity needed can be (re)calculated from values known to be in the cache then this will be faster than loading a stored value from main memory.

In order to maintain stability of the numerical algorithm the speed at which variations in parameters propagate (ie the fastest wave speed in that direction) must be less than the the grid spacing times the time-step. This is known as the Courant-Friedrichs-Lewy (CFL) condition[Courant et al., 1928].

$$\frac{v.\Delta t}{\Delta x} < C \tag{2.34}$$

where C is governed by the particular problem and is typically < 1.

2.2.1 Central Difference

The derivative of a numerical quantity on a regularly spaced grid can be simply derived from the difference in value between one grid point and the next in either forward or backward differencing, however this is only accurate to first order. The central difference is derived from taking the difference between the Taylor expansions of $f(x \pm h)$, $f(x \pm 2h)$ etc.

$$f(x \pm h) = f(x) \pm hf'(x) + \frac{h^2}{2}f''(x) \pm \frac{h^3}{6}f^{(3)}(x) + O_{1\pm}(h^4) \tag{2.35}$$

So that

$$f(x+h) - f(x-h) = 2hf'(x) + \frac{h^3}{3}f^{(3)}(x) + O_1(h^4) \tag{2.36}$$

For a function evaluated on a uniform grid, the derivative accurate to higher order requires a stencil of N points around the central point. Using the notation $f(x + kh) = f_k$

$$N = 2 \quad f'(x) \approx \quad \frac{f_1 - f_{-1}}{2h} \tag{2.37}$$

$$N = 4 \quad f'(x) \approx \quad \frac{f_{-2} - 8f_{-1} + 8f_1 - f_2}{8h} \tag{2.38}$$

Similarly the by subtracting the Taylor series in such a way to just leave the 2nd derivatives, the numerical approximations are

$$N = 3 \quad f''(x) \approx \quad \frac{f_{-1} - 2f_0 + f_1}{h^2} \tag{2.39}$$

$$N = 5 \quad f''(x) \approx \quad \frac{-f_{-2} + 16f_{-1} - 30f_0 + 16f_1 - f_2}{12h^2} \tag{2.40}$$

The higher accuracy of a larger stencil comes at a cost of more computation, and the assumption that the function is sufficiently smooth for the higher order terms of the Taylor expansion to converge. This can fail if, for instance, there are discontinuities (shocks) in the simulation. There also comes a point where the round-off error due to the limited floating point precision exceeds the truncation error from the higher order terms in the Taylor series expansion. So careful evaluation of the cost/benefit needs to be considered, as adding more terms may not increase the overall accuracy of the model.

In moving from 1D to 2 & 3 dimensional problems the simplest approach is to

just consider each dimension independently and ignoring the diagonal terms. This gives a simple algorithm but leads to inaccuracies at the scale of the stencil size, where it takes several time-steps for changes to propagate in off-axis directions. This can lead to what is known as the chequerboard instability, whereby the decoupled alternate grid cells oscillate around the smooth value. Coupling the diagonal terms can be achieved via a small artificial diffusion slightly above the necessary numerical diffusion term required to cancel the next order error introduced via the Taylor approximation. The alternative often used in magnetohydrodynamics is to use a staggered grid such as the Yee scheme[Yee, 1966], where the electric field is defined on the edges of the grid cells, the magnetic field at the centre of the faces, with the velocity and scalar quantities such as density and temperature at the cell centre. For non-orthogonal curvilinear grids the form of the metric tensor and jacobian also become important choices for the numerical scheme.

2.2.2 Runge-Kutta

Similar arguments to the spatial derivatives come when considering the evolution of the quantities in time by the numerical integration of the PDEs. The goal being that given the state of the system at time t, the evaluation of each PDE leads to the new values at $t + \Delta t$. The Euler method is simply

$$f(\mathbf{x}, t + \Delta t) = f(\mathbf{x}, t) + \Delta t \frac{\partial f(\mathbf{x}, t)}{\partial t} \tag{2.41}$$

However, this method which only uses the derivative at the start of the interval, is only accurate to one power of the step-size smaller than the error on the derivative[Press et al., 2007, p907]. There are various other methods that take a trial step to the midpoint of the interval and re-evaluate the time derivative there. A popular algorithm that is sufficiently accurate for our purposes is the fourth-order Runge-Kutta. Here, in each time-step the derivative is evaluated four times: once at the initial point, twice at trial midpoints and once at a trial endpoint. These values are then combined with an appropriate weighting to find the new function

value to fourth order accuracy. For The formula is expressed as follows

$$\begin{aligned} k_1 &= \Delta t \frac{\partial f(x,t)}{\partial t} \\ k_2 &= \Delta t \frac{\partial f(x + k_1/2, t + \Delta t/2)}{\partial t} \\ k_3 &= \Delta t \frac{\partial f(x + k_2/2, t + \Delta t/2)}{\partial t} \\ k_4 &= \Delta t \frac{\partial f(x + k_3, t + \Delta t)}{\partial t} \end{aligned}$$

$$f(x, t + \Delta t) = f(x,t) + \frac{1}{6}k_1 + \frac{1}{3}k_2 + \frac{1}{3}k_3 + \frac{1}{6}k_4 + O(\Delta t^5) \tag{2.42}$$

For systems that evolve over time an adaptive method of determining the appropriate time-step for a given error. One such method is the Dormand-Prince[Dormand and Prince, 1980] fifth order Runge-Kutta, whereby the next term in the Taylor expansion is calculated to give an estimate of the truncation error, the step-size can then be adjusted accordingly to ensure accuracy is maintained. Other more elaborate algorithms include the Bulirsch-Stoer and Predictor-Corrector methods. However, for the scenarios expected to be studied in this work regarding instabilities in turbulent plasmas the basic Runge-Kutta should be sufficient since the gradients involved will not be high enough to constitute shocks.

2.2.3 MPI & OpenMP

In order to make any code as portable as possible (and not re-invent the wheel), the use of established, preferably open-source, standard libraries and application programming interfaces (APIs) is required. In the case of large scale parallel programs this means MPI and OpenMP. OpenMP is a simple scheme, built into most modern compilers, suited to multi-core workstations and moderate size shared memory systems, in which by added a few simple directives to standard C code around elements such as loops the task can be split into multiple threads and shared over several processor cores. To scale upto much larger systems where each node has it's own local memory, the Message Passing Interface (MPI) is used. Here multiple copies for the program are started on each node. Each node then works out where it is in the whole domain and works on its part of the problem, passing 'messages' of the changes in the boundary layer around the edge of the grid to the corresponding nodes via a high bandwidth, and more importantly low-latency, interconnect such as Infiniband.

The specification for MPI includes a set of functions explicitly designed for

domain decomposition problems, and as such make the handling of boundary conditions relatively trivial. The scaling efficiency of the parallel program is then a combination of the calculation time for each sub-grid with the communication overhead of passing all the new state in the boundary layer or ghost zones.

The hybrid OpenMP/MPI approach allows efficient use of multi-core/multi-chip hardware such that in our case each node has two Xeon X5650 CPUs each with 6 cores. Scheduling the simulation with 6 OpenMP threads per MPI task then enables efficient used of the level 1 and 2 CPU cache on each chip. This also avoids the issue of the 12 cores per node not dividing evenly when setting up jobs to divide grids typically defined using powers of two grid cells in each direction. The other aspect is that as the number of MPI tasks rises for a given resolution of simulation grid then the surface area to volume ratio of each MPI process' arrays rises. Reducing the relative number of MPI processes to CPU cores reduces the communications overhead governed by the size of the surface of each domain.

2.3 A simple two-fluid code

A simple 3D fluid code was developed by the author in C, using MPI and OpenMP to perform domain decomposition of a Cartesian grid. The partial differential equations outlined above were expressed using second or fourth order central differences in space, and evolved in time using a standard explicit fourth order Runge-Kutta scheme with a fixed time step, or an adaptive time step scheme using the method of Cash and Karp [1990].

The 3D arrays were created in C to ensure a contiguous block of memory, which is referenced via pointers to enable easy element referencing via standard `array[i][j][k]` notation, whilst also allowing efficient vector and matrix operations through the BLAS numerical library functions or the Intel optimised Math Kernel Library (MKL) equivalent if available.

Various initial condition scenarios, and algorithms were investigated as a pedagogical exercise to gauge the importance and sensitivity of alternative expressions for the various terms in the fluid equations to numerical errors. For example in the continuity equation the conservative form, using divergence of the flux $\nabla \cdot (n\mathbf{v_i})$, requires looping though the data twice, as shown in this code snippet:

```
#pragma omp parallel for private(i,j,k)
for(i=0; i < p->grid.z; i++){
    for(j=0; j < p->grid.y; j++){
        for(k=0; k < p->grid.x; k++){
            flux[i][j][k] = scalarMultVect( nzero[i][j][k] + p->n[i][j][k],p->s[1].v[i][j][k]);
        }
    }
```

```
}
#pragma omp parallel for private(i,j,k)
for(i=ghost; i < p->grid.z-ghost; i++){
    for(j=ghost; j < p->grid.y-ghost; j++){
        for(k=ghost; k < p->grid.x-ghost; k++){
            derivs->n[i][j][k] = -Div(flux,i,j,k, p->d);
        }
    }
}
```

wheras, if expressed as separate advection, $\mathbf{v_i} \cdot \nabla n$, and compression $n \nabla \cdot \mathbf{v_i}$; more calculation is needed but only involves traversing the arrays in memory once, as follows

```
#pragma omp parallel for private(i,j,k, advection, compression)
for(i=ghost; i < p->grid.z-ghost; i++){
    for(j=ghost; j < p->grid.y-ghost; j++){
        for(k=ghost; k < p->grid.x-ghost; k++){
            advection = -vdotgrad(p->s[1].v[i][j][k], p->n, i,j,k,p->d);
            advection += -vdotgrad(p->s[1].v[i][j][k], nzero, i,j,k,p->d);
            compression = -(p->n[i][j][k]+nzero[i][j][k]) * Div(p->s[1].v, i,j,k,p->d);
            derivs->n[i][j][k] = advection + compression;
        }
    }
}
```

Here we also see the `#pragma` keyword of the OpenMP directive instructing the compiler where to perform the loop parallelisation. The conservative form, as the name suggests, yields reduced errors in the conservation of total number density over time. The dissipative terms in the momentum and energy equations are more difficult to express in a fully conservative form.

2.3.1 Geometry and Vector Operators

The computational grid is implemented in a way such that by selecting arguments in the `Makefile` the code is compiled with either cartesian, cylindrical, or toroidal geometry. The vector operators for Div, Grad, Curl, etc. are overloaded with the appropriate function with the jacobian and required metric tensor components calculated during initialisation and stored in lookup tables. For example the advective operator $(\mathbf{v}.\nabla)f$ in toroidal coordinates is defined as:

```
inline double vdotgrad(const vect v, double ***f, int i, int j, int k, vect d){
    double g;
    double r= rTable[k];
    double R= RRTable[j][k];

    g  = v.z*(f[i+1][j][k] - f[i-1][j][k])/(2.0*d.z*R);
    g += v.y*(f[i][j+1][k] - f[i][j-1][k])/(2.0*d.y*r);
    g += v.x*(f[i][j][k+1] - f[i][j][k-1])/(2.0*d.x);
    return g;
}
```

For toroidal and cylindrical grids the minimum radial coordinate is specified in the `input.dat` file as, for example `rmin=0.3`, with the limiting factor begin the restric-

tion on the poloidal CFL condition near the axis. Figure 2.1 shows an example of a toroidal simulation with a grid major radius of $R_0 = 5$m and circular minor radius of $a = 1$m. The equilibrium is defined via the analytical Soloviev form[Soloviev, 1975], and so the field is not aligned with the grid, with a Shafranov shift of 0.1m between the magnetic axis and the geometric axis of the surface at $r = a$. The

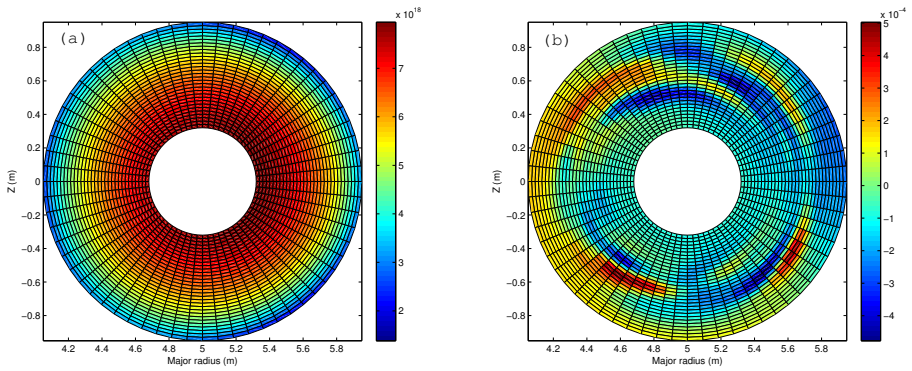

Figure 2.1: Low resolution example of a circular cross section poloidal slice through a toroidal simulation, to highlight the grid topology, showing (a) equilibrium density n_0 and (b) density fluctuations $\tilde{n}/n_0$.

inner and outer boundaries are configured with fixed density and temperature, with a level of damping, increasing towards the boundary, applied to the perturbed quantities in the edge grid cells to avoid instabilities. This non-aligned geometry is only viable at large aspect ratios, so the next stage of development would have been to move to a coordinate system aligned to the poloidal flux surfaces, with generalised vector operators in axis-symmetric curvilinear coordinates. However, due to time constraints, and requirement to match the experimental conditions in MAST it was decided to move to a more established code `CENTORI` as described in chapter 4.

2.4 Waves in simulated plasmas

The solutions of the ideal MHD equations for perturbations in a background magnetized plasma can be expressed in terms of wave equations with different characteristic speeds. The non-ideal resistive, hall, and other terms of the two-fluid formulation add additional modes and modify the ideal modes. These wave equations are expressed by separating the terms into those parallel and perpendicular to the background magnetic field. The characteristics of these waves can be used in

simple test cases to verify a numerical model is stable and that waves propagate at the expected speeds.

2.4.1 Alfvén waves

Originally postulated by Hannes Alfvén [Alfvén, 1950], and later observed experimentally, Alfvén waves are transverse displacements of the velocity and magnetic field and propagate along the direction of the magnetic field. An analogy can be made with waves on a stretched string under tension T, and mass per unit length ρ_m; the speed of the wave is then $v = \sqrt{T/\rho_m}$. A magnetic field is under tension as expressed via the Maxwell stress tensor, $T = B^2/\mu_0$ per unit area [Sawnson, 2008]. The Alfvén wave equation is given in terms of the perturbation in the parallel current $\tilde{\mathbf{j}}_{\parallel}$ by

$$\left[\frac{\partial^2}{\partial t^2} - V_A^2(\mathbf{b}\cdot\nabla)^2\right]\tilde{\mathbf{j}}_{\parallel} = 0 \tag{2.43}$$

which gives a dispersion relation $\omega^2 = V_A^2 k_{\parallel}^2$ where the Alfvén speed is given by

$$V_A = \frac{B_0}{\sqrt{\mu_o \rho_m}} \tag{2.44}$$

2.4.2 Magnetoacoustic waves

In non-ionised gases longitudinal pressure waves simply travel at the sound speed $c_s = \sqrt{(}\gamma p/\rho)$, where γ is the adiabatic index, p is the pressure and ρ is the mass density, in plasmas the coupling with the magnetic pressure, yields a more complex solution. In terms of the total pressure perturbation $\tilde{p}$ the magnetoacoustic wave equation is

$$\left[\frac{\partial^4}{\partial t^4} - (c_s^2 + V_A^2)\nabla^2 + c_s^2 V_A^2(\mathbf{b}.\cdot\nabla)^2\nabla^2\right]\tilde{p} = 0 \tag{2.45}$$

and corresponding dispersion relation

$$\omega^4 - (c_s^2 + V_A^2)k^2\omega^2 + c_s^2 V_A^2 k_{\parallel}^2 k^2 = 0. \tag{2.46}$$

Solving for ω^2 respect to the wavenumber k, there are two solutions, the fast (plus sign), and slow (minus sign), magnetoacoustic wave

$$\omega^2 = \frac{1}{2}(c_s^2 + V_A^2)k^2\left[1 \pm \sqrt{(c_s^2 + V_A^2)^2 - 4c_s^2 V_A^2 \frac{k_{\parallel}^2}{k^2}}\right] \tag{2.47}$$

A simulation on a periodic Cartesian grid, with a constant magnetic field

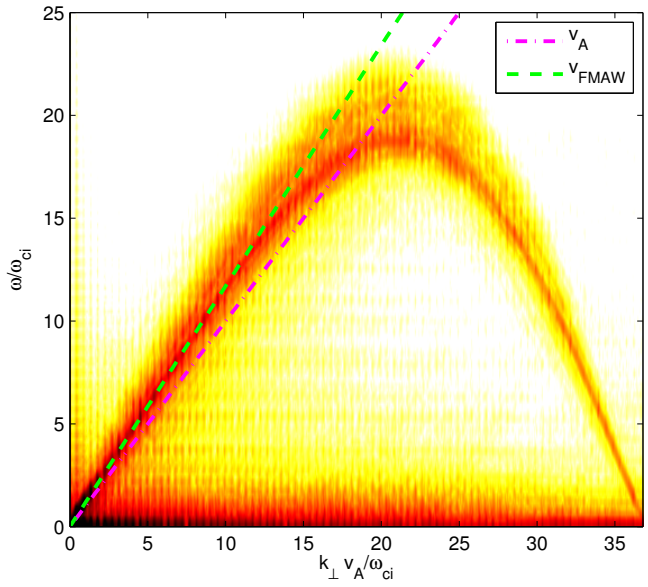

Figure 2.2: Perpendicular fast-magnetoacoustic wave (FMAW) dispersion compared to the Alfvén speed V_A, showing numerical roll-off at the grid scale

$\mathbf{B} = B_0\hat{\mathbf{z}}$ and uniform density and temperature, was run with seeded with perturbations in ion velocity, and density in all directions with wavelengths up to two-thirds of the Nyquist limit for the grid spacing, and random phases. After an initial relaxation, the frequency of the oscillations parallel and perpendicular to the imposed field were evaluated with respect to the wavenumber k, by taking (x,t) and (z,t) slices through the 4D (x,y,z,t) file output and performing a 2D Fast Fourier Transform (FFT) to yield the perpendicular and parallel dispersion relations as shown in figures 2.2 and 2.3. In the perpendicular direction the dominant wave mode is the fast-magnetoacoustic wave, travelling at a slightly higher velocity than the Alfvén speed. The simulation cannot model the physics accurately at all scales and rolls off as the wavenumber approaches the grid scale. For this reason it is necessary to run at a sufficient resolution to ensure the smallest scale of interest is at least double the limiting grid scale. Also it is necessary to add sufficient numerical dissipation at small scales to avoid aliasing artefacts.

In the parallel direction waves can exist in two polarisations with respect to the magnetic field, in addition to the longitudinal compression along the field line. This leads to three distinct branches. The fluctuations in pressure are dominated by the ion acoustic mode, i.e. sound waves, see figure 2.3(a). Whereas the fluctuations in B_y show the combination of right and left polarised waves, with dis-

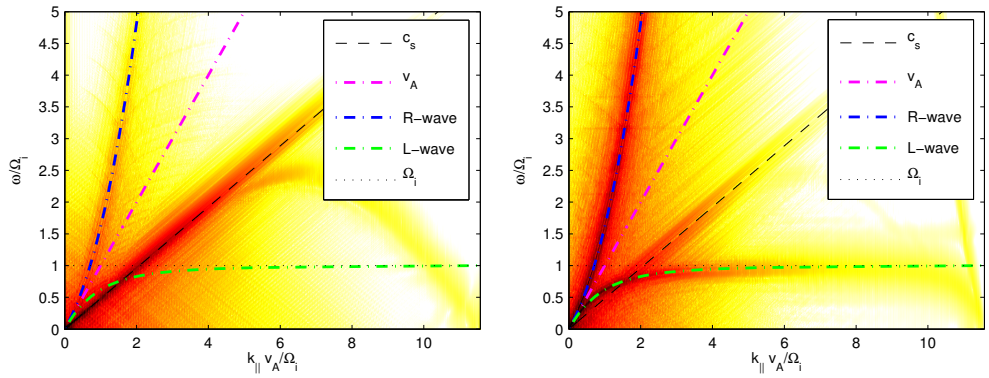

(a) p_i (b) B_y

Figure 2.3: Parallel wave dispersion in a uniform magnetic field

persion governed by the relative frequency of the fluctuation to the ion and electron gyro-frequencies:

$$\frac{k^2c^2}{\omega^2} = \frac{\omega^2 \mp \omega\Omega_i - \Omega_e\Omega_i - \omega_{pe}}{(\omega \pm \Omega_i)(\omega \mp \Omega_e)}. \tag{2.48}$$

Some coupling also exists to the acoustic branch, as shown in figure 2.3(b). The left handed branch asymptotes to the ion cyclotron frequency at large $k_\parallel$. However, the right handed 'whistler' mode frequency rises as $k_\parallel^2$. Physically this should roll off and asymptote to the lower-hybrid frequency $\omega_{\mathrm{LH}}^2 = (\Omega_e\Omega_i\omega_{pi}^2)/(\Omega_e\Omega_i + \omega_{pi}^2)$, but given the omission of electron inertia in the model, will rise without bound. For most simulations this is not an issue as the whistler frequency will, as with all modes, roll over and return to zero at the grid scale, thus provided there is numerical dissipation to damp any high k fluctuations, the low frequency fluctuations should behave in a physically correct manner.

2.5 Turbulence

After the early formulation of an ideal incompressible fluid by Euler [1755] the incorporation of a dissipation term by Navier [1822], explained as viscosity by Stokes [1845], and given suitable boundary conditions, yields an equation that is believed to encapsulate all laminar and turbulent flows in ideal incompressible fluids; the Navier-Stokes equation:

$$\frac{\partial \mathbf{v}}{\partial t} + \mathbf{v}\cdot\nabla\mathbf{v} = -\nabla p + \nu\nabla^2\mathbf{v}, \tag{2.49}$$

$$\nabla\cdot\mathbf{v} = 0 \tag{2.50}$$

The key parameter in fluid flow is the ratio of the velocity to the kinematic viscosity (defined as the dynamic viscosity μ, divided by the density ρ), normalised to a characteristic scale length, e.g. diameter of a pipe, known as the Reynolds number.

$$Re = \frac{Lv}{\nu} \sim \frac{[\mathbf{v} \cdot \nabla \mathbf{v}]}{[\nu \nabla^2 \mathbf{v}]} \tag{2.51}$$

This dimensionless quantity gives a measure of the relative strength of the inertial advective term and the viscous term. Where the viscosity is small i.e. at large Reynolds numbers, laminar flow becomes unstable and turbulence can develop.

Plasma dynamics cannot be characterised by the same Re number since for plasmas the dissipation mechanisms are very different. Rather than simple diffusive molecular dissipation one has to consider, for example, wave–particle and gyro–resonant interactions. For MHD the role of currents and resistivity can similarly considered. The leading terms of the electron momentum equation, or Ohm's law can be substituted into Faraday's law to get

$$\frac{\partial \mathbf{B}}{\partial t} = -\nabla \times (-\mathbf{v} \times \mathbf{B} + \eta \mathbf{J}) = \nabla \times (\mathbf{v} \times \mathbf{B}) + \eta \nabla^2 \mathbf{B} \tag{2.52}$$

Taking the ratio of the inductive and resistive terms then gives a magnetic Reynolds number.

$$R_m = \frac{Lv}{\eta} \sim \frac{[\nabla \times (\mathbf{v} \times \mathbf{B})]}{[\eta \nabla^2 \mathbf{B}]} \tag{2.53}$$

It can be seen from the form of these equations that the collisional effects, here reduced to a simple classical resistivity play a crucial role in the nature of turbulence in magnetised plasmas. It is sometimes useful also to characterise a plasma via the Alfvén speed rather than the fluid velocity, using the Lunquist number

$$S = \frac{Lv_A}{\eta} \tag{2.54}$$

which is more appropriate in static situations, in particular the growth rate of resistive instabilities, during the linear phase. However for strongly non–linear turbulent systems R_m is of more significance [Biskamp, 1997, p23].

2.5.1 Energy and Enstrophy

The characteristic scaling of turbulence was long appreciated on an empirical level, however, it was not until Kolmogorov [1941a,b,c] that observations could be put on a firmer footing.

3D hydrodynamic turbulence

The fluid kinetic energy in the absence of any external forcing can be written as

$$E = \int \frac{1}{2}\rho|\mathbf{v}|^2 d^3r. \tag{2.55}$$

where ρ here, is the mass density. From the definition (2.55) and applying the vector identity:

$$\mathbf{v}\cdot\nabla\mathbf{v} = \frac{\nabla|\mathbf{v}|^2}{2} + (\nabla\times\mathbf{v})\times\mathbf{v} \tag{2.56}$$

The change of energy, E, of an incompressible fluid can be written as [Frisch, 1995]

$$\frac{\partial E}{\partial t} = -\nu\int \rho(\nabla\times\mathbf{v})^2 d^3r = -\nu\int \rho|\mathbf{w}|^2 d^3r \tag{2.57}$$

Where we introduce the vorticity $\mathbf{w}\equiv\nabla\times\mathbf{v}$. Enstrophy is then defined as $|\mathbf{w}|^2$, such that the total entropy, Z is

$$Z = \int \frac{1}{2}\rho|\mathbf{w}|^2 d^3r \tag{2.58}$$

so that relation (2.57) can now be written in a concise form as:

$$\frac{\partial E}{\partial t} = -\frac{2\nu Z}{\int \rho d\mathbf{v}} \tag{2.59}$$

In the trivial case where $\nu = 0$ kinetic energy is conserved. However in the limit as $\nu\to 0$ the mean energy dissipation rate per unit mass reaches a constant value

$$\lim_{\nu\to 0}\frac{2\nu Z}{\int \rho d\mathbf{v}} = \epsilon \tag{2.60}$$

Dimensionally the energy dissipation rate ϵ has units $[m^2 s^{-3}]$. Expressing in terms of wavenumber k, the total turbulent kinetic energy over all scales is defined as

$$E_T = \int_0^\infty E(k)dk \tag{2.61}$$

so

$$[E(k)] = [E_T]/[k] = [m^3 s^{-2}] \tag{2.62}$$

by comparison of units, a form for energy spectrum can in terms powers of the energy dissipation rate and wavenumber

$$[\epsilon^{2/3}k^{-5/3}] = [m^3 s^{-2}] \tag{2.63}$$

$$\Rightarrow E(k) \propto \epsilon^{2/3} k^{-5/3} \tag{2.64}$$

so

$$E(k) = C\epsilon^{2/3} k^{-5/3} \tag{2.65}$$

where the Kolmogorov constant C is found experimentally to be $C \simeq 1.5$.

2D hydrodynamic turbulence

In the case of a two dimensional system the vorticity only has one non-zero component perpendicular to the plane of the velocity, and can be written in terms of a stream-function ψ, defined via the velocity $\mathbf{v} = \nabla \times \psi$, where $\psi = (0, 0, \psi)$. The scalar non-zero component of the vorticity is then

$$w = -\nabla^2 \psi. \tag{2.66}$$

The two-dimensional Navier-Stokes equation then becomes

$$\frac{\partial w}{\partial t} + \mathbf{v} \cdot \nabla w = \nu \nabla^2 w - \alpha |\mathbf{v}| + f_w, \tag{2.67}$$

where f_w represents a driving term 'stirring' the fluid at large scales to counteract the dissipation by viscosity ν and friction α of the thin 2D slice in a 3D system. The Poisson equation (2.66) can then be solved via suitable boundary conditions. In the absence of driving or friction terms and given periodic boundary conditions it can be shown that [Musacchio, 2003]

$$\frac{\partial Z}{\partial t} = \int \rho |\nabla w|^2 d^2 r. \tag{2.68}$$

Then the conservation of energy takes the form

$$\lim_{\nu \to 0} \frac{\partial E}{\partial t} = \lim_{\nu \to 0} 2\nu Z = 0. \tag{2.69}$$

Thus, unlike its three dimensional counterpart, in two-dimensional turbulence in the limit of $\nu \to 0$ the viscous dissipation of energy vanishes, and both energy and enstrophy are conserved. This is due to the absence of 'vortex stretching' via the term $(\mathbf{w} \cdot \nabla)\mathbf{v}$.

2.6 Plasma turbulence

Nearly all astrophysical and laboratory plasmas are turbulent. Plasmas support a plethora of waves, instabilities and the dynamics are usually nonlinear. While turbulence can be driven in plasma by many mechanisms, here, the main considerations are given to the presence of plasma currents and the existence of spatial gradients. Other than the materials and engineering issues, we stress that plasma turbulence is one of the main physics challenges in developing nuclear fusion into a viable energy source.

The extensive research done during the 1950s and 1960s confirmed that even when large scale MHD instabilities, such as kink and ballooning mode instabilities, are avoided by suitable choice of equilibrium configuration, the micro-instabilities still increase the heat transport beyond classical and neo-classical estimates. For example micro-instabilities extract energy from spatial gradients, which are always present in a tokamak configuration. Other mechanisms could be related to neutral beam injection, radio frequency heating, pellet injection etc.

Unlike the space plasma, which often have Beta parameter close to one, magnetically confined fusion plasmas, have a strong magnetic field giving a Beta parameter of a few percent at most. This introduces a strong anisotropy. The restriction of flow across field lines, in strongly magnetized plasmas limits the rotation of vorticity vector, and causes a large separation in $k_{\|}$ and $k_{\perp}$ of the turbulence. This makes many aspects similar to the 2D hydrodynamic case. This characteristic is utilised in many reduced models such as Hasegawa and Mima [1978], and subsequent Hasegawa and Wakatani [1983].

2.6.1 Current-Driven Turbulence

There are many classes of current driven instability that can drive turbulence, including resistive or neoclassical tearing modes. If a plasma carries a high current, such that the electron drift velocity relative to the ions $u \equiv -j/en_e$ is higher than the electron thermal velocity then the flow becomes unstable exciting an electrostatic wave with a phase velocity in-between the drift and thermal velocities. This is known as the two-stream instability, and after initial heating, the current continues to drive turbulent mixing and manifests as an anomalous resistivity $\eta = m_e\nu_{\text{eff}}/ne^2$. Avoiding instabilities due to high currents are one advantage of the stellarator approach, as the necessary twist in magnetic field is created by external coils rather than the large toroidal current of a tokamak.

The exact nature and growth mechanisms of these instabilities is dependent

on the difference of the ion and electron temperature, and can further be modulated by the presence of impurity ions. The deviation of each species velocity distribution from thermal equilibrium is also affected. By using a two-fluid description the electron and ion temperatures can be varied, but to encompass the deviation from a Maxwellian velocity distribution a fuller kinetic description, such as that used in gyro-kinetic codes is needed.

As a rough indication of current density which is required to bring the electron drift velocity to the same order as the electron thermal velocity; for a plasma at $T_e = 1\text{keV}$, and density $n_e = 10^{-19}\text{m}^{-3}$

$$|j| = env_{th,e} = \sqrt{\frac{eT_e}{m_e}} \simeq 10^7\,\text{Am}^{-2} \tag{2.70}$$

The plasmas being studied in this thesis are primarily low current discharges, so no significant current driven modes should be present.

2.6.2 Spatial Gradient Driven Turbulence

In a non-uniform magnetised plasma ion-acoustic waves are split into two branches with different phase velocity parallel and perpendicular to the field, due to the presence of diamagnetic currents $\mathbf{j}_s = q_s n_e \mathbf{v}_{ds}$ for species s. Even for small perturbations these diamagnetic currents drive low frequency ($\omega \ll q_s B/m_s$) waves with $\mathbf{k}$ almost parallel to $\mathbf{B}\times\nabla p_s$ are unstable [Horton, 1999]. These drift waves increase cross-field transport of particle energy and momentum.

The magnetic shear associated with drift-wave turbulence can lead to zonal-flows (see section 2.9), which are believed to be related to new confinement regimes with transport barriers.

2.7 Drift Waves

Consider the situation in figure 2.4, where a constant density gradient dn_0/dx exists (in the radial direction) perpendicular to the magnetic field $\mathbf{B} = B\hat{\mathbf{z}}$. Then, a perturbation of the form

$$n = n_0 e^{i(k_y + k_z - \omega t)} \tag{2.71}$$

with $k_y \gg k_z > 0$, will propagate in the poloidal $\hat{y}$ direction with phase velocity $v_{dw} = \omega/k_y$. Electrons move along the field to maintain thermal equilibrium and

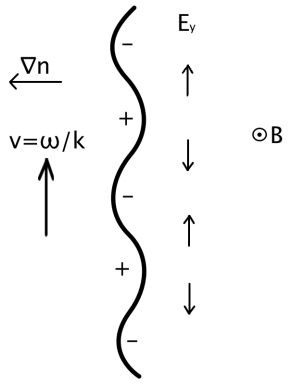

Figure 2.4: Schematic of a drift wave. A contour of perturbed density creates regions of fluctuating potential $\tilde{\phi}$ indecated by $+/-$, which propagate in the y-direction.

quasineutrality according to the Boltzmann response

$$n = n_0 + \tilde{n} = n_0 e^{e\phi/T_e} \approx n_0 \left(1 + \frac{e\phi}{T_e}\right). \tag{2.72}$$

The governing continuity, momentum and energy equations, are expressed in linearised form (as described in [Miyamoto, 2006]) as

$$-i\omega\tilde{n} + \tilde{v}_x \nabla n_0 + n_0 i k_z \tilde{v}_z = 0 \tag{2.73}$$

with perpendicular velocity component, due to $\mathbf{E} \times \mathbf{B}$ drift

$$\tilde{v}_x = E_y/B = ik_y\tilde{\phi}/B. \tag{2.74}$$

The corresponding parallel equation of motion is

$$-i\omega n m_i \tilde{v}_z = -ik_z(\tilde{p}_i + en_0\tilde{\phi}). \tag{2.75}$$

and adiabatic energy equation

$$-i\omega\left(\frac{\tilde{p}}{p} - \frac{5}{3}\frac{\tilde{n}}{n}\right) - \frac{ik_y\tilde{\phi}}{B}\left(\frac{1}{L_{T_i}} - \frac{2}{3}\frac{1}{L_n}\right) = 0 \tag{2.76}$$

where $L_{T_i} = T_i/\nabla T_i$, and $L_n = n_0/\nabla n$. If we assume cold ions $1/L_{T_i} \approx 0$ and $\tilde{p}_i \ll en_0\tilde{\phi}$, we arrive at the electron drift velocity

$$v^*_{dw} \equiv \frac{\omega^*_{ne}}{k_y} \equiv \frac{T_e}{enB}\frac{dn_0}{dx} = \frac{T_e}{eB}\frac{1}{L_n} \tag{2.77}$$

In this linearised description $\tilde{n}$ and $\tilde{\phi}$ remain in phase and the waves simply propagate in the y direction with no net transport down the gradient. If however, non-adiabatic coupling exists between the density and potential then a phase difference can occur resulting in net transport.

2.7.1 Ion Temperature Gradient (ITG) Turbulence

In order to consider the temperature gradient contribution to turbulence driving mechanisms, as distinct from the density gradient driven drift waves, we start from equation (2.76), but no longer take $T_i = 0$. For $k_\perp \rho_i \ll 1$ the motion perpendicular to $\mathbf{B}$ is given by the $\mathbf{E}\times\mathbf{B}$ velocity and is incompressible. Leading to the ion density perturbations being governed by compression along the field lines. An instability occurs if the frequency of the perpendicular $\mathbf{E}\times\mathbf{B}$ advection of a pressure perturbation is faster than the propagation of the mode along the field line $k_\parallel c_s$, where $c_s^2 = 2T_e/m_i$. Using the ion diamagnetic drift frequency, defined as

$$\omega_{pi}^* = \frac{k_\perp T_i}{eB}\left(\frac{|\nabla p_0|}{p_0}\right) = \frac{k_\perp T_i}{L_p eB} \tag{2.78}$$

in the limit $|\omega_{pi}^*| \gg |k_\parallel c_s|$ the dispersion relation becomes [Cowley et al., 1991]

$$\omega^3 = \frac{k_\parallel^2 c_s^2}{2}\omega_{pi}^* \tag{2.79}$$

This cubic relationship yields a $\pi/2$ phase difference between the density maximum and the $\mathbf{E}\times\mathbf{B}$ flow from the colder side of the temperature gradient, but a $\pi/3$ lag of the minimum pressure with respect to the density maximum. For instability the temperature gradient must be sufficiently large compared to the density gradient

$$\eta_i = \frac{d\log T_i/dx}{d\log n/dx} = \frac{d\log T_i}{d\log n} > \eta_c \tag{2.80}$$

where the critical level $\eta_c \sim 2/3$, is such that the temperature gradient term inside the brackets of Eqn. (2.76) becomes comparable to the density term.

Similar electron temperature gradient (ETG) modes exist, but at the much smaller scale/time of the electron gyro radius/frequency. Although the ETG modes are usually separated in scale to such an extent from ITG modes that they do not couple directly to each other, neoclassical trapped electron modes (TEMs) can bridge the gap, providing a hierarchy of interactions right from the smallest scales to global modes at the scale of the device.

2.8 Transport

The characteristics of heat and particle transport in plasmas is greatly affected by the presence of a magnetic field. The influence of magnetic field is often expressed in terms of the plasma beta which is the ratio of the magnetic to the gas pressure.

$$\beta \equiv \frac{p}{B^2/2\mu_0} \tag{2.81}$$

In a typical tokamak $\beta \approx \epsilon^2 \ll 1$ where $\epsilon = r/R$ is the inverse aspect ratio. Spherical tokamaks such as MAST, have a smaller aspect ration, and so can potentially achieve a higher confinement for its size than conventional tokamak shapes such as JET and ITER. Most transport mechanisms are highly anisotropic and either dominate along the field or across it.

2.8.1 Classical diffusivity

Classical diffusion due to the collision of electrons and ions can be considered within the MHD framework in a tokamak provided the mean free path is shorter than the connection length. The particle flux down the density gradient can be given by

$$\Gamma = n\mathbf{v_i} = -D(x,t)\nabla n(x,t). \tag{2.82}$$

The diffusion coefficient, of the form $D = (\Delta x)^2/(\Delta t)$ can then be considered as a random walk with step length equal to the electron Larmor radius ρ_e at a rate given by the electron–ion collision frequency

$$\nu_{ei} = \frac{1}{\tau_{ei}} = \frac{\sqrt{2}nZ^2e^4\ln\Lambda}{12\pi^{3/2}\epsilon_0^2 m_e^{1/2}T_e^{3/2}}. \tag{2.83}$$

The classical diffusion coefficient is then given by [Miyamoto, 2006]

$$D_{ei} = (\rho_e)^2\nu_{ei} = \frac{nT_e}{\sigma_\perp B^2} \tag{2.84}$$

where $\sigma_\perp$ is the perpendicular conductivity.

2.8.2 Neoclassical diffusivity

Neoclassical diffusion is a kinetic effect and takes into account that when the perpendicular component $v_\perp$ of an ion/electron velocity is larger than the parallel com-

ponent such that

$$\frac{v_\perp}{v_\parallel} > \frac{1}{\sqrt{\epsilon}} \tag{2.85}$$

the particle is trapped on the outside of the torus were the magnetic field is weaker. These so called banana orbits change the dynamics of the ion and electron diffusion due to the change in collision frequency. Representative orbits of ions near the $q = 2$ and $q = 5$ surfaces are plotted in figure 2.5. In this figure, trajectories of ions with low pitch angle relative to the magnetic field, performing full 'passing' orbits of the tokamak are plotted in blue, while in red we have indicated ions with the same energy, but steeper pitch angle, such that the parallel component of the velocity is insufficient to overcome the mirror force on the high field side.

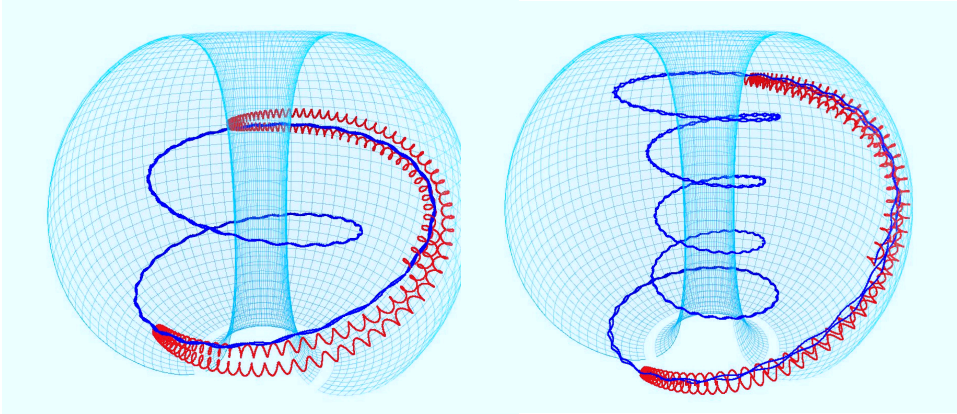

(a) $q = 2$ (b) $q = 5$

Figure 2.5: Representative ion orbits in MAST for low (blue) and high (red) pitch angles

Chang-Hinton formula

Various empirical relationships have been developed to provide suitable neoclassical diffusion coefficients across the different regimes such as [Chang and Hinton, 1982; Hazeltine et al., 1973], from the relatively collisionless core of a tokamak where the role of neoclassical banana orbits are important, to the more collisional edge region. In large tokamaks the diffusivity at intermediate radial positions is roughly constant forming a plateau region, however, in MAST this region is believed to be small. For ions the form of the equation in terms of the normalised radial coordinate ρ (as used in `CENTORI`, see chapter 4) is

$$\chi_{i,NC}(\rho) = \frac{K_{NC,i}\,\epsilon^{1/2}\rho_{pi}^2}{\tau_{ii}}$$

where τ_{ii} is the ion collision time and

$$K_{NC,i}(\rho) = \frac{0.66 + 1.88\epsilon^{1/2} - 1.54\epsilon}{1 + \sqrt{\nu_i^*} + 0.31\nu_i^*} + \frac{0.66}{0.31}\frac{\left((0.74)^2\epsilon^3\nu_i^*\right)}{1 + 0.74\nu_i^*\epsilon^{3/2}}$$

where $\epsilon = a\rho^{1/2}/R_0$ is the local inverse aspect ratio, ν_i^* is the normalised collision frequency, and $\rho_{pi} = \rho_i\langle B\rangle/\langle B_p\rangle$ is defined as a poloidal ion Larmor radius. A similar equation exists for the electrons.

2.8.3 Turbulent (Bohm and gyro-Bohm) diffusivity

The fluctuations within a plasma cause the diffusion to be higher than the classical rate above. Small micro-instablilites will drive drift waves, as described in Section 2.7. These $\tilde{n}_k$ and $\tilde{\phi}_k$ fluctuations, for each wavenumber k, will couple forming a cascade from the small scale, fed from the free energy in the density gradient, until non-linear interactions cause the fluctuations saturate at a level where the radial correlation length of the fluctuations correspond to the gradient scale length

$$|\tilde{n}_k| \approx |\nabla n_0|\Delta r \approx \frac{n_0}{k_x L_n}. \tag{2.86}$$

The total flux of $\Gamma = Dn_0/L_n$, gives diffusion coefficient as the sum over all modes k of [Miyamoto, 2006]

$$D = \left(\sum_k \frac{k_y L_n \gamma_k}{\omega_k^*}\left|\frac{\tilde{n}_k}{n_0}\right|^2\right)\frac{T_e}{eB} \tag{2.87}$$

where γ_k is the linear growth rate. This $1/B$ scaling of diffusion was observed experimentally by Bohm [1949] rather than the $1/B^2$ of classical diffusion above, with a coefficient of

$$D_{\text{Bohm}} = \frac{1}{16}\frac{T_e}{eB}. \tag{2.88}$$

In the toroidal geometry of a tokamak the diffusivity due to drift waves is modified, and is dependent on the shear of the q-profile $s \equiv rq'/q$. If the width of a drift wave mode Δr is less than the distance between rational surfaces $\Delta r_m = r((m-1)/n) - r(m/n)$, then the radial correlation length is [Miyamoto, 2006]

$$\Delta r = \rho_i\left(\frac{qR}{sL_p}\right)^{1/2}. \tag{2.89}$$

where L_p is the pressure gradient scale length. This changes the saturation point for the drift-wave turbulence, and the diffusion is found to scale as

$$D_{\text{gyro-Bohm}} \sim (\Delta r)^2 \omega_k^* \sim \left(\frac{qR}{sL_p}\right) \frac{\rho_i}{L_p} \frac{T_e}{eB} \tag{2.90}$$

2.9 Zonal Flows

Zonal features are found in many turbulent systems where there is sheared flow, such as the bands in the atmosphere of Jupiter [Williams, 1975], or the Jet streams on Earth. In atmospheres the shear is due to the variation of the Coriolis force with latitude, forming a Rossby wave [Charney, 1949], while in fusion plasma its origin lays in polarisation drift of the ions [Hasegawa and Mima, 1978].

In tokamaks, zonal flows are $n = 0, m \cong 0$ fluctuations of the electric field with finite radial wavenumber k_r, where m, n are the poloidal and toroidal mode numbers respectively. Zonal flows cannot directly tap the ∇n and ∇T energy sources to drive radial transport. Instead they must rely on non-linear interactions with all types of microinstabilites, often grouped generically together as 'drift waves' [Itoh et al., 2006]. They can then regulate the turbulent transport by shearing the eddies of the drift wave turbulence, extracting energy from them. This feedback mechanism forms a predator-prey type relationship between the zonal flows and the turbulence, which can manifest as steady, bursty or cyclic states.

The emergence of zonal flows can be demonstrated using simple reduced models such as the Hasegawa-Wakatani (HW) equations. This is derived by considering just the motion in a 2D plane perpendicular to a constant magnetic field. With the electron motion along the field modelled as a current with finite resistivity η.

$$J_\parallel = \frac{T_e}{e\eta}\left[\frac{\nabla_\parallel \tilde{n}}{n_0} - \frac{e\nabla_\parallel \tilde{\phi}}{T_e}\right] \tag{2.91}$$

This is characterised by the resistive coupling term $\alpha = T_e k_\parallel^2/(n_0 e^2 \eta \omega_{ci})$ in the Hasegawa-Wakatani (HW) equations, which in units normalised to the hybrid Larmor radius $\rho_s = \sqrt{m_i T_e}/eB$, ion cyclotron period ω_{ci}, and background density n_0, can be expressed as [Hasegawa and Wakatani, 1983]

$$\frac{\partial n}{\partial t} = -\kappa \frac{\partial \phi}{\partial y} + [n, \phi] + \alpha(\phi - n) + D\nabla^2 n \tag{2.92}$$

$$\frac{\partial w}{\partial t} = [w, \phi] + \alpha(\phi - n) + \mu\nabla^2 n \tag{2.93}$$

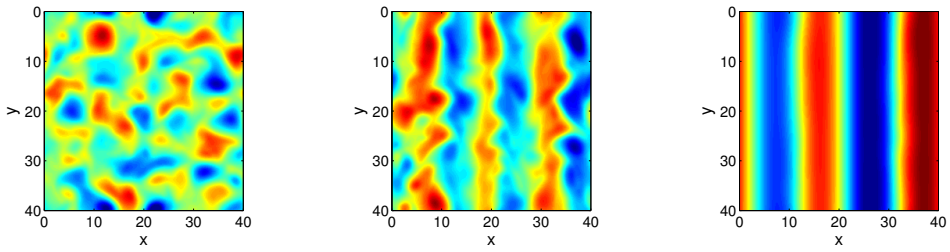

Figure 2.6: Snapshot of potential in a saturated quasi-stationary turbulent state for three cases: left where zonal flows are damped, middle where total kinetic energy is balanced between zonal flows and non-zonal drift wave component, and right – zonal flow dominated state (from [Dewhurst et al., 2010])

where the constant density gradient forcing term is $\kappa = -\partial \ln n_0/\partial x$, the vorticity $w = \nabla^2\phi$, and the Poission bracket $[A, B] = (\partial A/\partial x)(\partial B/\partial y) - (\partial A/\partial y)(\partial B/\partial x)$. In the limit $\alpha \gg 1$ the coupling is adiabatic and the equations reduce to the Hasegawa-Mima equation [Dewhurst et al., 2010], conversely if $\alpha \ll 1$ the equations reduce to the 2D hydrodynamic equation (2.67).

By artificially damping the mean flow in the y (i.e. zonal) direction Dewhurst et al. [2010] illustrated the transition from the saturated drift wave turbulent state to one in which the zonal flows are allowed to emerge, as shown in figure 2.6. In the standard HW equations, zonal flows quickly grow to dominate the potential fluctuations as in the right hand panel. By restricting (middle) or completely damping (left) the zonal component, the underlying turbulent fluctuations become apparent.

2.10 Geodesic acoustic mode

Postulated by Winsor [1968], and later observed experimentally, the geodesic acoustic mode (GAM) is a consequence of poloidal zonal flows causing an $m = 1$ oscillation in the density between the top and bottom of the tokamak, shown in figure 2.7. Since although $\mathbf{E}_r = -\nabla\phi$ of the zonal flow is roughly constant on the flux surface $\mathbf{v_E} = \mathbf{E}_r \times \mathbf{B}/B^2$ will be lower on the inner (high) field side than outboard side. In simplified terms the mode can grow if the pitch angle of the field is sufficiently close to toroidal that the parallel connection length between the top and bottom of the tokamak is sufficiently long that the ion flow along the field cannot adequately compensate for the poloidal flow. This results in a pile-up of density, and so pressure, at the top or bottom. The poloidal pressure gradient then creates a restoring force causing density to oscillate at a frequency proportional to the sound speed and

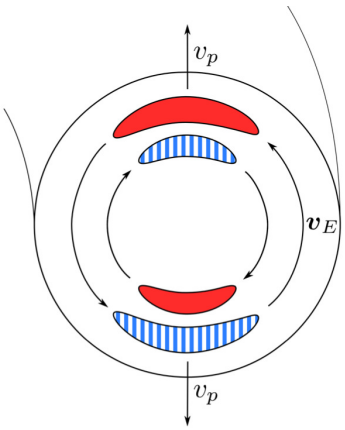

Figure 2.7: Sketch of a geodesic acoustic mode. Imbalance of zonal ExB-flow on high and low field side, leads to compression or expansion of the plasma (indicated by the filled and striped areas, respectively). Thus, an up-down antisymmetric m = 1 density perturbation arises, which is phase-delayed against the flow by $\pi/2$. This propagates outwards at phase velocity $v_p = \omega_{\mathrm{GAM}}/k_r$ (from [Hager and Hallatschek, 2009])

inversely to the major radius.

Following the derivation of Winsor we start with an ideal MHD model, neglecting time variations in $\mathbf{B}$, in which the perturbations obey

$$\rho\frac{\partial\tilde{\mathbf{v}}}{\partial t} = \tilde{\mathbf{J}}\times\mathbf{B} - \nabla\tilde{p} \tag{2.94}$$

$$\frac{\partial\tilde{\rho}}{\partial t} + \nabla\cdot\tilde{\rho}\mathbf{v} \tag{2.95}$$

$$\nabla\tilde{\phi} = \tilde{\mathbf{v}}\times\mathbf{B} \tag{2.96}$$

$$\nabla\cdot\tilde{\mathbf{J}} = 0 \tag{2.97}$$

$$\rho^{-\gamma}\frac{\partial\tilde{p}}{\partial t} - \gamma p\rho^{-\gamma-1}\frac{\partial\tilde{\rho}}{\partial t} + \tilde{\mathbf{v}}\cdot\nabla(p\rho^{-\gamma}) = 0 \tag{2.98}$$

Using an arbitrary flux surface function ψ such that $\mathbf{B}\cdot\nabla\psi = 0$, the perturbed velocity can be decomposed into components perpendicular to the flux surface $\tilde{v}_\psi$, parallel to the equilibrium B-field $\tilde{v}_b$, and third component perpendicular to both within the surface $\tilde{v}_s$

$$\tilde{\mathbf{v}} = \left(\tilde{v}_\psi\frac{\nabla\psi}{|\nabla\psi|^2} + \tilde{v}_s\frac{\mathbf{B}\times\nabla\psi}{B^2} + \tilde{v}_b\frac{\mathbf{B}}{B}\right)\exp(-i\omega t) \tag{2.99}$$

From the component of (2.96) parallel to $\mathbf{B}$, in this ideal case, the electrostatic

potential ϕ is a function of ψ alone, from the component along $\nabla\psi$ that $\tilde{v}_s = d\tilde{\phi}/d\psi$, and lastly that $\tilde{v}_\psi = 0$. This reduces (2.98) to

$$\tilde{p} = \left(\frac{\gamma p}{\rho}\right)\tilde{\rho} \tag{2.100}$$

Solving for $\mathbf{J}$ the divergence theorem converts the volume integral of (2.97) to the surface integral

$$\int \tilde{J}_\psi \mathcal{J} dS = 0. \tag{2.101}$$

Then using J_ψ, determined from the component of (2.94) in the $\mathbf{B}\times\nabla\psi$ direction

$$\tilde{v}_s = -\frac{i\gamma p}{\omega\rho^2}\int \frac{\mathbf{B}\times\nabla\psi\cdot\nabla\tilde{\rho}}{B^2}\mathcal{J}dS \Big/ \int \frac{|\nabla\psi|^2}{B^2}\mathcal{J}dS \tag{2.102}$$

similarly in the parallel direction

$$\tilde{v}_b = -\frac{i\gamma p}{\omega\rho^2}\mathbf{B}\cdot\nabla\tilde{\rho}. \tag{2.103}$$

Expanding (2.95), and multiplying by $\tilde{\rho}^*\mathcal{J}dS$ yields

$$\frac{\partial\tilde{\rho}}{\partial t}\tilde{\rho}^*\mathcal{J}dS = \left(-\nabla\rho\cdot\tilde{\mathbf{v}} - \rho\nabla\cdot\tilde{\mathbf{v}}\right)\tilde{\rho}^*\mathcal{J}dS. \tag{2.104}$$

The first term on the right hand side is zero since the perturbed velocity is within the flux surface and the equilibrium density gradient $\rho = \rho(\psi)$. Now, substituting in the non-zero components of $\tilde{\mathbf{v}}$

$$\begin{aligned}\frac{\partial\tilde{\rho}}{\partial t}\tilde{\rho}^*\mathcal{J}dS = &-\rho\nabla\cdot\left[\left(-\frac{i\gamma p}{\omega\rho^2}\int\frac{\mathbf{B}\times\nabla\psi\cdot\nabla\tilde{\rho}}{B^2}\mathcal{J}dS\Big/\int\frac{|\nabla\psi|^2}{B^2}\mathcal{J}dS\right)\frac{\mathbf{B}\times\nabla\psi}{B^2}\right.\\ &\left.+\left(-\frac{i\gamma p}{\omega\rho^2}\mathbf{B}\cdot\nabla\tilde{\rho}\right)\frac{\mathbf{B}}{B}\right]\tilde{\rho}^*e^{-i\omega t}\mathcal{J}dS.\end{aligned} \tag{2.105}$$

Then integrating by parts with respect to time and use of various vector identities to expand the divergence operator in order to cancel terms with $\nabla\cdot\mathbf{B}$ or curls of gradients; and realising, assuming steady state conditions, the time integral of just the perturbed density will average to zero, gives

$$\begin{aligned}\omega^2\int|\tilde{\rho}|^2\mathcal{J}dS = &\frac{\gamma p}{\rho}\left(\left|\int\tilde{\rho}\frac{\mathbf{B}\times\nabla\psi\cdot\nabla B^2}{B^4}\mathcal{J}dS\right|^2\Big/\int\frac{|\nabla\psi|^2}{B^2}\mathcal{J}dS\right.\\ &\left.+\int\frac{|\mathbf{B}\cdot\nabla\rho|^2}{B^2}\mathcal{J}dS\right).\end{aligned} \tag{2.106}$$

The second term of this wave equation is the ordinary sound wave along the field lines or ion acoustic mode (IAM), whereas the first is dependent on the curvature of $\mathbf{B}$ in the $\mathbf{B} \times \nabla\psi$ surface, and so is known as the Geodesic Acoustic Mode. The solution to this is dependent on the flux surface shape, but in the simplest case of a circular cross section and large aspect ratio can be found via Fourier expansion. Moving to toroidal (r, θ, φ) coordinates a circular cross section tokamak with toroidal field $B_T = R_0 B_0 / R$ the equilibrium magnetic field can be defined as

$$\mathbf{B} = \frac{B_0}{1 + (r/R_0)\cos\theta}[\mathbf{e}_\varphi + f(r)\mathbf{e}_\theta] \tag{2.107}$$

where $f(r) = r/q\sqrt{R_0^2 - r^2}$ is the rotational transform in terms of the safety factor q. Setting $\psi = r$, $\mathcal{J}dS = r(1+r/R_0\cos\theta)d\theta d\varphi$. Expanding $\tilde{\rho}$ for modes independent of toroidal angle φ gives

$$\omega^2 \int_0^{2\pi} |\tilde{\rho}|^2 d\theta = \frac{\gamma p}{\rho r^2(1+f^2)} \left(2r^2 \left| \int_0^{2\pi} \tilde{\rho} \left[\sin\theta + \frac{r}{2R_0}\sin 2\theta \right] d\theta \right|^2 \Big/ \pi R_0^2 \left(1 + \frac{3r^2}{2R_0^2} \right) + f^2 \int_0^{2\pi} \left| \frac{\partial\tilde{\rho}}{\partial\theta} \right|^2 d\theta \right). \tag{2.108}$$

In the large aspect ratio limit $r \ll R_0$, only the $\sin\theta$ i.e. the $m = 1$ mode is present. The frequency of the geodesic mode can then be expressed simply as

$$\omega_{\mathrm{GAM}}^2 = \frac{2c_s^2}{R_0^2}\left(1 + \frac{1}{2q^2}\right) \tag{2.109}$$

with the sound speed $c_s = \sqrt{\gamma p/\rho}$, and the factor of $1/2q^2$ relating to the balancing Pfirsch–Schlüter current maintaining $\nabla \cdot \mathbf{J} = 0$.

GAMs in a rotating plasma

Extending the idealised large aspect circular cross section model of Winsor, a relation can be found incorporating a toroidal rotation velocity. The derivation by Lakhin et al. [2010] starts from a simple velocity profile of

$$\mathbf{v_0} = R^2\Omega(\psi)\nabla\zeta \tag{2.110}$$

where Ω is the rotation frequency. Next the equilibrium mass density is taken as a constant on the flux surfaces $\rho_{m0} = \rho_{m0}(\psi)$ giving a non-uniform pressure with

centrifugal component

$$p_0 = p(\psi) + \frac{1}{2}\rho_{m0}\Omega^2 R^2 \tag{2.111}$$

Then from a linearised single fluid Ohm's Law

$$\mathbf{E} = -\tilde{\mathbf{v}} \times \mathbf{B}_0 = -\nabla\tilde{\phi} \tag{2.112}$$

is leads to a series of equations for the potential and pressure fluctuations in (ψ, θ) in terms of the sound speed and rotation Mach number. Eventually yielding a fourth order polynomial dispersion relation for the electrostatic fluctuations with two solutions

$$\omega^2_{\mathrm{GAM}} = \frac{c_s^2}{2R_0^2}\left(2 + \frac{1}{q^2} + 4M^2 + \sqrt{(2 + \frac{1}{q^2} + 4M^2)^2 + \frac{2M^4}{q^2}}\right) \tag{2.113}$$

$$\omega^2_{\mathrm{ZF}} = \frac{c_s^2}{2R_0^2}\left(2 + \frac{1}{q^2} + 4M^2 - \sqrt{(2 + \frac{1}{q^2} + 4M^2)^2 + \frac{2M^4}{q^2}}\right) \tag{2.114}$$

The zonal flow is always unstable for rotation $M > 0$ with growth rate $\gamma_{\mathrm{ZF}} = |\omega_{\mathrm{ZF}}|$.

An alternative derivation of Elfimov et al. [2011], starts from the more realistic assumption that the equilibrium temperature is constant on flux surface rather than the density, and considers the branches of the GAM and zonal flow with both toroidal and poloidal rotation. The combination of rotations is essential when considering the non-adiabatic thermal flow. In this case three branches are recovered

$$\omega^2_{\mathrm{GAM1}} = \frac{c_s^2}{R_0^2}\left[2 + \frac{1}{q^2} + \left(2 - \frac{1}{q^2} + \frac{2}{q^4}\right)M_p^2 + 4M_t^2 - 4\left(1 - \frac{1}{q^2}\right)M_p M_t\right] \tag{2.115}$$

$$\omega^2_{\mathrm{GAM2}} = \frac{c_s^2}{q^2 R_0^2}\left[1 + \left(3 - \frac{2}{q^2}\right)M_p^2 - 4M_p M_t\right] \tag{2.116}$$

$$\omega^2_{\mathrm{ZF}} = \frac{c_s^2}{q^2 R_0^2}\left[M_p^2(1 - M_d)^2 + \frac{q^2(\gamma - 1)}{2(1 + 2q^2)}(M_t^2 - 2M_t M_p + 2M_p^2)M_t^2\right] \tag{2.117}$$

where γ is the adiabatic index, and M_d is a factor related to the non-adiabatic part of the heat flux. The first GAM branch is similar to Lakhin's result, but the new branch is at a much lower frequency and would be hard to experimentally validate. The variation of $\omega_{\mathrm{GAM}}/(c_s/R_0)$ is plotted in figure 2.8 as a function of toroidal Mach number M_t for both models at a small fixed poloidal rotation of $M_p = 0.1$, and typical safety factor $q = 4$. Both these formulations however are restricted to large aspect, circular cross-section. We will see later in chapter 3 and in more detail in chapter 5, that for spherical tokamaks there is a large deviation from these.

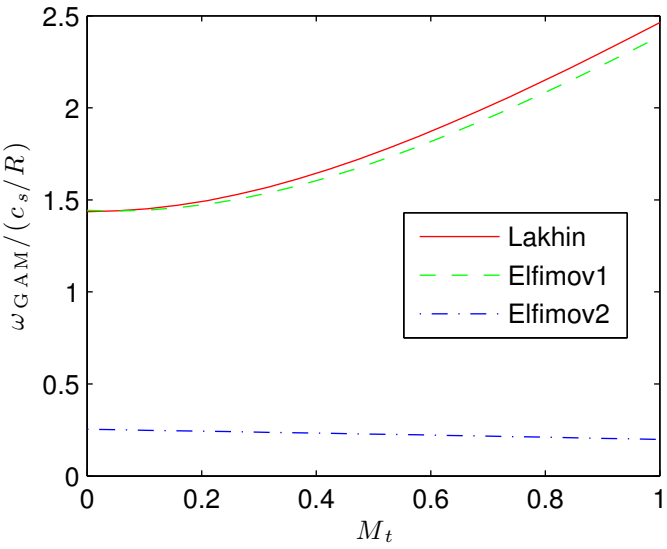

Figure 2.8: GAM frequency variation with toroidal rotation for Eq. (2.113) red line, Eq. (2.115) green dashed line, and Eq. (2.116) blue dot-dash line, all for $M_p = 0.1$, $q = 4$.

2.11 Edge Localized Modes (ELMs)

The identification of high-confinement mode (H-mode) has been one of the greatest advances in tokamak operation in the last few decades, and has been demonstrated empirically on nearly all devices. A possible explanation is that when the additional free energy supplied, for example, by neutral beam injection, exceeds a certain threshold, the turbulence–zonal flow feedback system moves to a more zonal dominated state. Resulting in a three to five times higher energy confinement time than that of the purely ohmically heated L-mode plasmas. The edge transport barrier allows a steepening of the density and temperature gradients forming a narrow pedestal just inside the last closed flux surface. This pedestal becomes unstable to pressure gradient (ballooning) modes which can couple to current (peeling) modes, the onset of which causes filaments of plasma to be ejected and are known as Edge Localized Modes (ELMs). The instability is quasi-periodic as a build-up then partial collapse of the pedestal, with the ejected plasma flowing towards wall and divertor, potentially causing damage due to excessive heating of the plasma facing components.

The total amount of energy available to an ELM grows with size of device, so a large ELM on ITER could cause catastrophic damage and so pose an unacceptable

level of risk in operating in H-mode without some form of mitigation. Studies for example on JET [McDonald et al., 2008], have characterised ELMs into various types across a range of conditions, in order to find an appropriate operating scenario for ITER and any future fusion power devices. In recent years it has been found that large pressure limit (type I) ELMs can be suppressed by the applications of resonant magnetic perturbations (RMPs) [Evans et al., 2006]. Resulting in smaller, but more frequent type II, III or 'grassy' ELMs. This 'ELMy H-mode' operation is proposed as a way of optimising the combination of inter-ELM confinement and ELM losses, whilst reducing the risk of a large ELM.

Chapter 3

Interaction between a low frequency electrostatic mode and resonant magnetic perturbations in MAST

"It is a capital mistake to theorise before one has data. Insensibly one begins to twist facts to suit theories, instead of theories to suit facts."
— Sherlock Holmes in *A Scandal in Bohemia*, Sir Arthur Conan Doyle

3.1 Introduction

RMPs are one of the key methods to control ELMs and this is critical for managing the pedestal behaviour in H-mode and other advanced operating scenarios of any future reactor. However, the impact of magnetic perturbations on the plasma is not well understood. We refer mostly to the indirect impact on the turbulence around rational $q = m/n$ surfaces, via changes of the amplitude and other features of zonal flow and low frequency modes. We will demonstrate that one of the effects that RMPs introduce is apparent suppression of the GAM, which in turn may lead to the increase levels of turbulence and thus increase of heat transport.

In this chapter, we present analysis of a low frequency electrostatic mode, detected at the outboard midplane, and its interaction with the resonant magnetic field perturbations (RMP) which are generated by external coils [Kirk et al., 2010], designed with the aim of controlling edge localised mode (ELM) instabilities on the Mega Amp Spherical Tokamak (MAST) [Lloyd et al., 2003]. The radial magnetic

field perturbations induced by these ELM control coils, resonantly couple to the helical confining field generating localised magnetic islands. This results in complex interactions of the plasma with these RMPs. Analysis reveals the impact of edge rotation, due to the torque induced by resonant magnetic perturbations, on the dispersion relation of the mode. It should be noted here that the torque is usually apparent as a breaking force, reducing the already fast rotation in the core of NBI heated plasmas, rather than the edge spin-up observed in these ohmic plasmas. A correlation is also identified between the amplitude of the mode and the overall turbulence level. Finally, we explore the possibility that observed fluctuations are GAMs and discuss implications of our observations relating to confinement.

3.2 Mega Amp Spherical Tokamak (MAST)

MAST is a very tight aspect ratio, or spherical, tokamak with a major radius $R_0 \approx 0.85$ m and a minor radius of $a \approx 0.65$ m, magnetic field of $B_0 = 0.5$T on axis giving the toroidal component as $B_\mathrm{t} \approx B_0 R_0/R$. The poloidal component of the magnetic field B_p, created by the plasma current of up to $I_p = 1.0MA$, and shaped by the poloidal field coils within the vacuum vessel, yielding a pitch angle to the horizontal reducing to about 22° at the outboard midplane. Note, the figure shows a ELM in a lower q_{95} discharge, and hence steeper angle than the discharges studied.

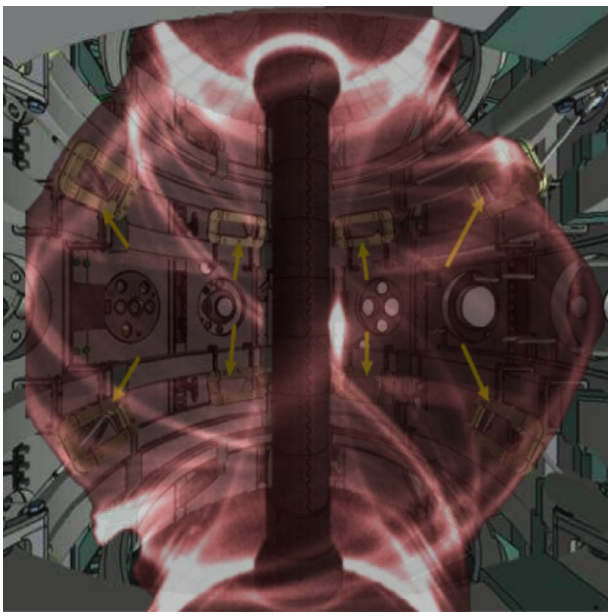

Figure 3.1: Composite of a schematic of MAST showing the ELM control coil positions, and a D_α visible light image of the filamentary structure of an ELM, highlighting the field line shape

3.3 Resonant Magnetic Perturbations

In addition to the shaping and external field error correction coils, designed to smooth the toroidal ripple MAST was fitted with 12 internal (at the time of the experiment) ELM Control Coils (ECC) as shown in figure 3.1, which have since been upgraded to 18 coils with the addition of a extra six coils filling the gaps in the bottom row. Each coil has 4 turns so a current of 1.4kA corresponds to 5.6kAt. These coils introduce small radial perturbations to the magnetic field which forms a complex set of resonant interactions at the rational surfaces $q = m/n$. For demonstration purposes, we now consider a simple model of a cylinder (r, θ, z) with equilibrium helical magnetic field and perpendicular perturbations, here given in terms of the vector potential $\mathbf{A} = A\hat{\mathbf{z}}$

$$\mathbf{B} = B_0 \left(\hat{\mathbf{z}} + \frac{1}{q}\hat{\theta} \right) + \nabla \times A\hat{\mathbf{z}} \tag{3.1}$$

with pertubations of the form [Reiser, 2007]

$$A = -\sum_m (-1)^m A_0 \exp(m(r-a)/a) \cos(m\theta - nz). \tag{3.2}$$

The field lines of the model, expressed as one directional derivatives, can be traced by following z as a pseudo-time variable [Dewhurst, 2010]

$$\frac{\partial \theta}{\partial z} = \frac{1}{qR} - \frac{1}{rB_0}\frac{\partial A}{\partial r} \qquad \text{and} \qquad \frac{\partial r}{\partial z} = \frac{1}{rB_0}\frac{\partial A}{\partial \theta} \tag{3.3}$$

Increasing the strength of the applied perturbation causes island chains to form at the rational surfaces, as shown in the Poincaré plots of figure 3.2. A measure of the RMP reaction is the Chirikov parameter [Chirikov, 1960], defined as the ratio of the half island width to the rational surface separation, where at $\sigma_{ch} > 1$ there is significant ergodisation of the field, and the notion of distinct nested flux surfaces breaks down. This simplistic vacuum model does not take into account the

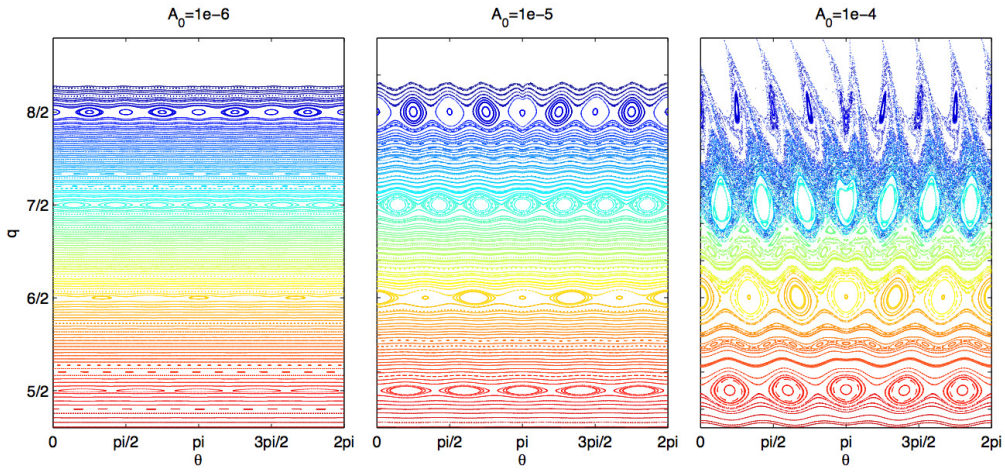

Figure 3.2: Poincaré plot of magnetic field lines for three perturbation levels

plasma response to the perturbation. The plasma responds to the perturbations by inducing rotation which tends to shield the penetration of the perturbations from the core. More sophisticated modelling of the plasma response using the MARS-F code [Liu et al., 2011], showed this rotation can reduce the amplitude of the resonant harmonics by an order of magnitude where the resistivity is high, so that simple vacuum modelling tends to overestimate the degree of ergodisation. The parity and phase of the top and bottom row of coils affects the nature of the plasma reaction. Figure 3.3 shows the modelled response for MAST under similar conditions to the discharges studied below which had $q_{95} \approx 6$ and even parity. The figures are plotted in terms of the normalised radial component of the magnetic field $b^1 \equiv (\mathbf{B}\cdot\nabla\psi_{\text{pol}}^{1/2})/(\mathbf{B}\cdot\nabla\phi)$. The magnitude of which then around 0.02% of the equilibrium magnetic field.

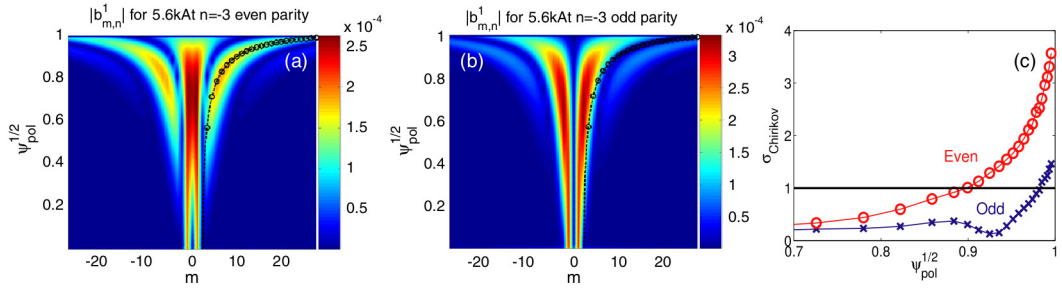

Figure 3.3: Poloidal magnetic spectra for the (a) even and (b) odd parity configurations for a scenario 1 discharge. Superimposed as circles and dashed line are the q = m/3 rational surfaces of the discharge equilibrium. (c) Predicted profiles of the Chirikov parameter produced with 5.6 kAt in the internal ELM coils in even (open circles) and odd (crosses) parity configurations (from [Kirk et al., 2010]).

3.4 Experimental Setup

We analyse data from several ohmic L-mode plasma discharges (numbered 21856 to 21860), since direct measurement via probes is not possible inside H-mode plasmas. The discharges were similar in terms of plasma parameters, but differed in terms of radial magnetic perturbation. These plasmas had a line average number density, $\bar{n}_e \approx 1.5 \times 10^{19}$ m^{-3}, magnetic field on axis $B_0 = 0.5$T and plasma current $I_p = 0.4$MA.

3.4.1 Langmuir Probes

A Langmuir probe is an electrode inserted into a plasma that can be biased either to higher or lower potential than the plasma in order to affect the sheath around it, and so the nett measured current [Wesson, 2004, p546]

$$I = (J_i + J_e)A = J_i(1 - exp(e(V - V_f)/T_e))A \tag{3.4}$$

where A is the effective projected surface area of the probe, V is the applied voltage, and V_f is the potential the electrode would float at if isolated.

From this several parameters can be determined. Firstly if the bias is to a sufficiently negative value that effectively all the electrons are repelled, the ions approaching the probe will satisfy the Bohm sheath criterion which states that ions approaching the sheath will be accelerated in a pre-sheath region until they reach the ion sound speed. The resulting ion saturation current then gives a measure of

the electron density

$$I_{\text{sat}} = en_e\sqrt{\frac{T_e}{m_i}}A \tag{3.5}$$

Alternatively the probe can be biased such that the nett current is zero to yield the floating potential. The plasma potential can then be inferred from

$$V_p = V_f + \Lambda \tag{3.6}$$

where the potental drop over the sheath $\Lambda = -0.5(T_e/e)\ln[2\pi(m_e/m_i)(1+(T_i/T_e))]$. The logarithm is slowly varying with T_i/T_e. As with other studies (see [Moyer et al., 1995], for example) we neglect temperature effects and use floating potential as a proxy for plasma potential.

3.4.2 Reciprocating Probe

The data were collected using a Gunderstrup type reciprocating probe on the outboard mid-plane of MAST [MacLatchy et al., 1992; Tamain et al., 2010]. The 5cm diameter probe head is comprised of 11 Langmuir probes, eight of which, with diameter 2.85mm are biased −200V to measure ion saturation current flush with the cylinder edge 3.5mm back from the end. The remaining three pins protrude 1.5mm from the face to measure floating potential, V_f, as illustrated in figure 3.4.

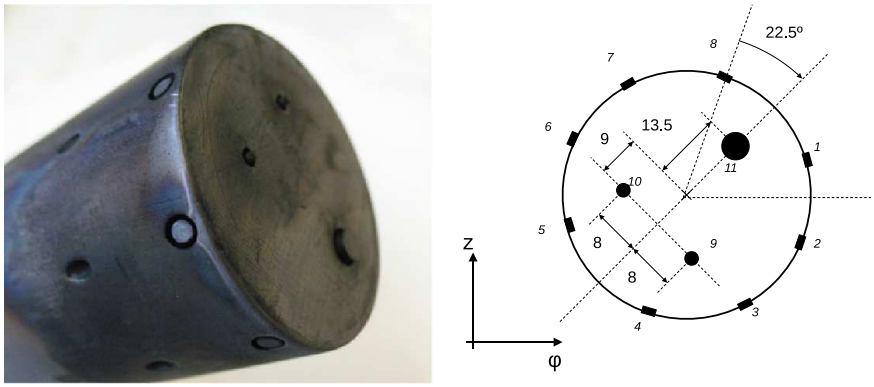

Figure 3.4: (a) Gunderstrup probe head (b) schematic of pin layout.

3.4.3 Raw data

The I_{sat} and V_f measurments have a sample rate of 500kHz, giving a Nyquist limit of 250kHz. Figure 3.5 shows the evolution of ion saturation current (and so density),for two selected pins on opposite sides of the probe as the probe enters the plasma at $\sim 0.25s$, then pulls out at $\sim 0.45s$, before the end of the discharge.

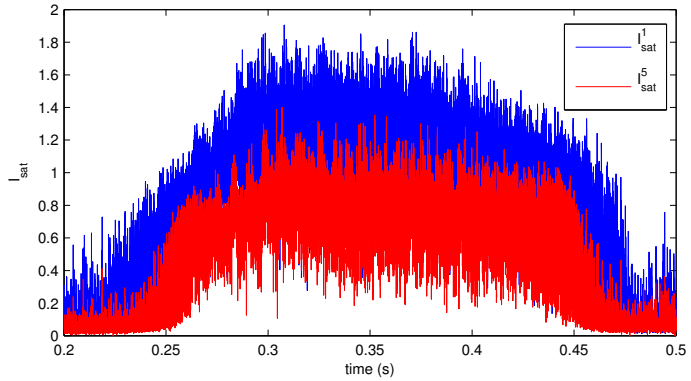

Figure 3.5: Ion Saturation current signal for two selected pins of discharge 21856

Some electronic noise is present on the V_f probe signals at 142kHz and several higher frequencies, as shown by the power spectrum over the semi–stationary interval t=0.30-0.32s, in figure 3.6. So we concentrate on the fluctuations below 100kHz. Looking at these power spectra, apart from the expected turbulent spectrum charac-

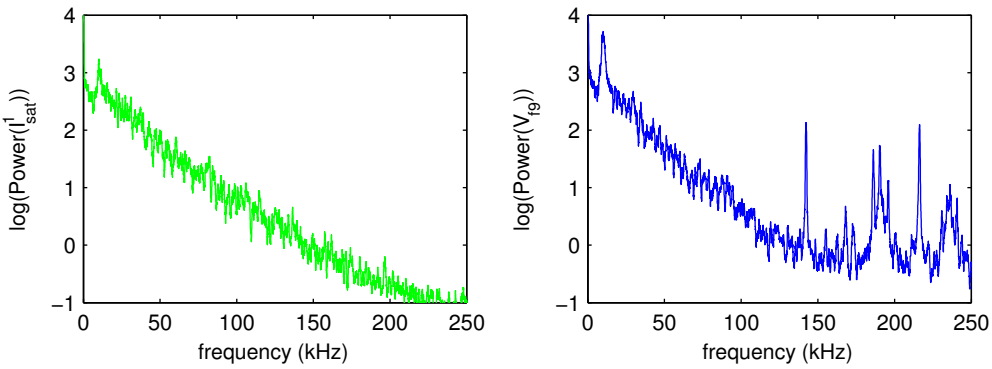

Figure 3.6: Power spectra of $I^1_{\rm sat}$ and V_{f9} from discharge 21856 for t=0.30-0.32s

terised by the fall–off of power at higher frequencies a feature was noticed at around 10kHz.

3.4.4 Discharge Overview

Figure 3.7 shows some of key parameters during the discharges studied. Panel (a) shows the position of the probe with respect to the last closed flux surface (LCFS) as a function of time. The sets of vertical dashed lines indicate three time intervals, marked as I, II and III in the figure, which we will repeatedly refer to in our study. Interval I corresponds to times $t = 0.28 - 0.31$ s when the probe is at a position $r_p = -3.5$cm inside the LCFS, but before the coils are turned on. Interval II

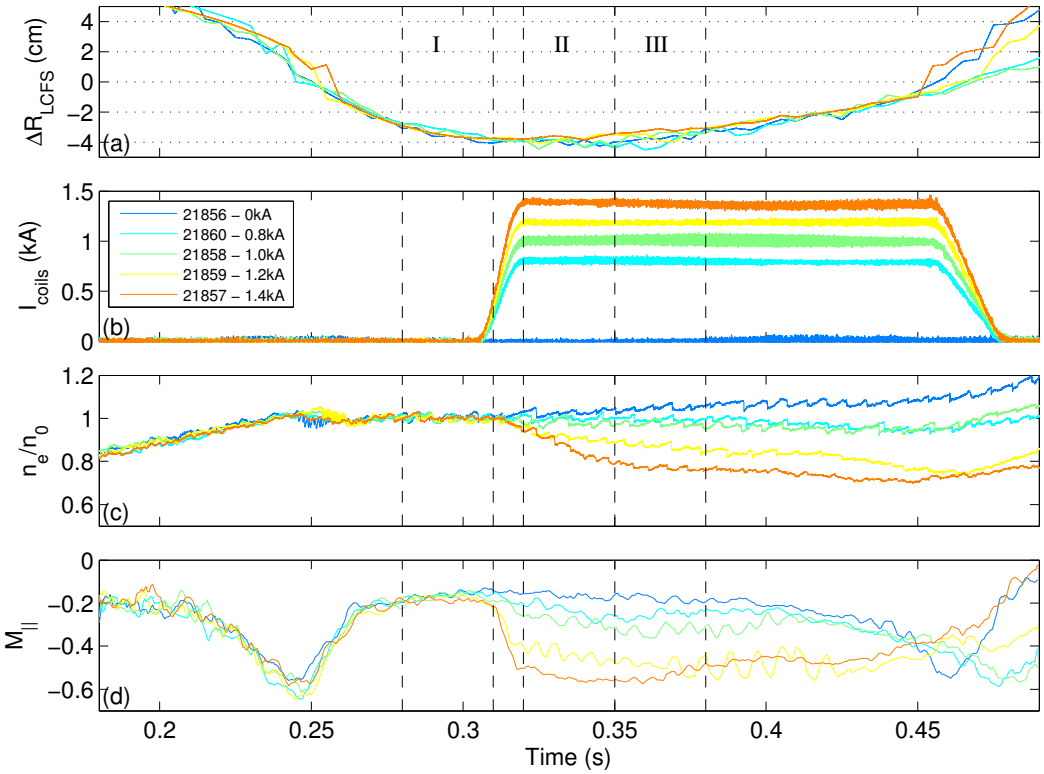

Figure 3.7: (a) Langmuir probe position with respect to the last closed flux surface (indicated as 0). (b) ELM coil current (c) line average plasma density normalised to level at t=0.3s (d) Parallel flow Mach number at probe position.

corresponds to times $t = 0.32 - 0.35$ s and position $r_p = -4$cm, just as the coil current reaches its assigned value, and interval III is the following 30 ms whilst the probe is held at $r_p = -4$cm, ie. $t = 0.35 - 0.38$ s. The line averaged plasma density, normalised to the level before the coils turn on to remove the slight shot-to-shot variability due to gas flow rates for each discharge, is shown in Figure 3.7(c). Induced RMPs result in a well documented gradual density pump-out [Kirk et al., 2010] which occurs $t \approx 0.32 - 0.36$s. A rapid increase in plasma rotation, on the timescale of the ELM coil current turning on, is also observed as the magnetic field is perturbed, as seen previously in[Tamain et al., 2010]. This is shown in Figure 3.7(d), where the flow velocity has been calculated using ratios of the fluctuation-averaged $I_{\rm sat}$ signals according to the Van Goubergen model [MacLatchy et al., 1992] (see section 3.5). Thomson scattering temperature and density profiles taken at 0.35s, shown in figure 3.8 show all the shots have similar profiles, falling to $T_e \approx 50$eV at the edge, with a gradient of around 10eV/cm. The core density can be seen to drop, inline with the pumpout illustrated in figure 3.7(c), but the edge density remains

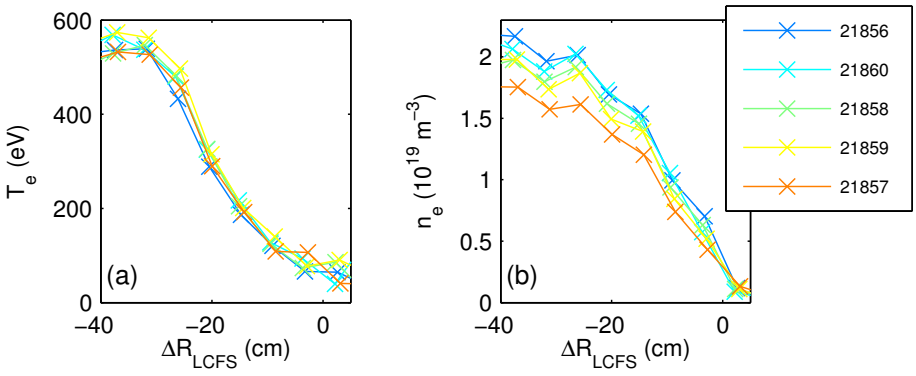

Figure 3.8: Thomson scattering profiles of (a) electron temperature and (b) density, taken at t=0.35s, relative to the LCFS.

roughly constant.

3.5 Rotation Velocities

The probe head is designed for the measurement of plasma flow velocities. The flow Mach number, past the probe parallel and perpendicular to the magnetic field is found via the relative amplitude of the fluctuation averaged I_{sat} signal on opposing pairs of pins (see figure 3.5). This is due to the distortion of the sheath by the flow, resulting in the shealth density, averaged to remove small scale flucuations, being lower on the downstream side of the probe.

$$\frac{1}{c}\ln\left(\frac{\langle I_{\text{sat}}^{i+4}\rangle}{\langle I_{\text{sat}}^{i}\rangle}\right) = M_{\parallel} - \frac{M_{\perp}}{\tan\alpha_i} \tag{3.7}$$

where the superscript i in the saturation currents is the pin number, and α_i is the angle between the tangent to the pin surface and the magnetic field. c is a parameter weakly dependent on $M_{\parallel}$, taken as a constant $c = 2.3$ as in [Tamain et al., 2010]. Using three pairs of I_{sat} pins, ignoring the pair where α_i is small, gives 3 equations for the 3 unknowns of $M_{\parallel}$, $M_{\perp}$, and α_i. The fitting algorithm first calculates the left hand side of equation (3.7) for $i = 1, 2, 3$ using the ion saturation currents averaged over 500 points or 1ms, which was found to give a reasonable compromise between a consistent solution and temporal resolution. Next, each pair of equations is subtracted to give expressions for $M_{\perp}/\tan(\alpha_i)$, then utilising the geometric arrangement of the probe $\alpha_1 = \alpha_2 + 45° = \alpha_3 + 90°$, the orientation of the probe to the magnetic field is determined. The angles are substituted back into the three expressions for $M_{\perp}$ and the result taken as the average. This is then substituted back into the the original three equations to similarly obtain $M_{\parallel}$.

Using the difference in the probe radial position and the plasma last closed flux surface obtained from the EFIT reconstruction the edge plasma flow profile can be plotted as the probe is inserted, the ELM coils turned on, then probe withdrawn, as shown in figure 3.9. Despite the relatively large apparent fluctuations in radius due to the combination of the whole plasma position itself varying and uncertainty in the EFIT reconstruction. The figure clearly shows the small intrinsic rotation prior to the ELM control coils being turned on followed by a rapid increase in flow dependent on the level of the coil current and so magnitude of the induced magnetic perturbations. Once the coils are activated the probe gradually pulls out from $t = 0.33s$ to $t = 0.45s$ in which for the 1.2kA and 1.4kA cases the flow remains roughly constant with radius. Note, this increase in flow in these ohmic discharges is in contrast to the breaking typically observed in NBI-heated H-mode plasmas [Kirk et al., 2011].

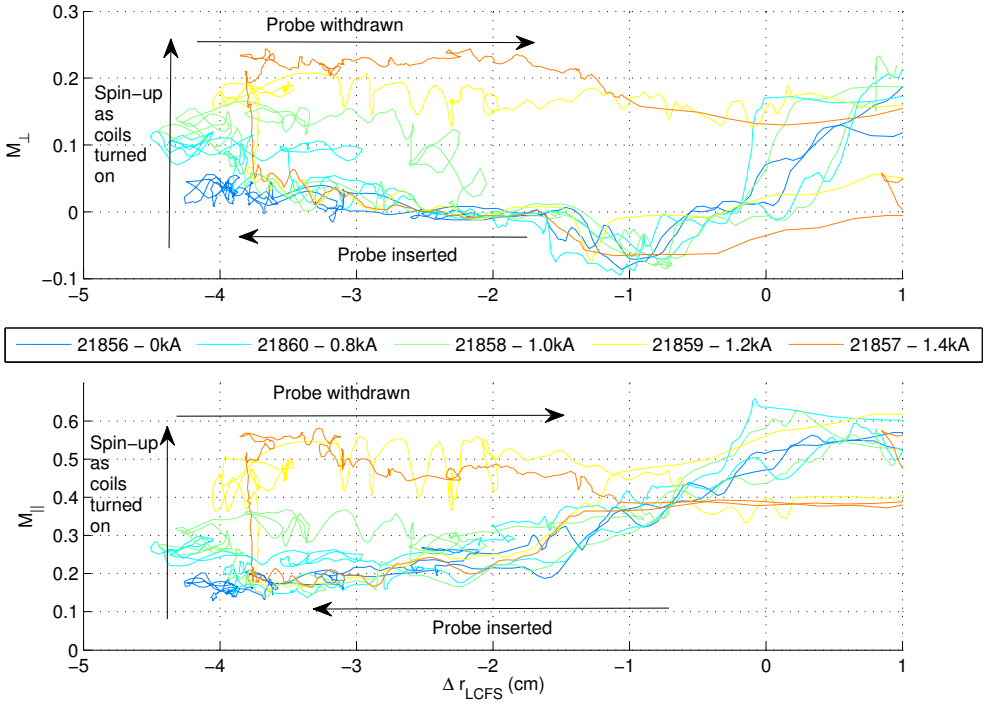

Figure 3.9: Change in perpendicular and parallel plasma flow versus radius, relative to the LCFS, as probe is inserted and removed

Rotation vs ELM control coil current

Taking the time period immediately after the ELM control coils have reached their set current for each discharge, the modified equilibrium flow can be seen to increase linearly with current from $0.8kA$ to $1.4kA$ in both parallel and perpendicular directions, as illustrated in figure 3.10. The error bars correspond to one standard deviation around the mean flow over interval II. The equation for each fitted line is $M_\perp = 0.23I_{\mathrm{ECC}} - 0.09$ and $M_\parallel = 0.56I_{\mathrm{ECC}} - 0.22$

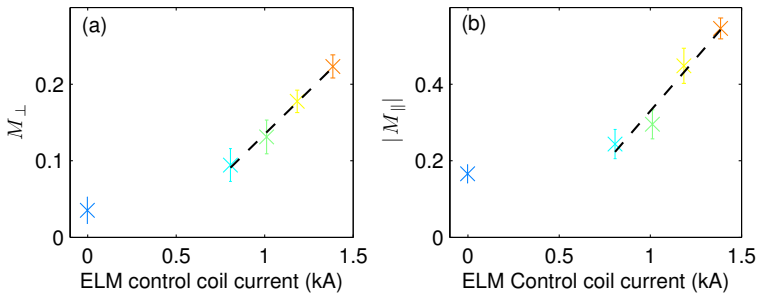

Figure 3.10: Change in parallel and perpendicular plasma flow with applied RMP level (colour scheme as in figure 3.9)

3.6 Results

Figure 3.11(a) shows a typical spectrogram of floating potential measurement, when the ELM coils are not activated. A high power feature with frequency of about 10kHz is clearly visible for a radial location $\Delta R_{\mathrm{LCFS}} < -2$cm for all discharges examined. The spatial distribution of power is not uniform, but rather shows an intermittent characteristic as reported in other similar observations [Conway and the ASDEX Upgrade Team, 2008]. Figure 3.11(b), shows magnetic field spectra from the Mirnov coils, located on the probe head 2cm behind the I_{sat} pins, for the same discharge. It is clear that there is no evidence of tearing mode perturbations with comparable frequency leading to conclusion that the observed mode is electrostatic in nature. Indeed, tearing modes are not normally seen in MAST for cool ohmic discharges of this type, however, similar frequencies have been reported for H-mode discharges [Dudson et al., 2005].

In order to quantify the coupling between observed mode and the drift wave turbulence, we measure the coherent energy exchanged between different Fourier modes via a resonant three-wave interaction [Tynan et al., 2001]. This is achieved by calculating the bispectrum, defined as $B_{f_3}(f_1, f_2) = \langle \phi(f_1)\phi(f_2)\phi^*(f_3) \rangle$, for the resonant modes which fulfil the frequency relation $f_3 = f_1 + f_2$. The auto–bispectrum is calculated using the Matlab routine `bisp3cum` [McMurray, 2000], which uses the efficient convolution method via Fourier transform of the third order (unbiased) cumulant of the timeseries of N samples, defined for each lag τ_1, τ_2.

$$\kappa_3(\tau_1, \tau_2) = \frac{1}{N} \sum_t \phi(t)^* \phi(t + \tau_1)\phi(t + \tau_2) \tag{3.8}$$

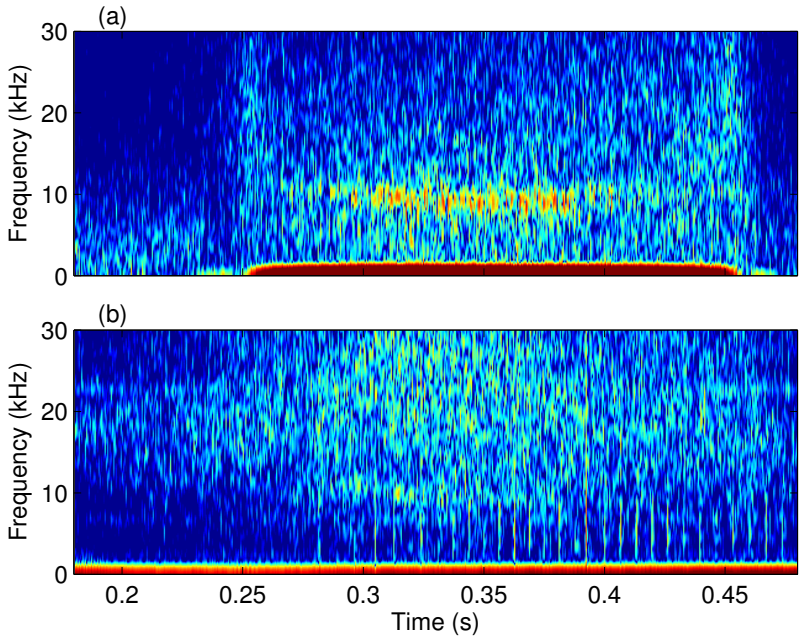

Figure 3.11: Spectrogram for low frequency part of the spectrum from shot 21856 for (a) potential, showing intermittent high power signature at ≈ 10 kHz frequency, for the period the probe is more than ≈ 2 cm inside the LCFS. (b) Mirnov coil response, showing no corresponding magnetic fluctuation

The bispectra is then

$$B_{f_3}(f_1, f_2) = \mathcal{F}(\kappa_3(\tau_1, \tau_2) * w(\tau_1, \tau_2)) \tag{3.9}$$

where $\mathcal{F}$ is a 2D Fast Fourier Transform and w is a standard 2D windowing function, here defaulting to the Priestley window [Oroian et al., 2008]. Figure 3.12 shows these bispectra for the case without (a) and with (b,c) RMPs. We see that when the ≈ 10 kHz mode is present, strong non-linear and non-local (in k-space) interactions with other low frequency modes dominate the bispectrum. These are represented by off-diagonal features on this plot. When the peak is absent these features disappear and purely local cascade-like energy transfer, that now extends to much higher frequencies, is dominant. This coincides with the increased power level in the high frequency part of the spectrum, confirming a parasitic relation between the mode, as an energy sink, and turbulence.

We now examine the interaction between resonant magnetic perturbations and this electrostatic mode identified above. Figure 3.13(a) shows the floating potential power spectrum calculated during the Interval I, before the ELM coil current

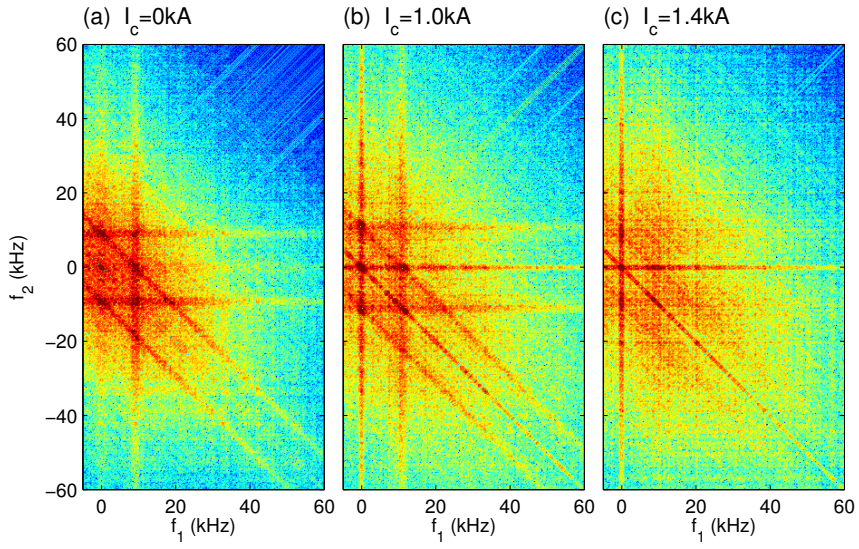

Figure 3.12: Bispectra of potential fluctuations, for discharges (a) 21856 $I_c = 0kA$ (b) 21858 $I_c = 1.0kA$, and (c) 21857 $I_c = 1.4kA$ all for interval III

is switched on. A peak at $\approx$ 10kHz is clearly visible in this plot and the profile of the spectra, including the peak is nearly identical for all discharges considered. These spectra do not saturate at lower frequencies, but show a rising trend which strongly suggests presence of a zero-frequency zonal flow. At high frequencies spectra exhibit a typical turbulent power-law behaviour. Figure 3.13(b) shows the spectra for interval II. When the ELM coils are turned on the mode peak is affected in two different ways: (i) the position of the peak is shifted towards higher frequencies with increased coil current and (ii) the amplitude of the peak decreases with time.

The normalised cross correlation between two floating potential pins located 2.5cm apart approximately parallel to the field, is used to give a measure of the spatial coherence of the mode, defined as

$$C_{xy}(\tau) = \frac{1}{N} \sum \frac{(V_{f9}(t) - \bar{V}_{f9})(V_{f11}(t+\tau) - \bar{V}_{f11})}{\sigma_{V_{f9}} \sigma_{V_{f11}}} \tag{3.10}$$

This is shown in figure 3.13(e-f). The strong correlation $\tau = 0$ peak has no nett lag between the two pins showing they are in phase, i.e. is not due to structures being advected past the probe. This, together with the clear oscillations upto two wave periods away, suggests the wavelength of the mode is much longer than the separation between the pins. In addition, this alternative representation illustrates

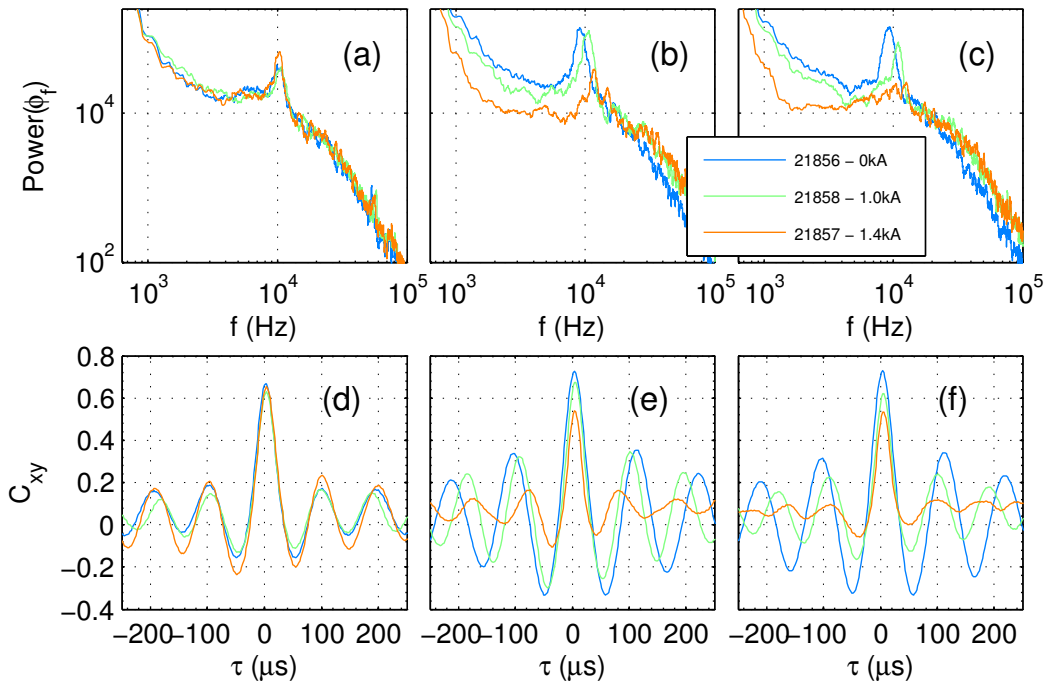

Figure 3.13: Power spectral densities for potential fluctuations: (a) interval I: coils off (b) interval II: coils on, peaks shifted (c) interval III: coils on, 30 ms later, peak damped for coil current 1.4 kA. (e)-(f) corresponding cross correlation between floating potential pins (V_{f9} and V_{f11})

again the frequency shift and damping of the mode for the 1.4kA case. The small separation of the probe pins is not conclusive and for true spatial analysis additional diagnostics at other locations on the device would be needed.

While frequency shift shows an increasing trend with the increased coil current (plasma rotation), the decrease in peak amplitude with time exhibits a threshold-like behaviour. Indeed, figure 3.13(c) shows that the most dramatic change occurs when the coil current achieves the value of 1.4 kA. At this point observed coherent mode is rapidly damped and disappears entirely within 30ms. Such threshold-like response of this mode to the magnetic perturbations is consistent with other observations on MAST for example [Kirk et al., 2010; Tamain et al., 2010] and other machines.

3.7 Discussion

A correct identification of the mode detected above is critical to understanding the nature of its interaction with RMPs and the drift turbulence. Such identification

is unambiguous if, and only if, the temporal and spatial measurements on a scale of interest are available. Spatial data, which allows a measurement of low mode numbers, is in our case not available and we must rely on the temporal variability of the signal alone. In what follows, we explore three different modes and assess the likelihood that the observed 10kHz peak is due to one of them.

First, we examine predicted frequency for GAM, ion acoustic mode (IAM) and the coherent drift wave, based on the measured plasma parameters. GAMs have been observed in many plasmas and across different confinement regimes, underlying the universal aspect of this large scale mode [Conway et al., 2008; Gupta et al., 2006]. In the large aspect ratio, circular limit has a frequency of $\omega_{\mathrm{GAM}} \approx \sqrt{2}c_s/R_0$. Frequency predicted for IAM would have an explicit dependence on q^{-1} (see 2.10 Eq. 2.108), and would in our case give frequency lower than ω_{GAM} by a factor of 6. Similarly, we can estimate the frequency of the most unstable drift wave, given by an empirical relation $k_\perp \rho_s \approx 0.3$. For edge parameters of density gradient scale length $L_n = n/|\nabla n| \approx 0.08$m and $T_e \approx 80$eV obtained from the Thomson scattering data, we use equation (2.77) to give the frequency as

$$f_{dw} = \frac{\omega^*_{ne}}{2\pi} = \frac{0.3}{2\pi\rho_i}\frac{T_e}{eB}\frac{1}{L_n}. \tag{3.11}$$

The magnetic field dependence cancels using the hybrid Larmor radius $\rho_s = \sqrt{T_e/m_i}/(eB)$ leaving

$$f_{dw} = \frac{0.3}{2\pi}\frac{T_e^{3/2}m_i^{1/2}}{L_n} \approx 30 - 40\mathrm{kHz}. \tag{3.12}$$

i.e. higher than the observed mode frequency. In addition, the presence of fully developed power-law spectrum and the absence of higher harmonics does not support the idea of a coherent drift wave. Indeed, if we expand figure 3.13(c) to investigate in more detail the higher frequency turbulent spectrum, shown in figure 3.14. A subtle knee is visible in the spectrum corresponding to the drift wave injection frequency of $\approx$ 35kHz separated from the large peak at $\approx$ 10kHz. Linear fits are applied to sections of the frequency spectra above and below this point between $15 - 35$kHz, and $35 - 100$kHz. We see that while both follow an approximate f^{-3} power law over the inertial range to the high frequency dissipation scale, characteristic of the quasi-2D nature of drift wave turbulence, as found in Hasegawa-Wakatani simulations [Camargo et al., 1995]. The inverse cascade to lower frequencies is modified from a f^{-2} relationship with the GAM, to a f^{-1} power law with the mode suppressed on application of the RMPs. With the effect of raising the whole turbulent spectrum, increasing the proportion of energy carried by the high frequency fluctua-

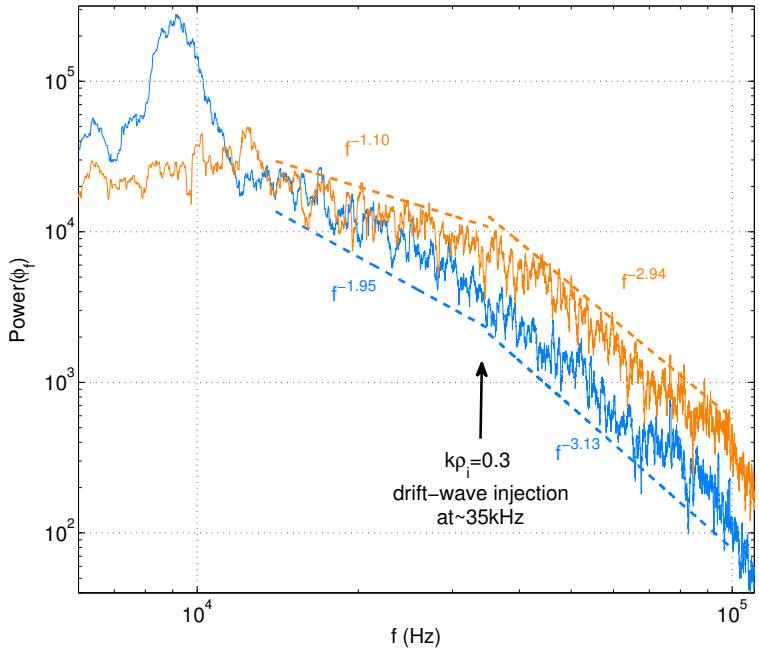

Figure 3.14: Spectra of potential fluctuations over interval III, without (blue) and with (orange) RMPs

tions. The f^{-1} (or equivalently k^{-1}) scaling is indicative that the non-local coupling of the fluctuations within this range is to the background mean flow [Tchen, 1953], rather than being terminated at the intermediate frequency mode. Although caution should be taken at inferring too much from a power law fit over such as short frequency interval. The increased power at high frequencies could then lead to an increase in flux, and reduction in energy confinement time.

3.7.1 Mode frequency with rotation

Since temporal behaviour suggests that the observed mode may be a GAM, we further explore the dependence of GAMs dispersion relation on plasma rotation. We recall that presented data shows a shift of the peak to higher frequencies on the application of RMPs. Previously, similar behaviour has been noted in four-field model simulations [Reiser, 2007]. We test if this shift can be explained by the increased toroidal rotation of the plasma as shown in the Figure 3.7(d). A theoretical GAM dispersion relation for large aspect ratio and adiabatic electrons can be written in terms of the toroidal rotation Mach number M and safety factor,

q [Lakhin et al., 2010]:

$$\omega^2_{\mathrm{GAM}} = \frac{\omega_s^2}{2}\left(2 + \frac{1}{q^2} + 4M^2 + \sqrt{(2 + \frac{1}{q^2} + 4M^2)^2 + \frac{2M^4}{q^2}}\right) \tag{3.13}$$

where $\omega_s = c_s/R_0$, sound speed $c_s = \sqrt{T_e/m_i}$, R_0 is the major radius. Taking $T_e \approx 80$eV, as suggested by the TS data shown in figure 3.8, $q = 6$ from equilibrium reconstruction for our discharges and the major radius, $R_0 = 0.88$ m we obtain a GAM frequency $f_{\mathrm{GAM}} = \omega_{\mathrm{GAM}}/2\pi = 16.5$kHz. We see that the expression (3.13) overestimates the observed frequency. Studies such as [Conway et al., 2008] have suggested various scale factors to account for the elongation and finite aspect ratio, which will be significant in a spherical tokamak such as MAST. Using the derivation of [Gao, 2010] (see section 5.2), but neglecting the small corrections due to Shafranov shift the scale factor $G = \omega_{\mathrm{GAM}}/\omega_{\mathrm{GAM}}(\kappa = 1, \epsilon = 0)$ can be expressed as

$$G = \sqrt{\frac{7}{4}\left(\frac{2}{\kappa^2 + 1}\right)}\left(1 - s_\kappa \frac{\kappa^2}{4\kappa^2 + 4} - \epsilon^2 \frac{9\kappa^2 + 3}{8\kappa^2 + 8}\right) \tag{3.14}$$

where ϵ is the inverse aspect ratio, κ is the elongation, and its radial derivative $s_\kappa \approx (\kappa - 1)/\kappa$. Using values appropriate for these shots of $\kappa = 1.55$, $\epsilon = 0.63$ gives a shaping factor of $G \approx 0.6$. Bringing the predicted GAM frequency in line with observed one, $f_{\mathrm{GAM}} = 9.9$kHz.

Combining the shaping factor with the rotational dependence, we correlate the frequency shift with the prediction of (3.13) and find good qualitative agreement with the theory, as shown in the figure 3.15. The errorbars correspond to the peak half-maximum width of ± 600 Hz and one standard deviation on the mean flow for each shot over interval II.

We now focus on the suppression of the observed mode, which appears to have a dependence on the strength of the applied RMPs. We believe that this rapid damping of the mode can be explained by its resonant interaction with the imposed RMPs. When considered in the rotating plasma frame, coherent mode will experience the static $n = 3$ magnetic perturbations imposed by the ELM coils as an Alfvénic oscillation with frequency

$$\omega_{\mathrm{RMP}} = \frac{nMc_s}{R_0}. \tag{3.15}$$

Comparing this relation with equation (3.13), and taking $1/q^2 \ll 1$, a resonance

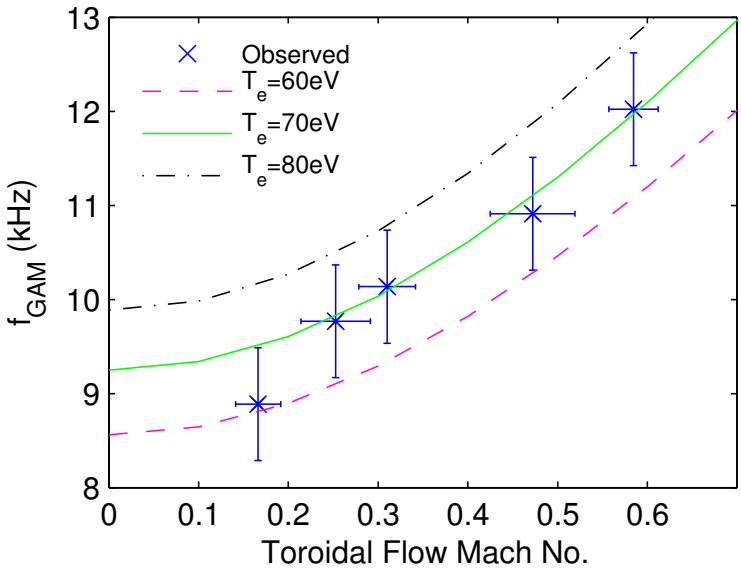

Figure 3.15: Observed peak frequency against toroidal spin-up at $R = 1.42$ m, $q = 6$; together with isotherms for $T_e = 60$eV, 70eV and 80eV

condition is found

$$\omega_{\mathrm{RMP}} = \omega_{\mathrm{GAM}}$$
$$\Rightarrow \frac{nMc_s}{R_0} \approx G\frac{\sqrt{2}c_s}{R_0}(1 + 4M^2). \tag{3.16}$$

For $n = 3$, this can occur as the toroidal rotation approaches $M = 0.6$ corresponding to a frequency of approximately 12 kHz. Thus a resonant transfer of energy from the mode to the RMPs is possible, suppressing the build up of energy in the acoustic mode. We note however that we found no evidence of such coupling in the magnetics signals from the Mirnov coils. For the cases with slightly lower RMP level the decay appears to be more gradual in its temporal evolution. Examination of spectral peak decay times as a function of coil currents was attempted, but the probe was already pulling out of the plasma by the time the peak decreased significantly, thus no accurate estimate of damping time could be ascertained in these discharges.

3.8 Conclusions

In summary, this is the first observation of MHD potential fluctuations on MAST that are consistent with the GAM. Resonant magnetic perturbations appear to shift upwards the frequency of the mode and we believe that this is associated with the

spin-up of the plasma edge. The mode is suppressed entirely when the magnetic perturbations exceed a certain level. This can be interpreted as evidence that GAMs can indeed couple to the Alfvénic perturbations. An alternative interpretation is that the mode suppression can be explained in terms of the connection length, whereby the ergodisation of the edge plasma due the the RMPs effectively shortens the field line connection length between the top and bottom of the tokamak, allowing the parallel ion flow along the field lines to restore the imbalance of the $\mathbf{E}_r \times \mathbf{B}$ poloidal flow, so avoiding the build up of density at either the top or bottom.

The overall effect of coupling between the GAM and RMPs would be detrimental to plasma confinement, since the dissipation of GAM increases the level of turbulent transport. This is an important aspect of GAM dynamics that needs to be explored further.

Chapter 4

Two-fluid simulations of MAST

"The purpose of computing is insight not numbers."

— Cecil Hastings, *1955*

4.1 CENTORI

Following the observations of the GAM-like mode in MAST descibed in chapter 3, and published in [Robinson et al., 2012], simulations were needed to verify the mode structure. Whilst a simple two-fluid code was developed as an exercise, mentioned in chapter 2, in order do perform simulations matching the experimental conditions of MAST a more established code was needed. Given the low frequency and global nature of the geodesic acoustic mode, the requirement for was for a code that could scale sufficiently to run simulations of several milliseconds with sufficient resolution to recover the interaction of drift-wave turbulence at the the scale of $k_\perp \rho_i \approx 0.3$, with global electrostatic oscillations.

`CENTORI` is a global two-fluid electromagnetic turbulence code developed at CCFE by Knight et al. [2012] for modelling in 3D arbitrary aspect ratio and high beta tokamak plasmas. Based on the two-fluid treatment of Hazeltine and Meiss [1985], and in part on the earlier code CUTIE [Thyagaraja, 2000; Thyagaraja et al., 2004, 2005].

The code uses various neoclassical modifications to the two-fluid equations described in chapter 2 in order to recover the additional dynamics under tokamak relevant conditions in the toroidal geometry. Additionally the sub-grid scale dissipation is handled by a phenomenological turbulent diffusivity to damp out the build up of fluctuations at the smallest scales. The sub-grid diffusivity is similar to eddy viscosity or hyper-viscosity used extensively in hydrodynamic 'Large Eddy Simula-

tions', and been shown (in slightly different forms) by Smith [1997] to give better convergence at low resolutions for drift-wave plasma turbulence than a simple $D\nabla^2$ numerical diffusion term.

4.1.1 Grad-Shafranov Equilibrium

The Grad-Shafranov equation describes the equilibrium force balance between the B-field curvature effects and magnetic & plasma pressures, in a cylindrical (R, Z, ζ) coordinate system. Starting from the relationship between the magnetic field and poloidal magnetic flux, ψ

$$\mathbf{B_{eq}} = (\nabla\zeta \times \nabla\psi) + F\,\nabla\zeta$$

the first term can then be given by

$$\nabla\zeta \times \nabla\psi = \nabla\zeta \times \left(\frac{\partial\psi}{\partial R}\nabla R + \frac{\partial\psi}{\partial Z}\nabla Z\right)$$

where of the contravariant basis vectors ∇R and ∇Z are unit vectors, but $|\nabla\zeta| = 1/R$. Skipping the detailed maths, described in [Wesson, 2004] and many other sources, the current density and force balance are combined to yield an equation at each point in (R, Z) for ψ in terms of F and p where the prime denotes $\partial/\partial\psi$

$$\left(R\frac{\partial}{\partial R}\left(\frac{1}{R}\frac{\partial\psi}{\partial R}\right) + \frac{\partial^2\psi}{\partial Z^2}\right) = -4\pi R^2 p' - FF' \tag{4.1}$$

where the left had side corresponds to the toroidal current density.

This is solved numerically on a rectangular grid of (257×256), with an odd number in Z ensuring a grid point on the midplane. Starting from an initial estimate, and using as an input the position and currents in the external poloidal field coils, the solver iterates forward a pseudo time variable until an equilibrium is found.

4.1.2 Geometry

From the cylindrical (R, Z, ζ) coordinate system of the co-evolving equilibrium solver, the simulation space is defined on a dimensionless (ρ, θ, ζ) grid, using two-dimensional Chebyshev polynomials in order to ensure a smooth transformation. The radial coordinate $0 \leq \rho \leq 1$ is defined as $\rho \equiv 1 + \psi/\psi_0$, and produces grid points which are equally spaced in ψ giving a good radial resolution near the edge.

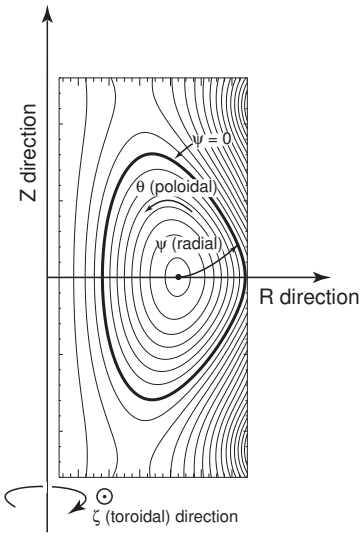

Figure 4.1: A typical plot of ψ contours over the (R, Z) grid, showing diagrammatically the laboratory coordinates (R, Z, ζ) and the plasma coordinates (ψ, θ, ζ) used within `CENTORI`. This plot was calculated by the `GRASS` equilibrium solver (from [Knight et al., 2012])

The coordinate system Jacobian $\mathcal{J}$

The three directions defined by $(\nabla\rho, \nabla\theta, \nabla\zeta)$ make up a "quasi-orthogonal" coordinate system in which $\nabla\rho.\nabla\zeta = \nabla\theta.\nabla\zeta = 0$, but $\nabla\rho.\nabla\theta \neq 0$. The Jacobian of this system is defined as:

$$\mathcal{J} \equiv |\mathbf{e_i} \cdot (\mathbf{e_j} \times \mathbf{e_k})| = |\mathbf{e^i} \cdot (\mathbf{e^j} \times \mathbf{e^k})|^{-1} = \frac{\partial(\rho, \theta, \zeta)}{\partial(X, Y, Z)} \tag{4.2}$$

$$= \nabla\zeta.(\nabla\rho \times \nabla\theta) = \nabla\rho.(\nabla\theta \times \nabla\zeta) = \nabla\theta.(\nabla\zeta \times \nabla\rho) \tag{4.3}$$

and has dimensions $[1/L^3]$. The Jacobian is then chosen to be a flux function i.e. $\mathcal{J} = \mathcal{J}(\rho)$, and is found via integrating the line element l around the contour of constant ρ, where l is defined via

$$\mathbf{B_{eq}}.\nabla\theta = B_p \frac{\partial\theta}{\partial l} = \psi_0 \frac{|\nabla\rho|}{R} \frac{\partial\theta}{\partial l} = \psi_0 \mathcal{J} \tag{4.4}$$

4.2 Normalised equations

In the following section the key equations as evaluated by `CENTORI` are summarised, as detailed in the excellent documentation included with the code [Knight, 2011]. This is not intended to be a complete description of the code but just highlight the

differences of moving to a toroidal geometry from the coordinate independent forms given for the two-fluid equations in chapter 2.

The physical values are normalised as follows

$$\mathbf{v_i}^* = \frac{\mathbf{v_i}}{v_A}, \quad \mathbf{v_e}^* = \frac{\mathbf{v_e}}{v_A}, \quad \mathbf{A}^* = \frac{\mathbf{A}}{B_0}, \quad \mathbf{B}^* = \frac{\mathbf{B}}{B_0} \tag{4.5}$$

$$n_e^* = \frac{n_e}{\overline{n_e}}, \quad T_i^* = \frac{T_i}{T_{i0}}, \quad T_e^* = \frac{T_e}{T_{e0}} \tag{4.6}$$

$$p_i^* = n_e^* T_i^* = \frac{p_i}{p_{i0}}, \quad p_e^* = n_e^* T_e^* = \frac{p_e}{p_{e0}}, \tag{4.7}$$

where $v_A = B_0/\sqrt{4\pi m_i \overline{n_e}}$ is a typical Alfvén velocity, $\overline{n_e}$ is the volume averaged electron number density.

4.2.1 Continuity equation

Given the open boundary and particle sources (due to for example neutral beam heating) the mass is not conserved in `CENTORI`. Incorporating the sources with diffusive and a Ware pinch [Ware, 1970] term gives

$$\frac{1}{v_A}\frac{\partial n_e^*}{\partial t} = -\nabla.(n_e^* \mathbf{v_i}^*) + S_n^* - \nu_{i\|}^*(n_e^* - \langle n_e^* \rangle) - \nabla.\Gamma_W^* + \delta_n \tag{4.8}$$

The Ware pinch, which also appears in the ion energy equation, originates from the toroidal electric field used to drive the plasma current. The conservation of canonical angular momentum requires a pinch towards the magnetic axis of the form

$$\Gamma_W^* = \frac{2.44\epsilon^{1/2}}{v_A}\frac{n_e^* c}{|B_{eq,pol}|}\frac{V_F}{2\pi R}\frac{\nabla\psi}{|\nabla\psi|} \tag{4.9}$$

where $V_F \equiv 2\pi R E_F$ is the equivalent loop voltage obtained by the Grad-Shafranov equilibrium solver. The remaining term is the ion parallel thermal relaxation rate, due to Landau damping

$$\nu_{i\|} = f_{\nu_{i\|}}\left(\frac{v_{th,i}}{q\langle R\rangle}\right) + \frac{1}{\epsilon^{1/2}\tau_{ci}} \tag{4.10}$$

where user defined multiplier $f_{\nu_{i\|}} = 0.01$ is set in the input file (although default value is 0.5). Although using simply the difference between the local perturbed density and its flux surface average $(n_e^* - \langle n_e^* \rangle)$ is a crude approximation as the term should have a dependence on the parallel wavenumber, as in for example[Hammett

and Perkins, 1990]. The diffusion term δ_n is given by

$$\delta_n = \frac{2}{3} R_0 \, \mathcal{J} \left\{ \left((D_n + D_{RR}/3) \frac{\partial^2 n_e^*}{\partial \rho^2} \right) + \frac{\langle B_p \rangle^2}{B_p^2} \left(D_n \frac{\partial^2 n_e^*}{\partial \theta^2} \right) \right\} \tag{4.11}$$

which includes a term corresponding to the Rechester-Rosebluth diffusivity (see section 4.2.3 for details), and the particle diffusivity D_n given by

$$D_n(\rho, \theta, \zeta) = \frac{1}{v_A} \left\{ \chi_{e,NC} + \chi_{ne} \left(1 + |\langle q \rangle| \langle R \rangle^2 \sqrt{\frac{m_i}{m_e}} \left[f_{JJ} \, \mathbf{J}^* . \mathbf{J}^* + \mathbf{W}^* . \mathbf{W}^* \right] \right) \right\} \tag{4.12}$$

where χ_{ne} is user-specified, $\mathbf{J}^* . \mathbf{J}^*$ is the normalised entropy and $\mathbf{W}^* . \mathbf{W}^*$ is the normalised enstrophy. f_{JJ} is a user-defined multiplier. These 'eddy-viscosity' terms correspond to the limiting energy dissipation rate being proportional to the enstrophy of a turbulent system as described in section 2.5.1. With the small $\mathbf{J}^* . \mathbf{J}^*$ term arising from the curl of the magnetic fluctuations, as opposed to the curl of the velocity fluctuations at the grid scale.

4.2.2 Momentum equations

The ion momentum is expressed in normalised form as

$$\begin{aligned} \frac{1}{v_A} \frac{\partial \mathbf{v_i^*}}{\partial t} = & - \left[\mathbf{W}^* + \frac{\omega_{ci}}{v_A} \mathbf{B}^* \right] \times \mathbf{v_i^*} - \beta_{i0} \frac{\nabla p_i^*}{n_e^*} - \beta_{e0} \nabla \Phi^* - \frac{1}{2} \nabla (\mathbf{v_i^*} . \mathbf{v_i^*}) - \frac{\omega_{ci}}{v_A^2} \frac{\partial \mathbf{A}^*}{\partial t} + \frac{\mathbf{S_v^*}}{n_e^*} \\ & + \frac{\omega_{ci}}{v_A} \mathbf{B_{eq}^*} \times \left(D_{RR}/3 \, \frac{\nabla \langle n_e^* \rangle}{\langle n_e^* \rangle} \right) - D_v \left(\nabla \times \mathbf{W}^* \right) - \frac{\omega_{ci}}{v_A} \eta^* \mathbf{J}^* \end{aligned} \tag{4.13}$$

Where the advection is calculated using the vorticity $\mathbf{W}^* = \nabla \times \mathbf{v_i^*} / v_A$ adding the corresponding $\nabla (\mathbf{v_i^*} \cdot \mathbf{v_i^*})/2$ term to the right hand side. The normalised velocity diffusivity D_v is expressed in a similar form to the particle diffusivity (Eq 4.12) as

$$D_v(\rho, \theta, \zeta) = \frac{\chi_{v,\text{user}}}{v_A} \left(1 + |\langle q \rangle| \langle R \rangle^2 \sqrt{\frac{m_i}{m_e}} \left[f_{JJ} \, \mathbf{J}^* . \mathbf{J}^* + \mathbf{W}^* . \mathbf{W}^* \right] \right) + \frac{\chi_{v,\text{classical}}}{v_A}.$$

The resistive and turbulent viscosity terms are combined as a diffusion term

$$\delta = -D_v \left(\nabla \times \mathbf{W}^* \right) - \frac{\omega_{ci}}{v_A} \eta^* \mathbf{J}^*$$

The non-orthogonal nature of the coordinate system makes this difficult to translate directly into finite differences. Instead it is approximated as

$$\delta \sim R_0 \, \mathcal{J} \, D_v \left(\frac{\partial^2 \mathbf{v_i^*}}{\partial \rho^2} + \frac{\langle B_p \rangle^2}{B_p^2} \frac{\partial^2 \mathbf{v_i^*}}{\partial \theta^2} \right) \tag{4.14}$$

where the poloidal field is introduced as a factor proportional to the spacing of the grid in that direction. This type of approximation occurs a few times in the code and is one limitation on the accuracy of the model compared to a fully field aligned coordinate system, where the numerical leakage between parallel and perpendicular quantities can be minimized.

The terms of the momentum equation are written as central differences and formed into a block tridiagonal matrix, which is then solved to find $\mathbf{v_i^*}$ at the new timestep.

4.2.3 Energy equations

The divergence of the electron heat flux (Eq. 2.26) term from the energy equation is implemented in terms of the parallel electron thermal relaxation rate and as a diffusion down the temperature gradient

$$-\frac{1}{n_e} \nabla \cdot \mathbf{q_e} = -\nu_{e\parallel} (T_e - \langle T_e \rangle) + \nabla \cdot (X_e \nabla T_e) \tag{4.15}$$

the second term is then approximated as

$$\nabla \cdot (X_e \nabla T_e) \simeq R_0 \mathcal{J} \left[\left((\chi_e + \chi_{RR}) \frac{\partial^2 T_e}{\partial \rho^2} \right) + \chi_e \frac{\langle B_p \rangle^2}{B_p^2} \frac{\partial^2 T_e}{\partial \theta^2} \right] \tag{4.16}$$

The Rechester-Rosenbluth diffusivity term is included to damp radial fluctuations in electron temperature [Rechester and Rosenbluth, 1978]

$$\chi_{RR} = f_{RR} \frac{\nu_{e\parallel} q^2 \langle R \rangle^2}{v_A} \frac{\tilde{B}^2_{\text{normal}}}{B^2} \tag{4.17}$$

where f_{RR} is a user definable parameter, set as 0.5. It should be noted again here that the approximation of multiplying the poloidal term by $\langle B_p \rangle^2 / B_p^2$ to get a pseudo-parallel component leads to an unwanted transfer of heat around the flux surface, rather than being restricted to the true parallel and perpendicular direc-

tions. The energy equations for each species are then written as

$$\frac{1}{v_A}\frac{\partial T_e^*}{\partial t} = -\frac{2}{3}\nu_{e\|}^* T_e^* + \frac{2}{3}\nu_{e\|}^*\langle T_e^*\rangle - \frac{2}{3}T_e^*\nabla\cdot\mathbf{v_e^*} - \mathbf{v_e^*}\cdot\nabla T_e^* + \frac{2}{3}\frac{S_e^*}{n_e^*} \\ +\frac{2}{3}R_0\mathcal{J}\left[\left((D_e + D_{RR})\frac{\partial^2 T_e^*}{\partial\rho^2}\right) + \frac{\langle B_p\rangle^2}{B_p^2}\left(D_e\frac{\partial^2 T_e^*}{\partial\theta^2}\right)\right] \tag{4.18}$$

$$\frac{1}{v_A}\frac{\partial T_i^*}{\partial t} = -\frac{2}{3}\nu_{i\|}^* T_i^* + \frac{2}{3}\nu_{i\|}^*\langle T_i^*\rangle - \frac{2}{3}T_i^*(\nabla\cdot\mathbf{v_i}^* + \nabla\cdot\Gamma_W^*) - \mathbf{v_i}^*\cdot\nabla T_i^* + \frac{2}{3}\frac{S_i^*}{{n_e}^*} \tag{4.19}$$

$$+\frac{2}{3}R_0\mathcal{J}D_i\left[\left(\frac{\partial^2 T_i^*}{\partial\rho^2}\right) + \frac{\langle B_p\rangle^2}{B_p^2}\frac{\partial^2 T_e^*}{\partial\theta^2}\right]$$

where the source terms incorporate the external heating power per unit volume, ohmic heating of electrons, and transfer of energy between species.

$$S_e = P_{aux,e} + P_{ei} + \eta J^2, \qquad S_i = P_{aux,i} + P_{ie} \tag{4.20}$$

$$P_{ei} = -P_{ie} = \frac{3m_e}{m_i}p_{e0}\frac{\langle n_e^*\rangle}{\tau_{ce}}(\langle T_e^*\rangle - \langle T_i^*\rangle) \tag{4.21}$$

4.2.4 Plasma resistivity

The resistivity in `CENTORI` is given as a function of radial coordinate ρ in terms of the Spitzer resistivity [Spitzer Jr., 1952] using the flux surface averaged density and electron temperature, with a correction for the modification due to neoclassical effects in the toroidal geometry.

$$\eta(\rho) = K_\eta\eta_{\text{spitzer}}(\rho) = \frac{1 + {\nu_e}^*}{(1-\epsilon^{1/2})^2 + {\nu_e}^*}\quad\frac{m_e}{2e^2\langle n_e\rangle\tau_{ce}} \tag{4.22}$$

where the electron collision time is

$$\tau_{ce}(\rho) = \frac{3\sqrt{m_e}\langle T_e\rangle^{3/2}}{4\sqrt{2\pi\langle n_e\rangle\lambda e^4}} \tag{4.23}$$

and a dimensionless electron collisionality is given in terms of the safety factor, q and the inverse aspect ratio $\epsilon = a\rho^{1/2}/R_0$ of the flux surface.

$$\nu_e^* = \frac{\sqrt{2}qR_0}{\epsilon^{3/2}v_{th,e}\tau_{ce}} \tag{4.24}$$

The neoclassical factor ensures appropriate behaviour in the banana regime where $\nu_e^* \ll 1$, whilst $K_\eta \to 1$ in the high collisionality limit.

4.3 Matching MAST ohmic discharge

A simulation was set up to match the ohmic conditions of MAST shot 21856, in which the GAM-like mode was observed at 10kHz. The key parameters of the discharge were: $B_0 = 0.5$T, $I_p = 400$kA, $R0 = 0.95$m. The simulation was set up on a grid of 128x128x32 in (ρ, θ, ζ) with a timestep of 0.5ns to satisfy the Courant conditions. Evolution of the equilibrium was performed every 5000 timesteps, giving a temporal resolution of 200kHz, matching that of the reciprocating probe used in MAST. This resolution was found to be sufficient to achieve reasonable convergence of the large scale behaviour, although the combination of poloidal and toroidal resolution was not quite sufficient to resolve drift wave modes corresponding to the highest time resolution of the output. So some aliasing is present in the signals above 100kHz. The full simulation parameter input files are given in Appendix A. The

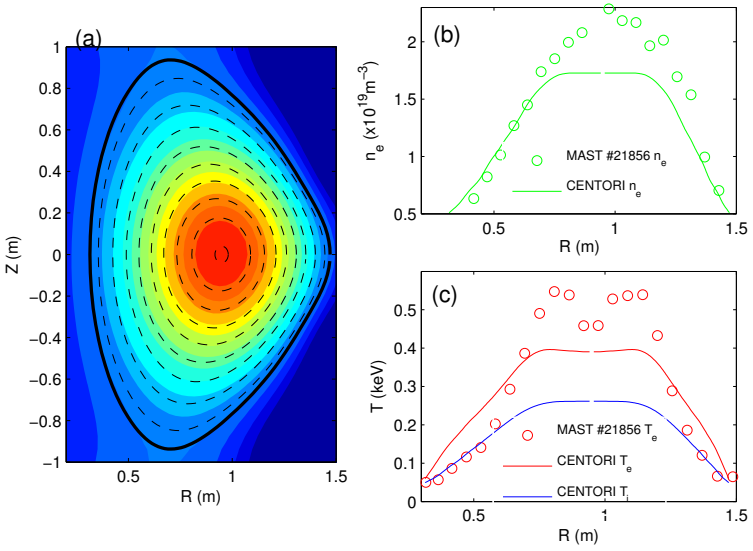

Figure 4.2: (a)EFIT reconstruction of MAST discharge 21856 (filled contours) vs `CENTORI` simulation equilibrium flux surfaces (black lines) (b) Thomson Scattering density vs simulation,(c) Thomson Scattering electron temperature vs simulation

EFIT reconstruction of MAST discharge 21856 was used to match the configuration and initial conditions. As can be seen from figure 4.2(c). the core temperature are not matched well and may be due to insufficient radial resolution close to the axis.

Several simulations were performed with differing background diffusivities to verify that the discrepancy in the core does not affect the behaviour at the edge.

Growth and saturation can be seen in the field and kinetic energy fluctuations summed over the plasma volume in the first millisecond of the simulation, as shown in figure 4.3. This first 1ms of the simulations was discarded and the following 4ms used for analysis. The kinetic energy becomes dominated by the growth of a low frequency mode, which shows no correlating part in the magnetics illustrating the electrostatic nature of the mode. The saturated fluctuating energies do not reach absolute steady state and continue to slowly rise, suggestive of a slight imbalance in the sources and sinks of the open boundary conditions.

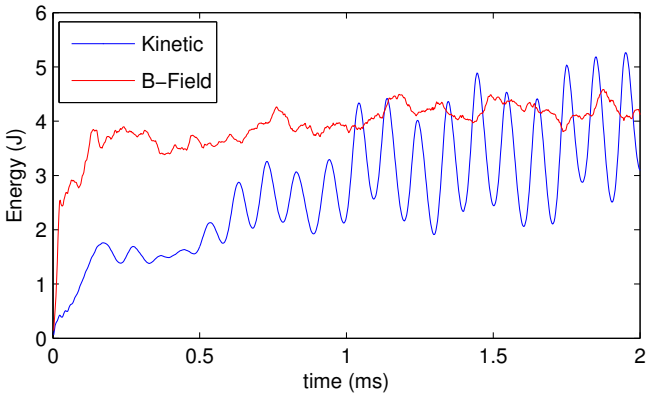

Figure 4.3: Fluctuating part of kinetic and magnetic field energy summed over the plasma volume over time.

4.4 Mode structure

The strong electrostatic mode spontaneously develops from the random seed variations with $m = n = 0$ in potential and an up/down asymmetric m=1 dominant component in the density fluctuations. Scripts were used to convert from the `CENTORI` native file format using the supplied IDL based analysis tool '`CENTORIScope`', via Matlab® to `.vtk` format, which can then be visualized using VisIt [Childs et al., 2005], as shown in figure 4.4. In the highly shaped plasma residual $m > 1$ density fluctuations reach the inboard and outboard midplane. Figure 4.5, shows a poloidal slice of the normalized potential and density fluctuations of the fully developed mode. The growth and saturation of the mode over the first millisecond of the simulation can be seen in figure 4.6(a) after which time the density fluctuations remain roughly constant with an outward propagating phase. The radial structure and propagation

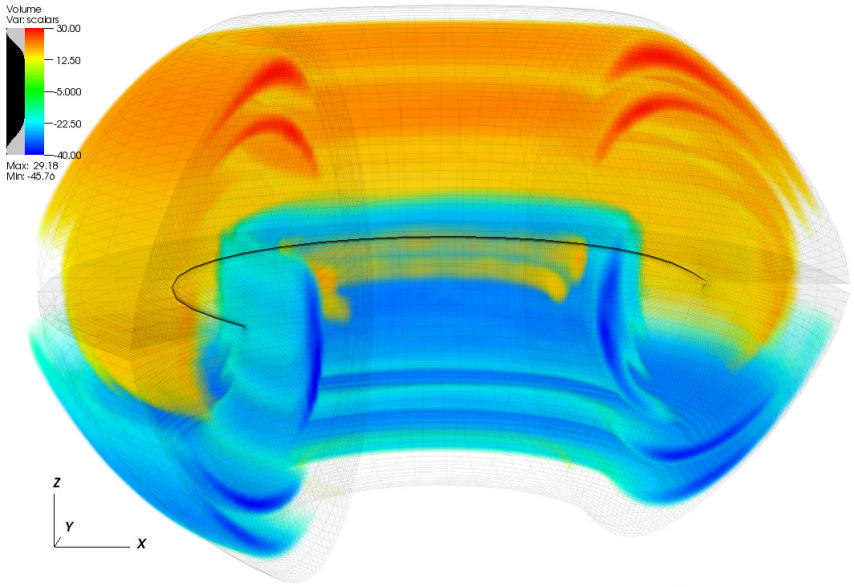

Figure 4.4: 3D volumetric plot of density fluctuations, showing $n = 0$, $m = 1$ structure.

is illustrated in 4.6(b), showing a series of profiles at $\Delta t = 10\mu s$ intervals forming the radial envelope of the mode. Taking profiles of the density fluctuations along the radial contours $\theta = 0, \pi/2, \pi, 3\pi/2, 2\pi$, the root mean square density fluctuation level $\mathrm{rms}(\tilde{n}(t)/\langle n \rangle)$ with radius is found to vary around the poloidal cross-section with a slight asymmetry between top and bottom as shown in figure 4.6(c), which also shows a $\tilde{n}/\langle n \rangle \sim 3\%$ level of fluctuations propagating to the outboard midplane, and upto 8% on the inboard side, but peaking at a slightly smaller normalised radius. Floating potential measurements were obtained 4cm inside the last closed flux surface, on the outboard midplane, over a 3ms time interval, with a sampling rate of 400 kHz, in MAST discharge 21856. Numerical data were obtained from a `CENTORI` simulation of this discharge, for the same spatial location (the average potential of two radial grid cells was used) and with the same sampling rate. The resultant power spectra are plotted in figure 4.7, normalised to the standard deviation of the fluctuations over the interval. Minimal smoothing was also applied to both power spectra to reduce the noise in order to bring out the features of interest. The simulation and experiment show remarkable agreement in slope of $\approx f^{-2}$, both on the low and high frequency side of the GAM peak, and in magnitude.

The radial wavelength varies over the width of the mode, so the wavenumber

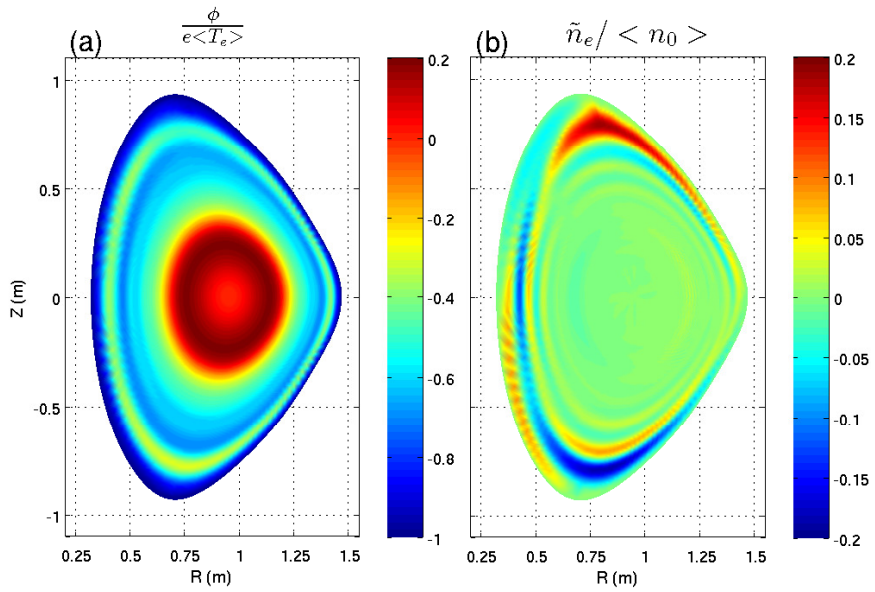

Figure 4.5: Snapshot at t=2.58ms of (a) potential, normalised to flux surface average electron temperature, showing dominantly m=0 structure, and (b) density fluctuation, normalised to the flux surface average over 1ms, showing mainly m=1 up/down mode, but with significant deviation due to shaping.

more easily determined by tracking the phase velocity of each fluctuation peak in turn as it propagates outwards along the $\theta = \pi/2$ contour over the time window $t = 2-5$ms as show in figure 4.8(a). The wavenumber is then found from the relation $v_p = \omega/k$, with the assumption that the dominant frequency is constant over the width of the plateau. The radial phase velocity is seen to rise from ≈ 1.5km/s at a normalised radius of $\psi^{1/2} = 0.86$ to ≈ 3.0km/s at $\psi^{1/2} = 0.92$, before dropping back towards the edge. This falloff at the edge is likely to be an artefact of the fixed density boundary condition. The wavelength corresponding to $\hat{k} = 0.05 - 0.1$ is in the range 15-30cm towards the X-points.

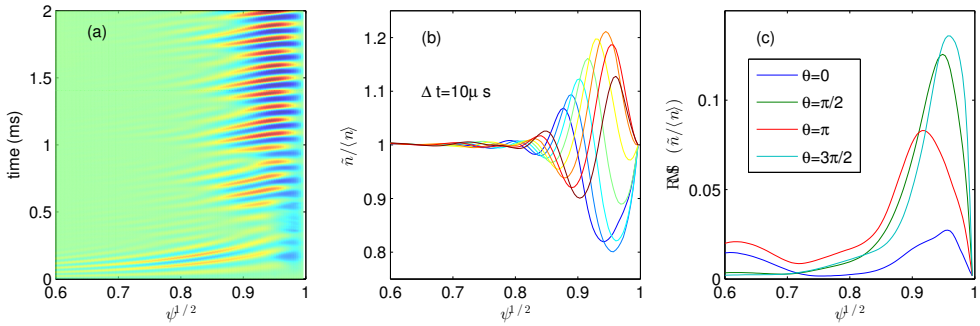

Figure 4.6: (a) Time evolution of density fluctuations with radius along $\theta = \pi/2$ for the first 2ms of simulation (b) Series of snapshots of density fluctuation at $10\mu s$ intervals showing envelope and outward phase propagation (c) Root-mean-square of density fluctuations for t=2-5ms at different poloidal coordinates.

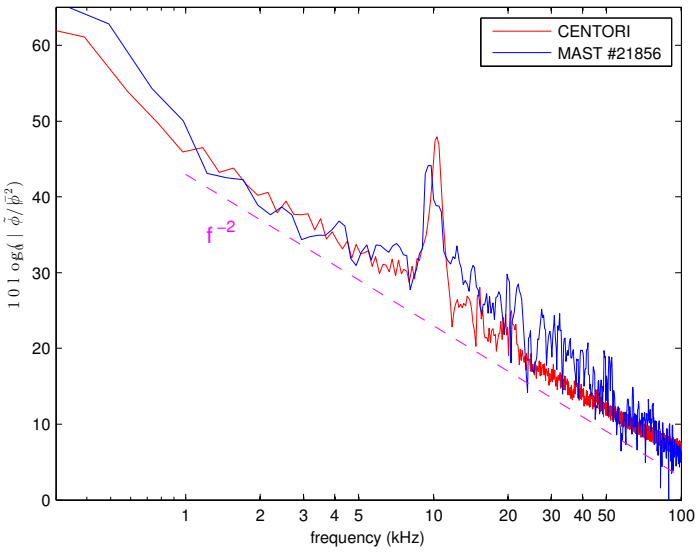

Figure 4.7: Power spectra of potential fluctuations on the outboard midplane 4cm inside the last closed flux surface.

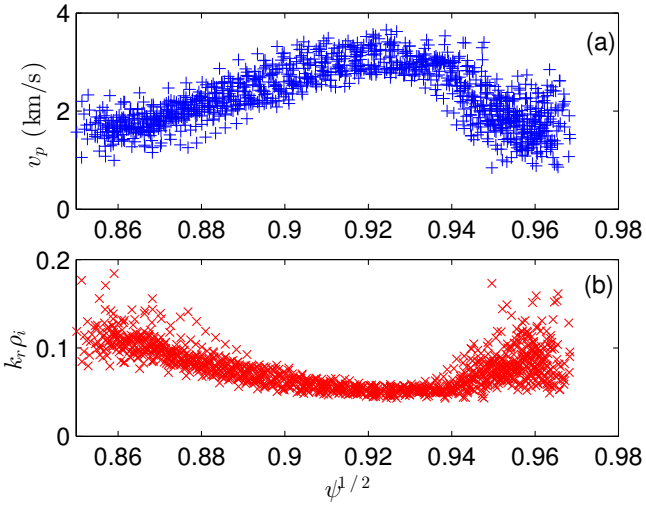

Figure 4.8: (a) Radial (outward) phase velocity of peaks in density fluctuation, (b) normalized radial wavenumber $\hat{k} = k_r \rho_i$ where $k_r = \omega_{\mathrm{GAM}}/v_p$.

4.5 Discussion

The two-fluid simulations show strong $m = n = 0$ potential and $m = 1, n = 0$ density fluctuations, with the frequency showing remarkable agreement with the experimental measurements in MAST [Robinson et al., 2012], confirming the observed mode as a GAM. Also the simulations show in the highly shaped configuration of MAST that although the $m = 1$ up/down nature of the density fluctuations is dominant, one can expect a small, but experimentally measurable, perturbations at the outboard midplane, as was seen. Whilst the boundary conditions of the simulation fix the temperatures at the edge, and so the sound speed, to the experimentally motivated values; the near perfect agreement of the power spectra shown in figure 4.7, suggests the modification of the mode frequency by the geometry is being simulated accurately.

Chapter 5

Simulations of geodesic acoustic modes in strongly shaped tight aspect ratio tokamak plasmas

"An approximate answer to the right problem is worth a good deal more than an exact answer to an approximate problem."

— John Tukey

5.1 Introduction

Further to the simulation using `CENTORI` of MAST-like conditions, a series of simulations were performed to investigate the variation of GAM frequency with elongation and aspect ratio.

5.2 Theoretical GAM shaping factors

While there have been many studies of the GAM under idealized large aspect ratio, circular cross section conditions [Elfimov et al., 2011; Lakhin et al., 2010; Qiu et al., 2009; Smolyakov et al., 2008], in which useful insights can be made on the growth, damping mechanisms, and dispersion relations (see section 2.10). The extension to tight aspect ratios and realistic shaping parameters is more difficult. One approach [Gao, 2011, 2010] extends the collisionless damping model of [Qiu et al., 2009] by invoking the large or small orbit drift width (ODW) limit, i.e. the ratio of the

magnetic drift frequency to the poloidal transit frequency, ω_d/ω_t

$$\omega_d = k|\nabla r|\hat{\mathbf{x}}\cdot\mathbf{b}\times(\mu\nabla B + mv_\parallel^2\mathbf{b}\cdot\nabla\mathbf{b})/m\Omega \tag{5.1}$$

$$\omega_t = v_\parallel B_p/[(dl/d\theta)B] \tag{5.2}$$

Gao starts the derivation by introducing a fluctuating zonal potential as

$$\phi = \sum_{\omega,k}\hat{\phi}(\theta)\exp(ikx|\nabla r| - i\omega t) \tag{5.3}$$

to an equilibrium with elliptical flux surfaces (R_s, Z_s), where $R_s = R_0(r) + r\cos\theta$, and $Z_s = \kappa(r)r\sin\theta$. The ion response is then split into the adiabatic, and non-adiabatic parts

$$\hat{f} = -qF_0\hat{\phi}/T + \hat{h}J_0(\delta) \tag{5.4}$$

with the non-adiabatic part satisfying the linear gyrokinetic equation

$$\left(1 - \frac{\omega_d}{\omega} + \frac{i\omega_t}{\omega}\partial_\theta\right)\hat{h} = \frac{e\hat{\phi}}{T}J_0(\delta)F_0 \tag{5.5}$$

where F_0 is a Maxwellian distribution, J_0 is the zeroth-order Bessel function and $\delta = k\rho_i(v_\perp B_0/v_{ti}B)$. This is then solved in terms of inverse aspect ratio ϵ, elongation κ, Shafranov shift gradient Δ', safety factor q, and temperature ratio $\tau = T_e/T_i$. The gradient of the elongation also appears as $s_\kappa = (r/\kappa)\partial_r\kappa \approx (\kappa - 1)/\kappa$. It should be stressed this derivation assumes ϵ, s_κ, Δ',$1/q \sim O(\epsilon)$ are all small parameters. In our case these have values of $\epsilon = 0.4 - 0.6$, $s_\kappa \approx 0.3$, $\Delta' \approx -0.2$, and $1/q \approx 0.2$, so are pushing the validity bounds of the model.

Using the small ODW limit, appropriate for MAST conditions, of [Gao, 2011] for $\omega_d \ll \omega_t$, but neglecting the small corrections due to Shafranov shift gradient, the GAM frequency is given by

$$\begin{aligned}\frac{\omega_{\mathrm{GAM}}}{v_{T_i}/R_0} = &\sqrt{\left(\frac{7}{4}+\tau\right)\left(\frac{2}{\kappa^2+1}\right)\left(1 - \frac{s_\kappa}{2}\frac{7+2\tau}{7+4\tau}\right)\left(1 - \epsilon^2\frac{9\kappa^2+3}{8\kappa^2+8}\right)} \\ &\times\left[1 + \frac{\kappa^2+1}{4q^2}\left(\frac{23}{8} + 2\tau + \frac{\tau^2}{2}\right)\left(\frac{7}{4}+\tau\right)^{-2}\right].\end{aligned} \tag{5.6}$$

The growth rate of the mode is also given by the theory, but here we will concentrate on the mode frequency as matching the expected absolute magnitude of the saturated mode from the balance of driving and damping terms is beyond the scope of this work. However [Gao, 2010] noted that in the limit $q \to \infty$, the GAM damping

rate is weakened by the elongation, as a possible explanation why the GAM is easily excited in strongly elongated plasmas. The large ODW limit gives a similar form for the frequency that yields only a few percent difference for the small value of $\hat{k}$ deduced from the phase velocity in chapter 4, but has a different damping rate, as detailed in [Gao, 2011].

5.3 Variation with R_0

The dominant term modifying the original GAM frequency expression of Winsor, Eq. (2.109), in Eq. (5.6) is the $\approx (1-\epsilon^2)$ factor. So, in order to test the agreement of the analytical prediction of Eq. (5.6) with simulations, a series of runs were performed keeping all the key parameters the same ($B_0 = 0.5$T,$I_p = 0.5$MA), except moving the major radius of the magnetic axis R_0, from the MAST configuration of 95cm inwards to 85cm, and outwards to 110, 120 and 150cm, as show in figure 5.1. The poloidal and divertor field coils were also moved out to keep the overall

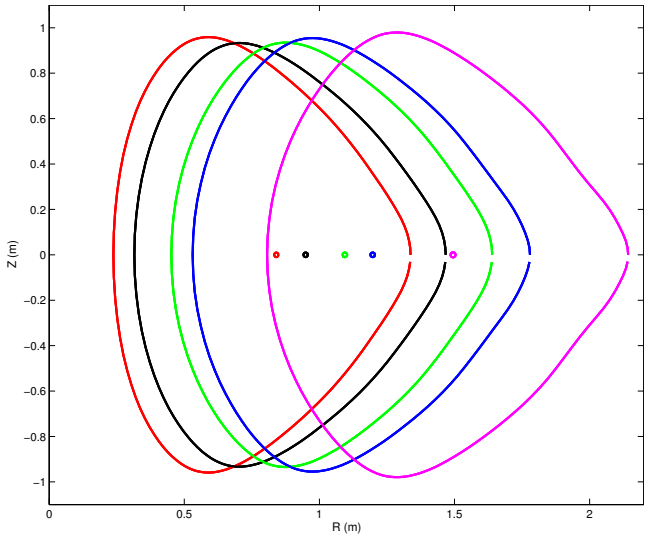

Figure 5.1: Simulation flux surface position and shape with increasing major radius

shaping broadly similar, but with the plasma relaxing to find its own equilibrium, giving an elongation reducing from 1.85 to 1.43, and safety factor at the position of the peak GAM reducing from $q = 7.96$ in the very tight 85cm case to $q = 2.87$ at 150cm. A GAM-like mode was observed in all cases with the frequency only reducing from 10.6kHz at $R_0 = 85$cm to 7.98kHz at $R_0 = 150$cm despite the $1/R_0$ dependence of the large aspect ratio approximation with constant temperature. Taking the constant $\theta = \pi/2$ radial contour a Fourier transform was taken over a

	Simulation parameters at main GAM plateau						Predicted
$R_0(m)$	$\psi^{1/2}$	ϵ	κ	q	$T_e/T_i(eV) = \tau$	f_{centroid}	f_{pred} (kHz)
0.85	0.935	0.557	1.85	7.96	119/73=1.64	10.6	8.85
0.95	0.938	0.503	1.65	5.94	112/70=1.60	10.5	9.43
1.10	0.942	0.468	1.55	4.45	105/71=1.48	9.82	8.93
1.20	0.947	0.453	1.52	3.78	101/70=1.44	9.57	8.47
1.50	0.956	0.403	1.43	2.87	97/72=1.35	7.98	7.68

Table 5.1: Key parameters for outer GAM plateau centroid peak locations

3ms window once the simulation had reached approximately steady state conditions at each position.

A linear global eigen-mode treatment of the functional dependence of GAM frequency with radial position would form non-overlapping regions. However, in the non-linear simulations, as with experimental observations, such as those in ASDEX Upgrade [Conway and the ASDEX Upgrade Team, 2008], the radial frequency plateaux can be seen in the density fluctuations to overlap, as shown in figure 5.2, where the colour scale is $\log(|\tilde{n}_e/n_0|^2)$. Overlaid are lines for the sound transit frequency $c_s/2\pi R_0$ and the predicted local GAM frequency. The series of plateaux can be seen to extend deeper into the core of the smaller radius plasmas. Interpreting figure 5.2, the mode at each excited frequency appears to propagate outwards until that frequency approaches the local sound transit frequency where it is damped. So for the cases where the region between the lines is large, the mode can exist as multiple overlapping plateaux. The position of the main (outer) GAM peak can also be seen to be pushed out slightly in the large R_0 (low q) case going from normalized radius $\psi^{1/2} = 0.935$ to $\psi^{1/2} = 0.956$, as summarised in table 5.1. Also, the relative amplitude of the second plateau grows with respect to the outer mode, so by $R_0 = 1.5$m they are on a par with each other. It should be noted that due to numerical limitations the simulation region cannot extend fully to the X-points and so the grid boundary is at 95% of the equilibrium flux at the last closed flux surface.

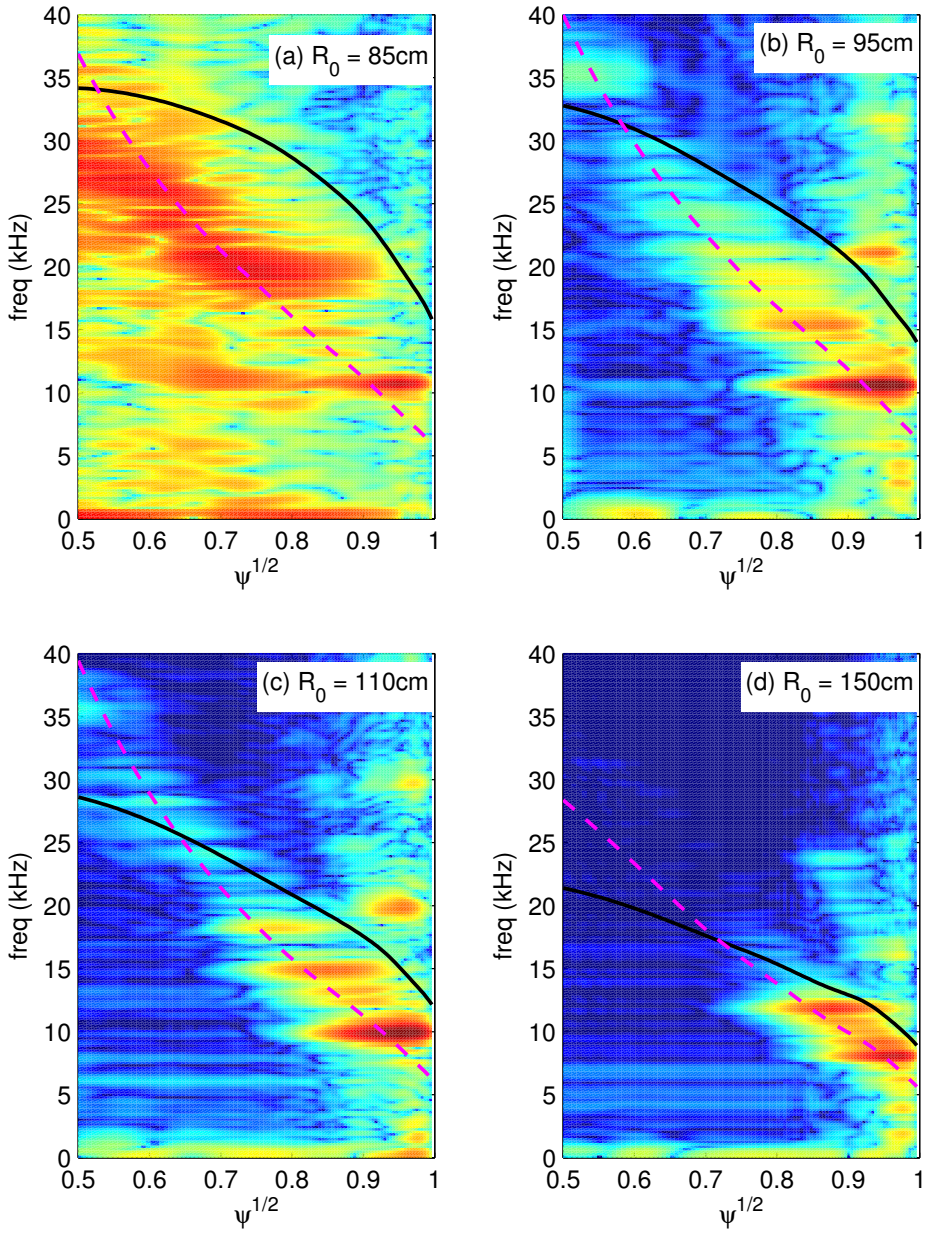

Figure 5.2: Density fluctuation power for $R_0 = 85$cm,(b)$R_0 = 95$cm,(c)$R_0 = 110$cm, and (d)$R_0 = 150$cm. Black line shows the sound speed transit frequency $f_{c_s} = c_s/(2\pi R_0)$, the magenta dashed line is the predicted local GAM frequency from equation (5.6).

5.4 Results

We compare the value of the frequency at the centroid of the main and second plateaux from each simulation with the analytical model by inserting the local values q,κ,ϵ and τ into (5.6), shown in figure 5.3, where the horizontal error bars of $\pm$500Hz correspond to the FFT resolution, and the vertical error bars represent the sensitivity of the analytical prediction to a variation of $\pm$20% in τ. Taking all the results over the wide variety of parameters the simulations show a strong linear relationship, ($R^2 = 0.966$) with the ODW model as expressed by Eq. (5.6), but underestimating the GAM frequency by 12%. This is evident from figure 5.2(a–d), where the predicted frequency (magenta dashed lines) coincide with the inner edge of the plateaux rather than the points where they reach maximum amplitude. The

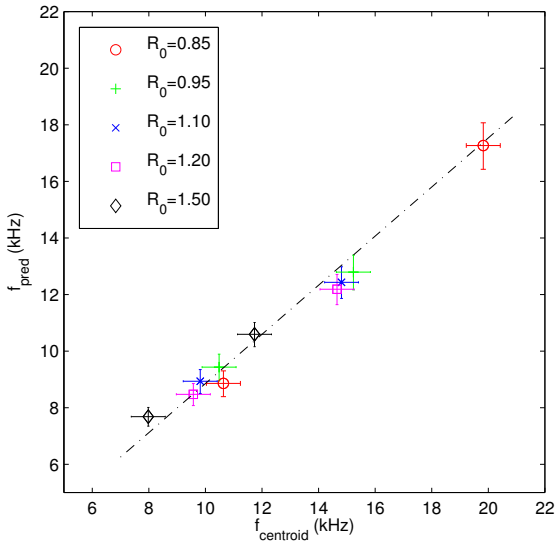

Figure 5.3: Simulation vs predicted GAM frequency for main and secondary plateaux. Linear fit: gradient=0.88 ± 0.12, $R^2 = 0.966$.

linear agreement with theory from the GAM under MAST-like size and shaping from chapter 4 over the range of different aspect ratios given here provides good confidence that `CENTORI` is capturing the electrostatic behaviour correctly, and acts as a strong benchmark test of the code. The 12% discrepancy in frequency at the position of maximum amplitude is within the expectation of the differing gyro-kinetic versus fluid approach of the models.

Chapter 6

Conclusion

In this work we take a holistic approach to study GAMs in spherical tokamak, such as MAST. We not only directly compare theoretical dispersion relation to this observed in MAST, but also use two-fluid simulations to verify that the observed mode can indeed be interpreted as the GAM. After a broad introduction to fusion power and plasma physics, the role of turbulence driven zonal flows, and the geodesic acoustic mode is investigated. The first identification of the GAM in MAST is presented with evidence that they are affected by the application of resonant magnetic perturbations. The hypothesis that it is the rotation induced by the RMPs is the cause for the upwards frequency shift of the GAM is postulated and shown to give good agreement with a simple analytical model. Then on achieving a threshold the mode is damped, possibly due to interaction of the mode with the Alfvénic perturbations as seen by the plasma in the rotating frame.

Simulations using `CENTORI` confirmed the mode structure as a GAM and together with a series of simulations at larger aspect ratios were compared to the orbit drift width model of [Gao, 2011]. The agreement between the theory and simulations provide good confidence that the code is capturing the physics of the electrostatic mode to sufficient accuracy. However, the 12% frequency disparity of the fluid simulation versus the gyro-kinetic theory seen in chapter 5, when contrasted with the good agreement between the simulation and experimental observations of chapter 4, suggest it is the theoretical model that is not capturing the correct behaviour in the highly shaped, tight aspect plasmas considered. This is not surprising given the relative sizes of the "small parameters". Also of question is the validity of the $\gamma_i = 7/4$ ion adiabatic index that emerges from form of pressure anisotropy taken in the collisionless gyro-kinetic approach [Nguyen et al., 2008], that appears in the sound speed term $c_s = \sqrt{(T_e + \gamma_i Ti)/m_i} = v_{T_i}\sqrt{7/4 + \tau}$, particularly at the cool

edge where the collisionality is higher. Recently Gao [2013] showed the gyro-kinetic $(7/4+\tau)$ term reduces to the isotropic fluid-like $(1+\tau)$ in a high collisionality limit.

Development of the code is ongoing at CCFE, for example incorporating plasma rotation into the equilibrium solver, allowing for future simulations with higher Mach number, and more complex rotation velocity profiles. The addition of RMPs into the code could be treated as a small perturbation and should not require the shift to a fully three-dimensional equilibrium solver over the present axissymmetric scheme. One last comment is that at present `CENTORI` does not include any form of gyroviscous cancellation, while only a small $O(\delta^2)$ term, may play a crucial role governing the height of the pedestal in H-mode, since near the top of the pedestal, where the temperature and density are relatively high, and the gradient becomes steep will be the point where δ reaches its maximum. It would be interesting to add a gyroviscous term, and compare the resulting equilibrium density and temperature profiles reached.

6.1 Future work

A new series of simulations is under way, extending the cases of chapter 5 to higher current discharges, with and without auxiliary heating. In connection with these a series of experiments has been proposed on MAST, and are currently scheduled in two parts as priority 1 for the next MAST experimental campaign running from March-July 2012. Before MAST shuts down for a major upgrade. The first part is to verify the results of chapter 2 using various new diagnostics fitted or upgraded since the data studied was taken. In particular the beam emission spectroscopy (BES) system [Field et al., 2012] and the new Thomson scattering (TS) system in burst mode [Gibson et al., 2010].

The new TS system comprises eight Nd::Yag lasers capable of firing at 30Hz, yielding a 130 point profile for n_e and T_e across the midplane with 4ms resolution when evenly spaced. However the laser timings can be adjusted to give an eight point burst with only a few microseconds delay. Thus to detect fluctuations around 10kHz the timing can be set to cover two wave periods across the eight pulses giving a required offset of $25\mu s$.

Provided the GAM can be successfully identified in the non-intrusive diagnostics. The second part of the proposed experiments will move towards the L-H transition, by increasing the ohmic current and neutral beam heating, where the reciprocating probe cannot be used due to the heat load. The neutral beam also enables, the corresponding ion temperature to be measured using charge ex-

change recombination spectroscopy (CXRS), alternatively the new deuterium gas puff method [Morgan, 2011] could be used giving increased resolution at the edge.

Beyond the MAST experiments work is also planned on extending the GAM simulations to JET and eventually ITER sized plasmas. Where the numerical challenge is harder given the large scale separation between the ion gyro scale and the device size, requires an increased resolution.

6.2 Final words

As mentioned several times, the success of magnetic confinement fusion as a viable power source for the future, largely depends on developing sufficient understanding of the turbulent processes and associated instabilities that dominate the transport of heat and particles out of the plasma. The mitigation of edge localised modes by the use of magnetic perturbations is hoped to give the level on control required to operate the next generation tokamak, ITER, currently under construction. The frequency range and sensitivity to plasma conditions of the GAM could provide a useful diagnostic to probe the non-linear mechanisms coupling drift wave turbulence and zonal flows, yielding important insights into the formation and stability of transport barriers and the H-mode pedestal. Conversely, they could potentially be artificially excited by external driving as an alternative mechanism for controlling the flow of energy from small to large scales. So in summary, this thesis offers an insight into a class of non-linearly driven oscillations of a complex turbulent system, with a three-way comparison between experiment, simulation and theory. Although just scratching the surface of this growing field, it offers the opportunity for continued iteration and comparison with improved diagnostics on the experimental side, and improved modelling incorporating next order corrections to the equations and combining magnetic perturbations with rotation and other factors to the simulations.

Appendix A

Sample CENTORI input files

The CENTORI key input files are [centori.in] and [grass.in]. Lines starting with [*] are comments

A.1 centori.in

```
* CENTORI Global Input File
*** ************************************************************************
***                                                                          *
***** MAST standard case                                                    *
*** ************************************************************************
***   Invariant specifications                                               *
***
NRGRID              = 128
NZGRID              = 129
RMIN                = 0.0
RMAX                = 200.0
ZMIN                = -200.0
ZMAX                =  200.0
RPMIN               = 7.5
RPMAX               = 145.0
ZPMIN               = -150.0
ZPMAX               =  150.0
*******************************************************************************
* Max length=50:  12345678901234567890123456789012345678901234567890
RUN_DESCRIPTION = JR101:NOUT=1;NEQUIL=500;NT=5000;129x129x33;128pro
***
DUMPFORMAT          = 0
***
```

```
*** If DUMP_ALL_ZETA is set to 1, all zeta values will be available
DUMP_ALL_ZETA       = 0
***
*** Time step in  secs.
DT                  = 0.5D-9
***
*** Processor distributions
NX_SPROC            = 8
NY_SPROC            = 8
NZ_SPROC            = 2
***
*** Grid sizes
***
NPSI                = 129
NTHETA              = 129
NZETA               = 33
***
*** Output control parameters
***
*** Number of equilibria per run
NEQUIL              = 500
*
*** Number of outputs per equilibrium
*** 20 mu.s per output
NOUT                = 1
*
*** Number of time steps per output
NT                  = 5000
*
*** Total number of time steps NOUTxNEQUILxNT
*** Run length No. time stepsxDT =1 ms
*** COLD_START=1 indicates a cold start; 0 is a WARM start
COLD_START          = 0
***
*** Equilibrium parameters
***
BREF                = 0.5D4
RREF                = 95.0
RES_GRASS_INDEX     = 2.0
***
*** Plasma current in Amps
PLASMA_CURRENT      = 0.5D6
```

```
*
*** B0 in Gauss
*
BZERO               = 0.5D4
*
*** ne0 in particles/cc
NEZERO              = 2.15D13
*
*** Te0, Tio in keV
TEZERO              = 0.54
TIZERO              = 0.4
*
ALPHAN              = 1.6
POWER_E0            = 1.0D0
ALPHA_POWE          = 3.0D0
POWER_I0            = 1.0D0
ALPHA_POWI          = 3.0D0
PARTICLE_SRC        = 1.0D17
VITOR0              = 0.01
ALPHAVI             = 1.6
ALPHATE             = 2.2
ALPHATI             = 2.1
***  Momentum source strength restored
SRC_VTOR_MULT       = 0.75
DENSITY_FEEDBACK    = 1
*** Target average density
TARGET_NE           = 1.1D13
*
*** Density feed-back relaxation time  (secs)
TAU_SN              = 1.0D-4
POSITION_CONTROL    = 1
RTARGET             = 95.0
*** ************************************************************************
*** Diffusion factors (cm.sq/sec)
***
*** Density Dne
CHI_NE              = 0.75D4
*
*** Chi-e
CHI_TE              = 0.4D4
*
*** Chi-i
```

```
CHI_TI              = 0.1D4
*
*** Kinematic viscosity (was 0.2)
CHI_VI              = 0.2D4
*
***  Resistive diffusivity (was 0.0125)
CHI_RES             = 0.0125D4
*
*** ************************************************************************
***   Some multipliers
***   Rechester-Rosenbluth doubled to 0.5 (16/10/2011)
RRMULT              = 0.5
*
***   Entropy
JSQ_DMULT           = 1.0
*
***
CHI_CLASSICAL_MULT  = 0.0
***   Landau multiplier (new nupi practice: 16/10/2011)
NUPI_MULT           = 0.01
* IONMASS: 1.67D-24 = H, 3.34D-24 = D, 5.01D-24 = T
IONMASS    = 3.34D-24
```

A.2 grass.in

```
8 *** COILS: ncoils, then rcoil(cm), zcoil(cm), drcoil(cm), dzcoil(cm), icoil(A)
 47.35  165.0    5.0  22.7    87.0D3  ; P2iu, 12 turns
 47.35 -165.0    5.0  22.7    87.0D3  ; P2il, 12 turns
 52.65  161.2    5.0  15.1    58.0D3  ; P2ou,  8 turns
 52.65 -161.2    5.0  15.1    58.0D3  ; P2ol,  8 turns
150.0   110.0   15.4  15.4  -101.4D3  ; P4u,  23 turns
150.0  -110.0   15.4  15.4  -101.4D3  ; P4l,  23 turns
165.0    50.0   15.4  15.4  -73.5D3  ; P5u,  23 turns
165.0   -50.0   15.4  15.4  -73.5D3  ; P5l,  23 turns
0 *** LIMITERS: nlim, then rlim(cm), zlim(cm)
142.0 0.0
120.0 50.0
120.0 -50.0
```

Bibliography

Hannes Alfvén. *Cosmical Electrodynamics*. Oxford University Press, 1950.

Stepfano Azteni and Jürgen Meyer-ter-Vehn. *The Physics of Inertial Fusion*. Oxford University Press, 2004. ISBN 0198562640.

Dieter Biskamp. *Nonlinear Magnetohydrodynamics*. Cambridge University Press, new ed edition, July 1997. ISBN 0521599180.

David Bohm. *The characteristics of electrical discharges in magnetic fields*. McGraw-Hill, 1949.

S I Braginskii. *Zh. Eksp. Teor. Fiz [Sov. Phys. JETP 6, 358 (1958)]*, (33):645, 1957.

S I Braginskii. *Transport Processes in a Plasma*. Number 1. Consultants Bureau, New York, 1965.

L.E.J. Brouwer. Über abbildung von mannigfaltigkeiten. *Mathematische Annalen*, 71(4):598–598, 1912. ISSN 0025-5831. doi: 10.1007/BF01456812. URL http://dx.doi.org/10.1007/BF01456812.

Suzana J. Camargo, Dieter Biskamp, and Bruce D. Scott. Resistive driftwave turbulence. *Physics of Plasmas*, 2(1):48–62, January 1995. ISSN 1070664X. doi: doi:10.1063/1.871116. URL http://dx.doi.org/10.1063/1.871116.

J. R. Cash and A. H Karp. A variable order runge-kutta method for initial value problems with rapidly varying right-hand sides. *ACM Transactions on Mathematical Software (TOMS)*, 16(3):201222, 1990.

P. J. Catto and A. N. Simakov. A new, explicitly collisional contribution to the gyroviscosity and the radial electric field in a collisional tokamak. *Physics of Plasmas*, 12(11):114503–114503–4, November 2005. ISSN 1070664X. doi: 10.1063/1.2136355. URL http://dx.doi.org/10.1063/1.2136355.

Peter J. Catto and Andrei N. Simakov. A drift ordered short mean free path description for magnetized plasma allowing strong spatial anisotropy. *Physics of Plasmas*, 11(1):90–102, January 2004. ISSN 1070664X. doi: 10.1063/1.1632496. URL http://dx.doi.org/10.1063/1.1632496.

Peter J. Catto and Andrei N. Simakov. Erratum: A new, explicitly collisional contribution to the gyroviscosity and the radial electric field in a collisional tokamak [Phys. plasmas 12, 114503 (2005)]. *Physics of Plasmas*, 13(12):129901–129901–1, December 2006. ISSN 1070664X. doi: 10.1063/1.2402507. URL http://dx.doi.org/10.1063/1.2402507.

C. S. Chang and F. L. Hinton. Effect of finite aspect ratio on the neoclassical ion thermal conductivity in the banana regime. *Physics of Fluids*, 25(9):1493–1494, September 1982. ISSN 00319171. doi: doi:10.1063/1.863934.

J G Charney. *J. Meteorol.*, 6:371, 1949.

Hank Childs, Eric S. Brugger, Kathleen S. Bonnell, Jeremy S. Meredith, Mark Miller, Brad J. Whitlock, and Nelson Max. A contract-based system for large data visualization. In *Proceedings of IEEE Visualization 2005*, pages 190–198, 2005.

B. V. Chirikov. *Journal of Nuclear Energy. Part C, Plasma Physics, Accelerators, Thermonuclear Research*, 1:253, 1960.

G D Conway and the ASDEX Upgrade Team. Amplitude behaviour of geodesic acoustic modes in the ASDEX upgrade tokamak. *Plasma Physics and Controlled Fusion*, 50(8):085005, August 2008. ISSN 0741-3335. doi: 10.1088/0741-3335/50/8/085005. URL http://iopscience.iop.org/0741-3335/50/8/085005/.

G D Conway, C Trster, B Scott, K Hallatschek, and the ASDEX Upgrade Team. Frequency scaling and localization of geodesic acoustic modes in ASDEX upgrade. *Plasma Physics and Controlled Fusion*, 50(5):055009, May 2008. ISSN 0741-3335, 1361-6587. doi: 10.1088/0741-3335/50/5/055009. URL http://iopscience.iop.org/0741-3335/50/5/055009.

R. Courant, K. Friedrichs, and H. Lewy. On the partial difference equations of mathematical physics. *Mathematische Annalen*, 100:3274, 1928. URL http://www.stanford.edu/class/cme324/classics/courant-friedrichs-lewy.pdf.

S. C. Cowley, R. M. Kulsrud, and R. Sudan. Considerations of ion-temperature-gradient-driven turbulence. *Physics of Fluids B: Plasma Physics*, 3(10):

2767–2782, October 1991. ISSN 08998221. doi: 10.1063/1.859913. URL http://dx.doi.org/10.1063/1.859913.

J M Dewhurst, B Hnat, and R O Dendy. Finite larmor radius effects on test particle transport in drift wave-zonal flow turbulence. *Plasma Physics and Controlled Fusion*, 52(2):025004, February 2010. ISSN 0741-3335. doi: 10.1088/0741-3335/52/2/025004. URL http://dx.doi.org/10.1088/0741-3335/52/2/025004.

Joseph Michael Dewhurst. *Statistical description and modelling of fusion plasma edge turbulence*. PhD thesis, University of Warwick, April 2010. URL http://wrap.warwick.ac.uk/3903/.

P H Diamond, S-I Itoh, K Itoh, and T S Hahm. Zonal flows in plasmaa review. *Plasma Physics and Controlled Fusion*, 47(5):R35–R161, May 2005. ISSN 0741-3335. doi: 10.1088/0741-3335/47/5/R01. URL http://dx.doi.org/10.1088/0741-3335/47/5/R01.

J.R. Dormand and P.J. Prince. A family of embedded Runge-Kutta formulae. *Journal of Computational and Applied Mathematics*, 6:19–26, 1980.

B. D. Dudson, R. O. Dendy, A. Kirk, H. Meyer, and G. F. Counsell. Comparison of L- and H-mode plasma edge fluctuations in MAST. *Plasma Physics and Controlled Fusion*, 47(6):885–901, 2005. ISSN 0741-3335. URL http://dx.doi.org/10.1088/0741-3335/47/6/010.

P. D. Dura, B. Hnat, J. Robinson, and R. O. Dendy. Vorticity scaling and intermittency in drift-interchange plasma turbulence. *Physics of Plasmas*, 19(9): 092301–092301–7, September 2012. ISSN 1070664X. doi: 10.1063/1.4751473. URL http://dx.doi.org/10.1063/1.4751473.

EDFA-JET. URL http://www.efda.org/2011/09/tokamak-principle-2.

A G Elfimov, R M O Galvo, and R J F Sgalla. Rotation effect on geodesic and zonal flow modes in tokamak plasmas with isothermal magnetic surfaces. *Plasma Physics and Controlled Fusion*, 53(10):105003, October 2011. ISSN 0741-3335, 1361-6587. doi: 10.1088/0741-3335/53/10/105003. URL http://iopscience.iop.org/0741-3335/53/10/105003.

L. Euler. Principles géneraux du mouvement des fluides. *Mém. Acad. Sci. Berlin*, 11:274–315, 1755.

Todd E. Evans, Richard A. Moyer, Keith H. Burrell, Max E. Fenstermacher, Ilon Joseph, Anthony W. Leonard, Thomas H. Osborne, Gary D. Porter, Michael J. Schaffer, Philip B. Snyder, Paul R. Thomas, Jonathan G. Watkins, and William P. West. Edge stability and transport control with resonant magnetic perturbations in collisionless tokamak plasmas. *Nat Phys*, 2(6):419–423, June 2006. ISSN 1745-2473. doi: 10.1038/nphys312. URL http://dx.doi.org/10.1038/nphys312.

A. R. Field, D. Dunai, R. Gaffka, Y.-c Ghim, I. Kiss, B. Mszros, T. Krizsanczi, S. Shibaev, and S. Zoletnik. Beam emission spectroscopy turbulence imaging system for the MAST spherical tokamak. *Review of Scientific Instruments*, 83(1): 013508–013508–10, January 2012. ISSN 00346748. doi: 10.1063/1.3669756. URL http://dx.doi.org/10.1063/1.3669756.

Uriel Frisch. *Turbulence: The Legacy of A. N. Kolmogorov*. Cambridge University Press, November 1995. ISBN 0521457130.

A. Fujisawa, K. Itoh, A. Shimizu, H. Nakano, S. Ohshima, H. Iguchi, K. Matsuoka, S. Okamura, T. Minami, Y. Yoshimura, K. Nagaoka, K. Ida, K. Toi, C. Takahashi, M. Kojima, S. Nishimura, M. Isobe, C. Suzuki, T. Akiyama, T. Ido, Y. Nagashima, S.-I. Itoh, and P. H. Diamond. Experimental studies of zonal flow and field in compact helical system plasma. *Physics of Plasmas*, 15(5):055906, 2008. ISSN 1070664X. doi: 10.1063/1.2889012. URL http://dx.doi.org/10.1063/1.2889012.

Zhe Gao. Collisional damping of the geodesic acoustic mode. *Physics of Plasmas*, 20(3):032501, 2013. doi: 10.1063/1.4794339. URL http://dx.doi.org/10.1063/1.4794339.

Zhe Gao. Analytical theory of the geodesic acoustic mode in the small and large orbit drift width limits and its application in a study of plasma shaping effect. *Plasma Science and Technology*, 13(1):15–20, February 2011. ISSN 1009-0630. doi: 10.1088/1009-0630/13/1/04. URL http://dx.doi.org/10.1088/1009-0630/13/1/04.

Zhe Gao. Plasma shaping effects on the geodesic acoustic mode in the large orbit drift width limit. *Physics of Plasmas*, 17(9):092503–092503–7, September 2010. ISSN 1070664X. doi: 10.1063/1.3481464. URL http://dx.doi.org/10.1063/1.3481464.

O E Garcia. Collective motions in non-uniformly magnetized plasmas. *European Journal of Physics*, 24(4):331–339, July 2003. ISSN

0143-0807, 1361-6404. doi: 10.1088/0143-0807/24/4/351. URL http://iopscience.iop.org/0143-0807/24/4/351.

K J Gibson, N Barratt, I Chapman, N Conway, M R Dunstan, A R Field, L Garzotti, A Kirk, B Lloyd, H Meyer, G Naylor, T O'Gorman, R Scannell, S Shibaev, J Snape, G J Tallents, D Temple, A Thornton, S Pinches, M Valovic, M J Walsh, H R Wilson, and {the MAST team}. New physics capabilities from the upgraded thomson scattering diagnostic on MAST. *Plasma Physics and Controlled Fusion*, 52(12):124041, December 2010. ISSN 0741-3335, 1361-6587. doi: 10.1088/0741-3335/52/12/124041. URL http://iopscience.iop.org/0741-3335/52/12/124041.

D. K. Gupta, R. J. Fonck, G. R. McKee, D. J. Schlossberg, and M. W. Shafer. Detection of zero-mean-frequency zonal flows in the core of a high-temperature tokamak plasma. *Physical Review Letters*, 97(12):125002, 2006. doi: 10.1103/PhysRevLett.97.125002. URL http://dx.doi.org/10.1103/PhysRevLett.97.125002.

Robert Hager and Klaus Hallatschek. Radial propagation of geodesic acoustic modes. *Physics of Plasmas*, 16(7):072503–072503–8, July 2009. ISSN 1070664X. doi: 10.1063/1.3155106. URL http://dx.doi.org/10.1063/1.3155106.

Gregory W. Hammett and Francis W. Perkins. Fluid moment models for landau damping with application to the ion-temperature-gradient instability. *Phys. Rev. Lett.*, 64:3019–3022, Jun 1990. doi: 10.1103/PhysRevLett.64.3019. URL http://link.aps.org/doi/10.1103/PhysRevLett.64.3019.

Akira Hasegawa and Kunioki Mima. Pseudothreedimensional turbulence in magnetized nonuniform plasma. *Physics of Fluids*, 21(1):87–92, January 1978. ISSN 00319171. doi: 10.1063/1.862083. URL http://dx.doi.org/10.1063/1.862083.

Akira Hasegawa and Masahiro Wakatani. Plasma edge turbulence. *Physical Review Letters*, 50(9):682, February 1983. doi: 10.1103/PhysRevLett.50.682. URL http://dx.doi.org/10.1103/PhysRevLett.50.682. Copyright (C) 2009 The American Physical Society; Please report any problems to prola@aps.org.

R. D. Hazeltine, F. L. Hinton, and M. N. Rosenbluth. Plasma transport in a torus of arbitrary aspect ratio. *Physics of Fluids*, 16(10):1645–1653, 1973. doi: 10.1063/1.1694191. URL http://link.aip.org/link/?PFL/16/1645/1.

RD Hazeltine and JD Meiss. Shear-Alfvén dynamics of toroidally confined plasmas. *Physics Reports*, 121:1164, October 1985.

Richard D. Hazeltine and Francois L. Waelbroeck. *The Framework Of Plasma Physics*. Westview Press, January 2004. ISBN 0813342139.

Nicholas J. Higham. *Accuracy and Stability of Numerical Algorithms*. Society for Industrial Mathematics, 2 edition, August 2002. ISBN 0898715210.

N. Holtkamp. *Fusion Eng. Des.*, 82:427, 2007.

W. Horton. Drift waves and transport. *Reviews of Modern Physics*, 71(3):735, April 1999. doi: 10.1103/RevModPhys.71.735. URL http://dx.doi.org/10.1103/RevModPhys.71.735.

Wendell Horton. *Turbulent Transport in Magnetized Plasmas*. World Scientific Publishing Co Pte Ltd, October 2012. ISBN 9814383538.

M King Hubbert. Nuclear energy and the fossil fuels. *Drilling and Production Practice*, 1956. URL http://www.hubbertpeak.com/hubbert/1956/1956.pdf.

M King Hubbert. *Energy and Power*. Scientific American, 1971.

K. Itoh, S.-I. Itoh, P. H. Diamond, T. S. Hahm, A. Fujisawa, G. R. Tynan, M. Yagi, and Y. Nagashima. Physics of zonal flows. *Physics of Plasmas*, 13(5):055502–055502–11, May 2006. ISSN 1070664X. doi: doi:10.1063/1.2178779. URL http://pop.aip.org/resource/1/phpaen/v13/i5/p055502_s1.

M. Jakubowski, R. Fonck, and G. McKee. Observation of coherent sheared turbulence flows in the DIII-D tokamak. *Physical Review Letters*, 89(26), December 2002. ISSN 0031-9007. doi: 10.1103/PhysRevLett.89.265003. URL http://dx.doi.org/10.1103/PhysRevLett.89.265003.

A. Kirk, E. Nardon, R. Akers, M. Bcoulet, G. De Temmerman, B. Dudson, B. Hnat, Y.Q. Liu, R. Martin, P. Tamain, D. Taylor, and the MAST team. Resonant magnetic perturbation experiments on MAST using external and internal coils for ELM control. *Nuclear Fusion*, 50(3):034008, March 2010. ISSN 0029-5515. doi: 10.1088/0029-5515/50/3/034008. URL http://dx.doi.org/10.1088/0029-5515/50/3/034008.

A. Kirk, E. Nardon, P. Tamain, P. Denner, H. Meyer, S. Mordijck, and D. Temple. The effect of resonant magnetic perturbations on l and h-mode plasmas on MAST. *Journal of Nuclear Materials*, 415(1, Supplement):S910–S913, August 2011. ISSN 0022-3115. doi: 10.1016/j.jnucmat.2011.01.012. URL http://dx.doi.org/10.1016/j.jnucmat.2011.01.012.

P.J. Knight. *CENTORI: Source Code Documentation*, June 2011.

P.J. Knight, A. Thyagaraja, T.D. Edwards, J. Hein, M. Romanelli, and K.G. McClements. CENTORI: a global toroidal electromagnetic two-fluid plasma turbulence code. *Computer Physics Communications*, 183(11):2346–2363, November 2012. ISSN 0010-4655. doi: 10.1016/j.cpc.2012.06.002. URL http://dx.doi.org/10.1016/j.cpc.2012.06.002.

A. N. Kolmogorov. The local structure of turbulence in incompressible viscous fluid for very large reynolds numbers. *Dokl. Akad. Nauk SSSR*, 30:299–303, 1941a.

A. N. Kolmogorov. On degeneration (decay) of isotropic turbulence in an incompressible viscous fluid. *Dokl. Akad. Nauk SSSR*, 31:538–540, 1941b.

A. N. Kolmogorov. Dissipation of energy in locally isotropic turbulence. *Dokl. Akad. Nauk SSSR*, 32:16–18, 1941c.

V.P. Lakhin, V.I. Ilgisonis, and A.I. Smolyakov. Geodesic acoustic modes and zonal flows in toroidally rotating tokamak plasmas. *Physics Letters A*, 374(48):4872–4875, November 2010. ISSN 0375-9601. doi: 16/j.physleta.2010.10.012. URL http://dx.doi.org/16/j.physleta.2010.10.012.

J D Lawson. Some criteria for a power producing thermonuclear reactor. *Proceedings of the Physical Society. Section B*, 70(1):6, 1957. URL http://stacks.iop.org/0370-1301/70/i=1/a=303.

M. Leconte and P. H. Diamond. Impact of resonant magnetic perturbations on nonlinearly driven modes in drift-wave turbulence. *Physics of Plasmas*, 19(5): 055903–055903–11, March 2012. ISSN 1070664X. doi: 10.1063/1.3694675. URL http://dx.doi.org/10.1063/1.3694675.

Eric J. Lerner, S. Krupakar Murali, and A. Haboub. Theory and experimental program for p-b11 fusion with the dense plasma focus. *Journal of Fusion Energy*, January 2011. ISSN 0164-0313. doi: 10.1007/s10894-011-9385-4. URL http://dx.doi.org/10.1007/s10894-011-9385-4.

Z. Lin, T. S. Hahm, W. W. Lee, W. M. Tang, and R. B. White. Turbulent transport reduction by zonal flows: Massively parallel simulations. *Science*, 281(5384):1835 –1837, 1998. doi: 10.1126/science.281.5384.1835. URL http://dx.doi.org/10.1126/science.281.5384.1835.

Yueqiang Liu, A. Kirk, Y. Gribov, M.P. Gryaznevich, T.C. Hender, and E. Nardon. Modelling of plasma response to resonant magnetic perturbation fields in mast and iter. *Nuclear Fusion*, 51(8):083002, 2011. URL http://stacks.iop.org/0029-5515/51/i=8/a=083002.

B Lloyd, J-W Ahn, R.J Akers, L.C Appel, E.R Arends, K.B Axon, R.J Buttery, C Byrom, P.G Carolan, C Challis, D Ciric, N.J Conway, M Cox, G.F Counsell, G Cunningham, A Darke, A Dnestrovskij, J Dowling, M.R Dunstan, A.R Field, S.J Fielding, S Gee, M.P Gryaznevich, P Helander, M Hole, M.B Hood, P.A Jones, A Kirk, I.P Lehane, G.P Maddison, S.J Manhood, R Martin, G.J McArdle, K.G McClements, M.A McGrath, H Meyer, A.W Morris, S.K Nielsen, M Nightingale, A Patel, T Pinfold, M.N Price, J Qin, C Ribeiro, C.M Roach, D.C Robinson, O Sauter, V Shevchenko, S Shibaev, K Stammers, A Sykes, A Tabasso, D Taylor, M.R Tournianski, G Turri, M Valovic, G Voss, M.J Walsh, S Warder, J.R Watkins, H.R Wilson, Y Yang, S You, the MAST teams, and NBI. Overview of recent experimental results on MAST. *Nuclear Fusion*, 43(12):1665–1673, December 2003. ISSN 0029-5515. doi: 10.1088/0029-5515/43/12/012. URL http://dx.doi.org/10.1088/0029-5515/43/12/012/.

Cyrus S. MacLatchy, Claude Boucher, Deborah A. Poirier, and James Gunn. Gundestrup: A Langmuir/Mach probe array for measuring flows in the scrape-off layer of TdeV. *Review of Scientific Instruments*, 63(8):3923, 1992. ISSN 00346748. doi: 10.1063/1.1143239. URL http://dx.doi.org/10.1063/1.1143239.

Thomas Robert Malthus. *An Essay on the Principle of Population*. John Murray, London, 6th edition, 1798.

D C McDonald, Y Andrew, G T A Huysmans, A Loarte, J Ongena, J Rapp, , and S Saarelma. ELMy h-mode operation in JET. *Fusion Science and Technology*, 53, 2008.

Tom McMurray. `bisp3cum.m`, 2000. URL http://www.mathworks.co.uk/matlabcentral/fileexchange/60-bisp3cum.

A. B. Mikhailovskii and V. S. Tsypin. *Plasma Physics*, (13):785, 1971.

Kenro Miyamoto. *Controlled Fusion and Plasma Physics*. Taylor & Francis, 1 edition, October 2006. ISBN 1584887095.

Thomas Morgan. *Measurement of MAST edge ion temperatures and velocities*. PhD thesis, University of York, 2011.

R. A. Moyer, K. H. Burrell, T. N. Carlstrom, S. Coda, R. W. Conn, E. J. Doyle, P. Gohil, R. J. Groebner, J. Kim, R. Lehmer, W. A. Peebles, M. Porkolab, C. L. Rettig, T. L. Rhodes, R. P. Seraydarian, R. Stockdale, D. M. Thomas, G. R. Tynan, and J. G. Watkins. Beyond paradigm: Turbulence, transport, and the origin of the radial electric field in low to high confinement mode transitions in the DIII-D tokamak. *Physics of Plasmas*, 2(6):2397, 1995. ISSN 1070664X. doi: 10.1063/1.871263. URL http://dx.doi.org/10.1063/1.871263.

Stefano Musacchio. *Effects of friction and polymers on 2D turbulence*. PhD thesis, UNIVERSIT DEGLI STUDI DI TORINO, 2003.

Claude Louis Marie Henri Navier. Mémoire sur les lois du mouvement des fluides. *Mém. Acad. Sci. Inst.*, 6:389–440, 1822.

C. Nguyen, X. Garbet, and A. I. Smolyakov. Variational derivation of the dispersion relation of kinetic coherent modes in the acoustic frequency range in tokamaks. *Physics of Plasmas*, 15(11):112502–112502–15, November 2008. ISSN 1070664X. doi: 10.1063/1.3008048. URL http://dx.doi.org/10.1063/1.3008048.

Teofil-Cristian Oroian, Constantin-Iulian Vizitiu, and Florin Şerban. Bispectral resolution and leakage effect of the indirect bispectrum estimate for different types of 2D window functions. *WSEAS Transactions on Signal Processing*, 4(11), 2008. ISSN 1790-5052. URL www.wseas.us/e-library/transactions/signal/2008/28-787.pdf.

William H. Press, Saul A. Teukolsky, William T. Vetterling, and Brian P. Flannery. *Numerical Recipes 3rd Edition: The Art of Scientific Computing*. Cambridge University Press, 3 edition, August 2007. ISBN 0521880688.

Zhiyong Qiu, Liu Chen, and Fulvio Zonca. Collisionless damping of short wavelength geodesic acoustic modes. *Plasma Physics and Controlled Fusion*, 51(1):012001, January 2009. ISSN 0741-3335, 1361-6587. doi: 10.1088/0741-3335/51/1/012001. URL http://iopscience.iop.org/0741-3335/51/1/012001.

J. J. Ramos. General expression of the gyroviscous force. *Physics of Plasmas*, 12(11): 112301–112301–7, November 2005. ISSN 1070664X. doi: doi:10.1063/1.2114747. URL http://pop.aip.org/resource/1/phpaen/v12/i11/p112301_s1.

A. B. Rechester and M. N. Rosenbluth. Electron heat transport in a tokamak with destroyed magnetic surfaces. *Phys. Rev. Lett.*, 40:38–41, Jan 1978. doi: 10.1103/PhysRevLett.40.38. URL http://link.aps.org/doi/10.1103/PhysRevLett.40.38.

D. Reiser. Impact of large island perturbations on turbulent blob transport in tokamaks. *Physics of Plasmas*, 14(8):082314, 2007. ISSN 1070664X. doi: 10.1063/1.2771133. URL http://dx.doi.org/10.1063/1.2771133.

Todd Rider. *Fundamental limitations on plasma fusion systems not in thermodynamic equilibrium*. PhD thesis, Massachusetts Institute of Technology, 1995. URL http://dspace.mit.edu/handle/1721.1/11412.

J R Robinson, B Hnat, P Dura, A Kirk, P Tamain, and the MAST Team. Interaction between a low-frequency electrostatic mode and resonant magnetic perturbations in MAST. *Plasma Physics and Controlled Fusion*, 54(10):105007, October 2012. ISSN 0741-3335, 1361-6587. doi: 10.1088/0741-3335/54/10/105007. URL http://iopscience.iop.org/0741-3335/54/10/105007.

M. N. Rosenbluth and F. L. Hinton. Poloidal flow driven by ion-temperature-gradient turbulence in tokamaks. *Physical Review Letters*, 80(4):724, January 1998. doi: 10.1103/PhysRevLett.80.724. URL http://dx.doi.org/10.1103/PhysRevLett.80.724.

D G Sawnson. *Plasma Kinetic Theory*. CRC Press, 2008. ISBN 9781420075809.

Stephen Andrew Smith. *Dissipative closeures for statistical moments, fluid moments and subgrid scales in plasma turbulence*. PhD thesis, Princeton, 1997.

A I Smolyakov, C Nguyen, and X Garbet. Kinetic theory of electromagnetic geodesic acoustic modes. *Plasma Physics and Controlled Fusion*, 50(11):115008, November 2008. ISSN 0741-3335. doi: 10.1088/0741-3335/50/11/115008. URL http://dx.doi.org/10.1088/0741-3335/50/11/115008.

L. S. Soloviev. Reviews of plasma physics. volume 6, page 239. (New York: Consultants Bureau), 1975.

Lyman Spitzer Jr. Equations of motion for an ideal plasma. *Astrophys J.*, 116:299, September 1952.

Lyman Spitzer Jr. The stellarator concept. *Physics of Fluids*, 1(4):253–264, July 1958. doi: 10.1063/1.1705883. URL http://link.aip.org/link/?PFL/1/253/1.

George G. Stokes. On the theories of internal friction of fluids in motion. *Trans. Cambridge Philos. Soc.*, 8, 1845.

D.R. Sweetman. Ignition condition in tokamak experiments and role of neutral injection heating. *Nuclear Fusion*, 13(2):157–165, March 1973.

ISSN 0029-5515, 1741-4326. doi: 10.1088/0029-5515/13/2/002. URL http://iopscience.iop.org/0029-5515/13/2/002.

Toshiki Tajima. *Computational Plasma Physics: With Applications to Fusion and Astrophysics*. Westview Press Inc, reprint edition, 2004. ISBN 0813342112.

P Tamain, A Kirk, E Nardon, B Dudson, B Hnat, and the MAST team. Edge turbulence and flows in the presence of resonant magnetic perturbations on MAST. *Plasma Physics and Controlled Fusion*, 52(7):075017, July 2010. ISSN 0741-3335. doi: 10.1088/0741-3335/52/7/075017. URL http://dx.doi.org/10.1088/0741-3335/52/7/075017/.

C M Tchen. On the spectrum of energy in turbulent shear flow. *Journal of the National Bureau of Standards*, 50(1), 1953.

A Thyagaraja. Numerical simulations of tokamak plasma turbulence and internal transport barriers. *Plasma Physics and Controlled Fusion*, 42(12B):B255–B269, December 2000. ISSN 0741-3335. doi: 10.1088/0741-3335/42/12B/320. URL http://iopscience.iop.org/0741-3335/42/12B/320.

A. Thyagaraja, P.J. Knight, and N. Loureiro. Mesoscale plasma dynamics, transport barriers and zonal flows: simulations and paradigms. *European Journal of Mechanics - B/Fluids*, 23(3):475–490, May 2004. ISSN 0997-7546. doi: 10.1016/j.euromechflu.2003.10.009. URL http://dx.doi.org/10.1016/j.euromechflu.2003.10.009.

A. Thyagaraja, P. J. Knight, M. R. de Baar, G. M. D. Hogeweij, and E. Min. Profile-turbulence interactions, magnetohydrodynamic relaxations, and transport in tokamaks. *Physics of Plasmas*, 12(9):090907–090907–6, September 2005. ISSN 1070664X. doi: 10.1063/1.2034387. URL http://dx.doi.org/10.1063/1.2034387.

G. R. Tynan, R. A. Moyer, M. J. Burin, and C. Holland. On the nonlinear turbulent dynamics of shear-flow decorrelation and zonal flow generation. *Physics of Plasmas*, 8(6):2691, 2001. ISSN 1070664X. doi: 10.1063/1.1357220. URL http://dx.doi.org/10.1063/1.1357220.

A. A. Ware. Pinch effect for trapped particles in a tokamak. *Phys. Rev. Lett.*, 25:15–17, Jul 1970. doi: 10.1103/PhysRevLett.25.15. URL http://dx.doi.org/10.1103/PhysRevLett.25.15.

John Wesson. *Tokamaks*. Oxford University Press, 3 edition, November 2004. ISBN 0198509227.

Gareth P. Williams. Jupiter's atmospheric circulation. *Nature*, 257(5529):778, October 1975. doi: 10.1038/257778a0. URL http://dx.doi.org/10.1038/257778a0.

Niels Winsor. Geodesic acoustic waves in hydromagnetic systems. *Physics of Fluids*, 11(11):2448, 1968. ISSN 00319171. doi: 10.1063/1.1691835. URL http://dx.doi.org/10.1063/1.1691835.

K. S. Yee. Numerical solution of initial boundary value problems involving Maxwells equations in isotropic media. *IEEE Trans. Antennas Propagat.*, 14:302307, 1966.